

**Confined Uniaxial Compaction Observing
Triaxial Response of Granular Media
under Quasi-static Loading Conditions**

by

Piotr Nicewicz

A thesis submitted in partial fulfillment of the requirements for the degree of

Master of Science

Department of Mechanical Engineering
UNIVERSITY OF ALBERTA

©Piotr Nicewicz, 2019

Abstract

Experimental studies have been carried out in this thesis to enhance the understanding of granular material failure by observing the effects of particle size on material properties. Understanding the granular behaviour of materials is important in pharmaceutical research, product quality in the additive manufacturing industry, and ballistic performance in defence applications. In order to investigate these granular material behaviours in this thesis, two different experimental apparatuses were designed to conduct confined uniaxial compression tests under quasi-static loading conditions. The triaxial compaction response was monitored using a displacement transducer and load cells to derive material property characteristics.

First, the material response of granular stainless steel 316 was captured using the thick-walled cylinder approach where a load washer and strain gauges relate the hydro-static pressure effects as a function of porosity, particle size dependency on wall friction effects, and particle size-dependent failure mechanisms. The average particle sizes investigated were: $127 \pm 34 \mu\text{m}$, $309 \pm 88 \mu\text{m}$, $487 \pm 98 \mu\text{m}$. Observations revealed that the path of crushing out porosity varied based on the particle size and the frictional effects. Scanning Electron Microscope images were taken to examine the surface features and failure mechanisms of the compacted material. The analysis indicated that smaller particles exhibited significant plastic deformation and flow, while the larger appeared to show micro-cracking which lead to inelastic deformation and particle fracture.

Second, quasi-static uniaxial confined compaction of granular alumina and boron carbide was also studied, observing the triaxial stress effects of the materials as a function of particle size, using the instrumented die approach. The average particle sizes for alumina powder used in the experiments were: $133 \pm 38 \mu\text{m}$, $201 \pm 42 \mu\text{m}$, $290 \pm 52 \mu\text{m}$, and $414 \pm 57 \mu\text{m}$. The material response was captured using load cells and a displacement transducer to relate the hydro-static pressure as a function of porosity, the bulk modulus as a function of hydro-static pressure, and the transmission ratio as a function of applied load all for increasing particle sizes. Investigation of these ceramics revealed that for alumina, increasing the particle size resulted in an increase in strength for a fixed porosity, the bulk modulus did not show clear particle-size dependent trends, and the transmission ratio showed increasing behaviour where larger particles transmitted more load. To contrast, similar particle sizes were investigated for granular boron carbide: $152 \pm 26 \mu\text{m}$, $171 \pm 23 \mu\text{m}$, $303 \pm 46 \mu\text{m}$, and $461 \pm 44 \mu\text{m}$. For granular boron carbide, the path of crushing out porosity decreased with increasing particle size, the change in bulk modulus of the material increased with increasing particle size, and no clear particle-size dependent trends were observed when looking at the transmission ratio during the

compaction. Likewise, for both ceramics, SEM images were taken to observe the surface features of the loose and compacted material to track any failure mechanisms before and after experiments. Post-experiment SEM analysis revealed that alumina powder fragmented from elongated shapes to block-like structures, while the boron carbide powder appeared more circular before the experiments and fragmented into smaller comminuted pieces during experimentation. The degree of fragmentation was strongly correlated with the maximum hydro-static pressure reached during experimentation, regardless of initial particle size.

Altogether, these results are important to better understand the particle-size dependent behaviours in metals and advanced ceramics so that failure regimes can be more accurately conveyed in validating failure models and improving the use of materials in blast mitigating structures.

Preface

I, Piotr Nicewicz, declare that this thesis titled, ‘Confined Uniaxial Compaction Observing Triaxial Response of Granular Media under Quasi-static Loading Conditions’ and the work presented in it are my own. Furthermore, permission is hereby granted to the University of Alberta Libraries to reproduce single copies of this thesis and to lend or sell such copies for private, scholarly or scientific research purposes only. Where the thesis is converted to, or otherwise made available in digital form, the University of Alberta will advise potential users of the thesis of these terms.

The author reserves all other publication and other rights in association with the copyright in the thesis and, except as herein before provided, neither the thesis nor any substantial portion thereof may be printed or otherwise reproduced in any material form whatsoever without the author’s prior written permission.

"Try not to become a man of success, but rather try to become a man of value."

-Albert Einstein

Dedicated to my parents, Marta and Andrzej.

Acknowledgements

I would like to begin by thanking my supervisor Dr. J. D. Hogan. His knowledge, expertise, and guidance were critical to the success of my thesis. He dedicated many hours teaching me how to understand material properties from data, convey his intelligence in material science, and how to deliver information in the form of critical writing. Without his technical support, many aspects of this work would not be possible and for that I am truly grateful; he gave me a chance to prove myself.

Furthermore, I would like to extend my appreciation to doc. Ing. Peter Peciar PhD, Ing. Oliver Macho PhD, and doc. Ing. Roman Fekete PhD of the Slovak University of Technology in Bratislava, for their comprehension and collaboration. In particular, assisting with conducting experiments and leading insightful discussions on the research topic. Their timely feedback and guidance were a critical aspect in executing this project. In addition, I am grateful for the hospitality of the research team during my time in Bratislava.

Next, I would like to thank my lab mates and fellow graduate students for their countless interesting conversations, that kept me sane throughout my degree. This created a cheerful environment to take the edge off during hectic times. I wish you all the best, and good luck on your research and future endeavours.

I also would like to express my gratitude to the supporting staff at the University of Alberta and the Mechanical Engineering machine shop for their hard work and design recommendations. In particular, I would like to thank Bernie Faulkner for his insightful talks and helpful advise. He aided in technical design, as well as shared many interesting stories which maintained an entertaining environment.

Last, but certainly not the least, I would like to thank my family for the ongoing support and encouragement. Their backing continues to motivate me to reach greater heights and to never give up. Their encouragement kept me moving forward throughout my under graduate and graduate degrees and for that I am very thankful.

Contents

Abstract	i
Preface	iv
Acknowledgements	vii
List of Figures	xi
List of Tables	xv
Abbreviations	xvi
Symbols	xvii
1 Introduction	1
1.1 The Study of Granular Material	1
1.1.1 Granular Flow in Additive Manufacturing	2
1.1.2 Granular Flow in Pharmaceuticals	3
1.1.3 Granular Flow in Advanced Ceramics for Ballistic Protection	3
1.2 Compaction Methods	5
1.2.1 Thick-walled Cylinder (TWC) - Confined Uniaxial Compaction	5
1.2.2 Instrumented Die - Confined Uniaxial Compaction	6
1.2.3 Triaxial Compaction	7
1.3 Thesis Objectives	8
1.4 Thesis Goals	9
1.5 Contributions	9
1.6 Thesis Structure	10
2 Theory of Mechanics of Granular Materials	11
2.1 3D Hooke's Law	11
3 Confined Uniaxial Compression of Granular Stainless Steel 316	14
3.1 Material Composition and Geometry	14
3.2 Particle Distribution	15
3.3 Experiment Configuration	17

3.3.1	Thick-walled Cylinder (TWC)	17
3.3.2	TWC Theory	19
3.4	Compaction Results and Discussion	23
3.4.1	Hydro-static Response	23
3.4.2	Bulk Modulus	24
3.4.3	Friction	25
3.4.4	Janssen Coefficient	26
3.4.5	SEM Images of Material Failure	27
3.4.6	Discussion and Summary	27
3.4.7	Concluding remarks	30
4	Quasi-static Confined Uniaxial Compaction of Granular Alumina and Boron Carbide	31
4.1	Material Composition and Geometry	31
4.1.1	Alumina	32
4.1.2	Boron Carbide	33
4.2	Particle Distribution	34
4.3	Experiment Configuration	35
4.3.1	Instrumented Die	35
4.3.2	Instrumented Die Theory	38
4.4	Compaction Results and Discussion	41
4.4.1	Hydro-static Response	41
4.4.2	Bulk Modulus	43
4.4.3	Friction	45
4.4.3.1	Failure	47
4.4.4	Distributions	48
4.5	Discussion and Summary	49
4.5.1	Concluding Remarks	55
5	Conclusion	56
5.1	Conclusion	56
5.2	Implications	57
5.3	Future Work and Recommendations	58
A	Data Processing	75
A.1	MATLAB Code - Confined Uniaxial Compression of Granular Stainless Steel 316	75
A.2	MATLAB Code - Quasi-static Confined Uniaxial Compaction of Granular Al_2O_3 and B_4C	78
B	Uncertainty - Propagation of Error	81
C	SEM Images of Tested Materials	84
D	Hooke's Law	91
D.1	Generalized Hooke's Law	91
D.2	Material Symmetries	93

D.3 Cylindrical Coordinates	95
E Supplementary Material	97
E.1 Curve fitting	97
E.2 Particle distribution data	99
F Curriculum Vitae	101

List of Figures

1.1	The cross-section of the TWC apparatus shows the void holding the specimen along with the external instruments required to capture the material behaviour during compaction. This testing configurations can accommodate a range of material amounts depending on required axial load.	6
1.2	An adapted sketch of the instrumented die which directly measures within the void, simultaneously capturing constitutive data and material properties [67].	7
1.3	Sketch of the triaxial pressure cell used for compacting cylindrical powder specimens of diameter 12.7 mm for probing the yield surface [68].	8
3.1	SEM images of the stainless steel 316 powder at two different particle sizes: A $127 \pm 34 \mu\text{m}$ and B $487 \pm 98 \mu\text{m}$, respectively.	15
3.2	Schematic of the cross-section of the experimental set-up illustrating key components and dimensions. Due to the nature of the compression machine, the load was applied from the bottom.	18
3.3	Quasi-static granular compaction of stainless steel 316 powder for particle sizes of: $127 \pm 34 \mu\text{m}$, $309 \pm 88 \mu\text{m}$, $487 \pm 98 \mu\text{m}$ depicting the load and unload response.	23
3.4	The bulk modulus of stainless steel 316 as a function of applied stress for particle sizes of: $127 \pm 34 \mu\text{m}$, $309 \pm 88 \mu\text{m}$, $487 \pm 98 \mu\text{m}$	24
3.5	The transmission ratio relationship of granular stainless steel 316 as a function of applied stress for different particle sizes: $127 \pm 34 \mu\text{m}$, $309 \pm 88 \mu\text{m}$, $487 \pm 98 \mu\text{m}$	25
3.6	Janssen coefficient of stainless steel 316 as a function of porosity for varying particle sizes: $127 \pm 34 \mu\text{m}$, $309 \pm 88 \mu\text{m}$, $487 \pm 98 \mu\text{m}$	26
3.7	SEM images of the stainless steel 316 powder at two different particle sizes: position A $127 \pm 34 \mu\text{m}$ and position B $487 \pm 98 \mu\text{m}$ respectively. The red arrows indicate the failure within the material post-compaction.	27
4.1	SEM images were taken of the Al_2O_3 powder to observe powder morphology before experiments and failure features post-experiment. Position A depicts the Al_2O_3 powder ($133 \pm 38 \mu\text{m}$) before compression. B depicts the Al_2O_3 powder ($133 \pm 38 \mu\text{m}$) after compression. Lastly, position C depicts the large Al_2O_3 powder ($414 \pm 57 \mu\text{m}$) after the experiment showing the resulting material size and shapes and D depicts surface features of the $414 \pm 57 \mu\text{m}$ Al_2O_3 powder.	32

- 4.2 SEM images of B_4C were taken to observe the small and large particles, focusing on powder morphology before and after experiment. Position A depicts $152 \pm 26 \mu m$ B_4C powder before compression. Position B depict the $303 \pm 46 \mu m$ particle size showing the overall geometry before compression. Position C depict the postmortem $303 \pm 46 \mu m$ powder visualizing the overall fragment distribution and D depicts the surface features post experiment. 33
- 4.3 An isometric cross-section view is shown of the compaction apparatus used in compressing Al_2O_3 & B_4C powders to show the different components. The colour in the figure is to distinguish various components that constitute the apparatus. 36
- 4.4 In the figure we see the hydro-static pressure response of granular Al_2O_3 . In A, the hydro-static pressure response as a function of porosity was captured for the range of particles $133 \pm 38 \mu m$. In B, the hydro-static pressure response as a function of porosity was captured for the particle size range $201 \pm 42 \mu m$. In position C the hydro-static pressure response was captured for the particle size range $290 \pm 52 \mu m$. In position D, the hydro-static pressure response was captured for particle size range $414 \pm 57 \mu m$ 41
- 4.5 In the figure we see the hydro-static pressure response of granular B_4C . In A, the hydro-static pressure response as a function of porosity was captured for the range of particles: $152 \pm 26 \mu m$. In B, the hydro-static pressure response as a function of porosity was captured for the particle size range: $171 \pm 23 \mu m$. In position C the hydro-static pressure response was captured for the particle size range: $303 \pm 46 \mu m$. In position D, the hydro-static pressure response was captured for particle size range: $461 \pm 44 \mu m$ 42
- 4.6 In the figure we see the bulk modulus response of the Al_2O_3 powder as a function of hydro-static pressure. In A, the bulk modulus response as a function of hydro-static pressure was captured for the range of particles: $133 \pm 38 \mu m$. In B, the bulk modulus response as a function of hydro-static pressure was captured for the particle size range: $201 \pm 42 \mu m$. In position C the bulk modulus response as a function of hydro-static pressure was captured for the particle size range: $290 \pm 52 \mu m$. In position D, the bulk modulus response as a function of hydro-static pressure was captured for particle size range: $414 \pm 57 \mu m$ 43
- 4.7 In the figure we see the bulk modulus response of granular B_4C . In A, the bulk modulus response as a function of hydro-static pressure was captured for the range of particles: $152 \pm 26 \mu m$. In B, the bulk modulus response as a function of hydro-static pressure was captured for the particle size range: $171 \pm 23 \mu m$. In position C the bulk modulus response as a function of hydro-static pressure was captured for the particle size range: $303 \pm 46 \mu m$. In position D, the bulk modulus response as a function of hydro-static pressure was captured for particle size range: $461 \pm 44 \mu m$ 44

4.8	In the figure we see the transmission ratio of the Al_2O_3 powder as a function of applied stress. In position A, the transmission ratio response as a function of the applied stress was captured for the range of particles: $133 \pm 38 \mu\text{m}$. In position B, the transmission ratio as a function of applied stress was captured for the particle size range: $201 \pm 42 \mu\text{m}$. In position C the transmission ratio was captured for the particle size range: $290 \pm 52 \mu\text{m}$. In position D, the transmission ratio was captured for particle size range: $414 \pm 57 \mu\text{m}$	45
4.9	In the figure we see the transmission ratio of the B_4C powder as a function of applied stress. In position A, the transmission ratio response as a function of the applied stress was captured for the range of particles: $152 \pm 26 \mu\text{m}$. In position B, the transmission ratio as a function of applied stress was captured for the particle size range: $171 \pm 23 \mu\text{m}$. In position C the transmission ratio was captured for the particle size range: $303 \pm 46 \mu\text{m}$. In position D, the transmission ratio was captured for particle size range: $461 \pm 44 \mu\text{m}$	46
4.10	In A we see the overall trend of the bulk modulus for granular B_4C , depicting the sensitivity of particle size on bulk modulus as a function of hydrostatic pressure. Illustrated in the B is the overall trend of the transmission ratio of granular Al_2O_3 . As the particle size increases, the transmission ratio increases. To show the global behaviour of the material response, the tests with the largest deviation with respect to a given particle size were chosen.	51
4.11	In the figure are illustrated the overall trends seen in the granular Al_2O_3 , position A, and granular B_4C , position B, depicting the hydro-static pressure response as a function of porosity for increasing particle sizes. To show the global response of the material, individual tests with respect to a given particle size were chosen.	52
4.12	The cumulative distribution of the particles for Al_2O_3 powder for the range of particles: $133 \pm 38 \mu\text{m}$, $201 \pm 42 \mu\text{m}$, $290 \pm 52 \mu\text{m}$, and $414 \pm 57 \mu\text{m}$	54
4.13	The cumulative distribution of the particles for B_4C powder for the range of particles: $152 \pm 26 \mu\text{m}$, $171 \pm 23 \mu\text{m}$, 303 ± 46 , and $461 \pm 44 \mu\text{m}$	54
C.1	SEM image of stainless steel 316 powder with an average particle size of $127 \pm 34 \mu\text{m}$ before the quasi-static compaction.	84
C.2	SEM image of stainless steel 316 powder with an average particle size of $487 \pm 98 \mu\text{m}$ before the quasi-static compaction.	85
C.3	SEM image of the stainless steel 316 powder at an average particle size of $127 \pm 34 \mu\text{m}$ post compaction.	85
C.4	SEM image of the stainless steel 316 powder at an average particle size of $487 \pm 98 \mu\text{m}$ post compaction.	86
C.5	SEM images were taken of the Al_2O_3 powder to observe powder morphology before experiments and failure features post-experiment. The following depicts the Al_2O_3 with an average particle size $170 \pm 63 \mu\text{m}$ before compression.	86
C.6	The following is an SEM image of Al_2O_3 powder with an average particle size $170 \pm 63 \mu\text{m}$ after compression.	87

C.7	SEM image of the large Al_2O_3 powder with an average particle size of $450 \pm 83 \mu\text{m}$ after the experiment showing the resulting material size and shapes.	87
C.8	SEM images were taken of the Al_2O_3 powder to observe powder morphology before experiments and failure features post-experiment. The following is Al_2O_3 powder with an average particle size of $450 \pm 83 \mu\text{m}$	88
C.9	SEM images of B_4C were taken to observe the small and large particles, focusing on powder morphology before and after experiment. The figure depicts $170 \pm 40 \mu\text{m}$ B_4C powder before compression.	88
C.10	The figure depicts B_4C powder with an average particle size of $320 \pm 59 \mu\text{m}$ showing the overall geometry before compression.	89
C.11	The figure depicts the postmortem B_4C powder with an average particle size of $320 \pm 59 \mu\text{m}$ visualizing the overall fragment distribution.	89
C.12	The following figure depicts the surface features post experiment of B_4C powder with an average particle size $320 \pm 59 \mu\text{m}$	90
D.1	Stress components defined with respect to the Cartesian coordinate system [133].	92
D.2	Stress components with respect to the cylindrical coordinates [133].	95
E.1	For the Al_2O_3 powder, trends can be observed when plotting the constants (A, B, C) as a function of average particle size for (E.1). Polynomial fitting functions were used for the purpose to explicitly show the overall trends of each constant.	98
E.2	The function constants (A, B, C) for granular B_4C were plotted against increasing particle size. Polynomial fitting functions of order two and three were used for the purpose of depicting overall trends of each constant.	99
E.3	The empirical cumulative distribution function is plotted against average particle size before and after compaction for granular alumina.	100
E.4	The empirical cumulative distribution function is plotted against average particle size before and after compaction for granular boron carbide.	100

List of Tables

3.1	Chemical composition of Alfa Aesar stainless steel 316 powder.	15
3.2	Particle size characterization observing the diameter distribution and circularity of each particle.	16
3.3	Relative systemic error of the minimum and maximum cases for the mechanical properties of stainless steel 316.	22
4.1	Al ₂ O ₃ Powder Characterization: the material span is Δ (unitless), the tenth percentile D_{10} (μm), the fiftieth percentile D_{50} (μm), and ninetieth percentile D_{90} (μm) of the distribution.	35
4.2	B ₄ C Powder Characterization: the material span is Δ (unitless), the tenth percentile D_{10} (μm), the fiftieth percentile D_{50} (μm), and ninetieth percentile D_{90} (μm) of the distribution.	35
4.3	Alumina experiment parameters: mean diameter $\bar{\phi}$ (μm), mass m (g), initial void volume V_o (mm^3), initial density ρ_i (kg m^{-3}), final density ρ_f (kg m^{-3}), initial porosity ϕ_i (%), and final porosity ϕ_f (%).	37
4.4	Boron carbide experiment parameters: mean diameter $\bar{\phi}$ (μm), mass m (g), initial void volume V_o (mm^3), initial density ρ (kg m^{-3}), final density ρ (kg m^{-3}), initial porosity ϕ_i (%), and final porosity ϕ_f (%).	37
4.5	Systematic uncertainty: propagation of error.	40
4.6	Standard deviation in material properties at each particle size tested for granular Al ₂ O ₃ and B ₄ C.	52

Abbreviations

AM	A dditive M anufacturing
SiC	S ilicon C arbide
TWC	T hick W alled C ylinder
LVDT	L inear V ariable D ifferential T ransformer
SEM	S canning E lectron M icroscope
G3	Morphologi G3 M icroscope
HRC	R ockwell H ardness S cale C
Al₂O₃	A lumina O xide
B₄C	B oron C arbide
TiC	T itanium C arbide
WC	T ungsten C arbide

Symbols

a	inner crucible radius	m
A	projectd area of particles	m ²
A_o	cross-section of the crucible void	m ²
A_r	cross-sectional area of radial pin	m ²
b	outer crucible radius	m
B_{ep}	elasto-plastic bulk modulus	Pa
C	circularity	unitless
C_{iklm}	fourth order stiffness tensor	Pa
Da	area equivalent diameter	μm
$D[4, 3]$	De Broukere mean diameter	μm
D_{10}	thenth percentile in distribution	unitless
D_{50}	fiftieth percentile in distribution	unitless
D_{90}	ninetieth percentile in distribution	unitless
E_c	Young's modulus of elasticity of the crucible	Pa
F_f	friction force output from load washer	N
F_{MTS}	force output from compression machine	N
F_z	axial force	N
K	Janssen coefficient	unitless
m	mass	kg
\emptyset	particle diameter	μm
p	perimeter of particles	m
P	hydro-static pressure	Pa
ΔP	change in hydro-static pressure	Pa
r	crucible radius	m
T	transmission ratio	unitless

V_o	initial specimen volume	m^3
ΔV	change in volume	m^3
δ	relative displacement	m
Δ	span in distribution	unitless
ε_{kl}	second order strain tensor	unitless
ε_r	radial strain	unitless
$\dot{\varepsilon}$	compression strain rate	s^{-1}
θ	principle direction in cylindrical coordinates	o
ν_c	Poisson's ratio of the crucible	unitless
$\rho_{i,f}$	initial and final density	kg m^{-3}
ρ_s	solid bulk density	kg m^{-3}
ϕ	porosity of the sample	%
$\phi_{i,f}$	initial and final packing porosity	%
σ_a	applied stress	Pa
σ_{ik}	second order stress tensor	Pa
σ_r	radial stress	Pa
$\sigma_{r,z,\theta}$	stress tensor in cylindrical coordinates	Pa
σ_t	transmitted stress through the sample	Pa
σ_z	axial stress	Pa

Chapter 1

Introduction^{a,b}

1.1 The Study of Granular Material

Granular materials are an agglomeration of discrete solid macroscopic particles (magnitude of 10^{-3} m) that behave differently than continuous solids, liquids, and gases. The granular material response can be observed at the bulk scale or at the individual particles. The understanding of granular behaviour is critical in various industries for process optimization such as, for example, manufacturing [1], pharmaceutical [2], and geo-technical [3] applications. Typically, researchers choose to pursue two main approaches when describing the granular behaviour: discrete and continuum analysis. In the discrete approach, research is focused on individual particle behaviour [4–6]. The discrete models are based on kinematics of the particles and allow for simulating mechanical characteristics [7]. More recently, discrete models exhibit deformability and allow for the simulation of the yielding behaviour of materials [8]. Conversely, in continuum-scale studies, researchers focus on using constitutive laws and conservation equations to model the ensemble of granular behaviour [9, 10]. Specifically, researchers have derived a number of yield and friction models to express various characteristics such as variation

^aA portion of this chapter has been published in: P. Nicewicz, T. Sano, J.D. Hogan, “Confined Uniaxial Compression of Granular Stainless Steel 316”. Powder Technology. Manuscript number: POWTEC-D-18-03323R1. Article reference: PTEC14359.

^bA portion of this chapter has been submitted for publication in: P. Nicewicz, P. Peciar, O. Macho, T. Sano, J.D. Hogan. “Quasi-static Confined Uniaxial Compaction of Granular Alumina and Boron Carbide Observing the Particle Size Effects”. Journal of the American Ceramic Society. *Under review*. Manuscript number: JACERS-44392

in friction as a function of localized stresses [7]. However, challenges exist with both approaches. Discrete modelling is computationally expensive and struggles with complex non-linear behaviour [7, 11]. On the other hand, certain continuum computational techniques struggle when high levels of strain occur which is difficult to represent in a unified model [9]. Researchers have been interested in the micro-scale of solid-like behaviour of grains [12] while capturing the macro-scale fluid-like characteristics [13] due to the large application possibilities.

1.1.1 Granular Flow in Additive Manufacturing

One method in processing granular materials is through cold die compaction. This process consists of having the powder flow into a die and compacting it at room temperature. The loose material produces a coherent piece known as a ‘green compact’ which is then sintered into the final product [14]. The simplicity of this process makes it desirable in many industry sectors. Work on cold compaction of granular materials has been conducted in additive manufacturing (AM), where it is important to understand the relationship between the powder characteristics and the mechanics of the consolidated part [15]. For example, mechanical properties, surface finish, and integrity of the final structure are highly influenced by the characteristics of the powder material that is used in the manufacturing process. Further, flow properties (flowability) of the powder highly influences the finish, grade, and strength of the final product. The correlation between factors such as the shape distribution, size distribution, density, and packing density are a complex and ongoing research topic [16, 17]. In one example, Spierings et al. [17] determined that larger stainless steel 316 particles in the raw powder consequently resulted in bigger pores in the final steel part. The thicker layers created heterogeneous regions in the structure that promoted fracture [17] and increased void density that creates nucleation sites for brittle failure, and promotes crack propagation. Comparable research was done by Bai et al. [18] when analyzing a binder jetting AM technique with copper particles. Similar to laser sintering, binder jetting combines the metal powder with a binder and creates a green compact structure surrounded by the remaining powder, which is then sintered. By using a bimodal powder distribution, Bai et al. [18] was able to improve the powder density by 8.2% and flowability by 10.5%. Powder flow properties have been shown to play an important role in the cohesive strength, friction,

compressibility, and transportation of the powder [16, 19]. The tailoring of particle sizes is required to improve the final density of the manufactured structure.

1.1.2 Granular Flow in Pharmaceuticals

The compaction of cold-pressed powder has likewise been of particular interest to pharmaceutical researchers [20] when looking at particle distribution, Jansen coefficient for particle friction, and porosity as a function of applied stress [2, 21]. For example, Michrafy et al. [21] studied the friction of pill compaction lubricant effects on the die wall friction coefficient. They showed that wall friction and particle friction primarily account for non-uniform stress distribution and produce a density gradient of the material in the compact; the lack of consistent density results in inferior mechanical properties [22]. Similar work conducted by Kadiri et al. [20] looked at predicting the axial density distribution of micro-crystalline material while determining the material properties during quasi-static triaxial compression. The axial density of cellulose decreases from the top to the bottom of compaction sample and Kadiri et al. [20] concluded that the particle size and shape significantly influence the density distribution throughout pharmaceutical tablet compaction.

1.1.3 Granular Flow in Advanced Ceramics for Ballistic Protection

Ceramics emerged in ballistic protection applications around the 1960's [23]. They have been used to mitigate various threats ranging from high pressure blasts to projectile and fragment penetration [24–27]. Due to the superior strength-to-weight ratio [28] and impact resistance [29], advanced ceramics have been used in the protecting vehicles and personnel in combat situations ever since. Projectile impact is a complex event where the ensemble of granular material behaves differently. For example the size of the impactor with respect to the target material dictates whether or not the ceramic material behaves like a liquid or solid. In addition, the loading conditions and failure mechanisms affect the amount of bulk or granular behaviour of the ceramic. Accompanying research on the development of advanced protection applications have included, for example, studying multi-hit capabilities of armour protection [25], the dwell-penetration relationship in projectile penetration [30], and fragmentation behaviour on projectile erosion and energy dissipation [31].

The failure of brittle ceramics through micro-cracking and fragmentation has been studied previously by many. Mott et al. [32] was one of the first researchers to couple physical and statistical theories of fragmentation. Later work by Grady and Kipp [33] noted that fragmentation occurs in three stages: crack nucleation, crack growth, and crack coalescence where they successfully related fragmentation sizes to mechanical properties and loading rates. Other work done by Sarva and Nemat-Nasser [34] showed that silicon carbide (SiC) fragment size was strongly correlated with induced strain rates, which aligned with well known concepts developed by Grady and Kipp [33]. Higher strain rates ($\sim 10^2 \text{ s}^{-1}$) produced significantly smaller fragments when compared to quasi-static compression. Related work by Hogan et al. [35] observed distinct fragmentation regimes during the dynamic fragmentation of boron carbide. Smaller fragments ($<100 \mu\text{m}$) appeared to be micro-structure dependent and arose from the coalescence of fractures from internal defects, while larger fragments ($>100 \mu\text{m}$) were more-so dependent on specific structural mechanisms (buckling of columns) rather than material. This work demonstrated that we are able to tailor the fragmentation sizes by controlling the inherent defect spacing in the micro-structure.

Fragmentation has been noted to be important in the ballistic performance of advanced ceramics [36–40]. For example, Shockey et al. [37] concluded that penetration resistance is governed by compressive strength, hardness, pulverization characteristics, frictional flow of fragments, and fragment abrasiveness (i.e., particle geometry). Related work by Krell and Strassburger [8] noted that fragment size and shape dictated the level of projectile erosion and energy dissipation during ballistic impact. With fragmentation happening as a primary material failure mechanism, the incentive of studying ceramics in a granular state increases. In their simulation study, Holmquist and Johnson [41] also demonstrate the importance of the behaviour of the damaged and granular forms of advanced ceramics on penetration resistance and characterizing flow stress by observing particle size distribution. They also noted that most of the uncertainty in modelling such behaviour stems from the pressure-volume response.

Experimental work on the granular behaviour, failure, and mechanical properties of advanced ceramics has been explored before [42–46], nonetheless, it is limited, likely as a result of the natural material hardness making it difficult to conduct experiments. However, there exists research in granulated rocks and minerals [47, 48]. For example, Huang et al. [49] conducted dynamic compression tests on quartz sands in which a simple

model for predicting the dynamic break efficiency of the granular materials was derived. Borg and Vogler [50] dynamically compressed granular tungsten carbide and noted the dynamic compaction characteristics of the material. Modelling efforts simulating the behaviour of granulated advanced ceramics has also been limited [51], with the majority of the literature on experimentation and modelling the behaviour of geological materials [52–57]. Such work presented by previous researchers is complimentary to accurately reproducing ceramic failure in brittle material models, which gets further implemented in simulating impact.

1.2 Compaction Methods

1.2.1 Thick-walled Cylinder (TWC) - Confined Uniaxial Compaction

The first method typically used for testing granular materials is the thick-walled cylinder approach. This technique is derived from soil mechanics where it has been extensively used to determine quasi-static material behaviour [58–62]. This method consists of placing the material inside a metal tube where the top and bottom punch seal the specimen. An axial load is applied to one or both punches and the sample becomes compressed. External load transducers record the axial force applied and strain gauges mounted on the outer perimeter of the tube record the radial strain. The cross-section of this set-up can be seen in Figure 1.1. It is important to note that the strain is not directly measured on the sample but rather the strain is transferred through the wall of the cylinder where it is recorded using, for example, a strain gauge. Furthermore, the axial displacement is recorded using a linear variable differential transformer (LVDT). This experimental set-up is simple in the sense that it does not require multiple sensors and instruments to obtain various stress states of the material tested.

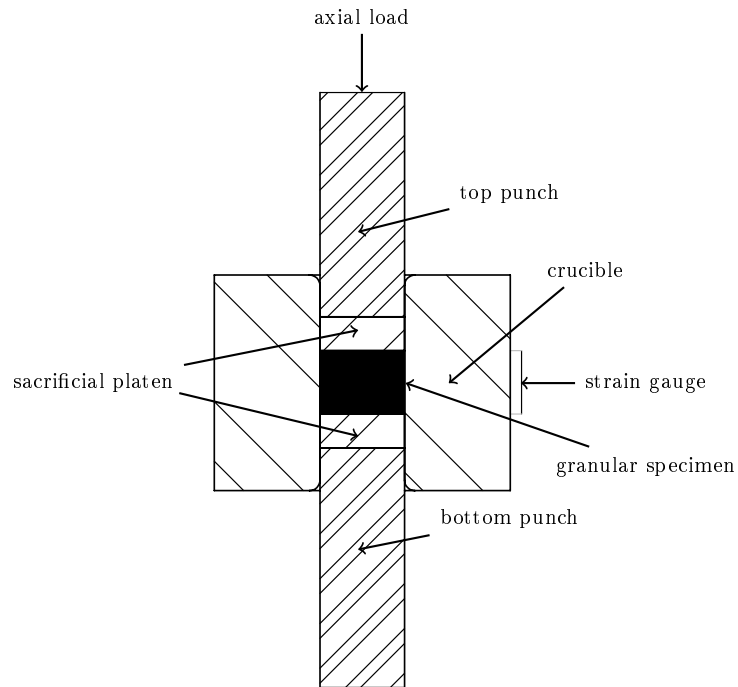


FIGURE 1.1: The cross-section of the TWC apparatus shows the void holding the specimen along with the external instruments required to capture the material behaviour during compaction. This testing configurations can accommodate a range of material amounts depending on required axial load.

1.2.2 Instrumented Die - Confined Uniaxial Compaction

The next common experimental apparatus is the instrumented die. This method has been previously used by researchers in the product manufacturing field [63–65] and compaction modelling research [66]. This system is similar to the one mentioned before, however, the pressure measurements are directly measured from the material using various transducers illustrated in Figure 1.2. This provides a simple system for measuring simultaneously data and material properties in the course of compaction [66].

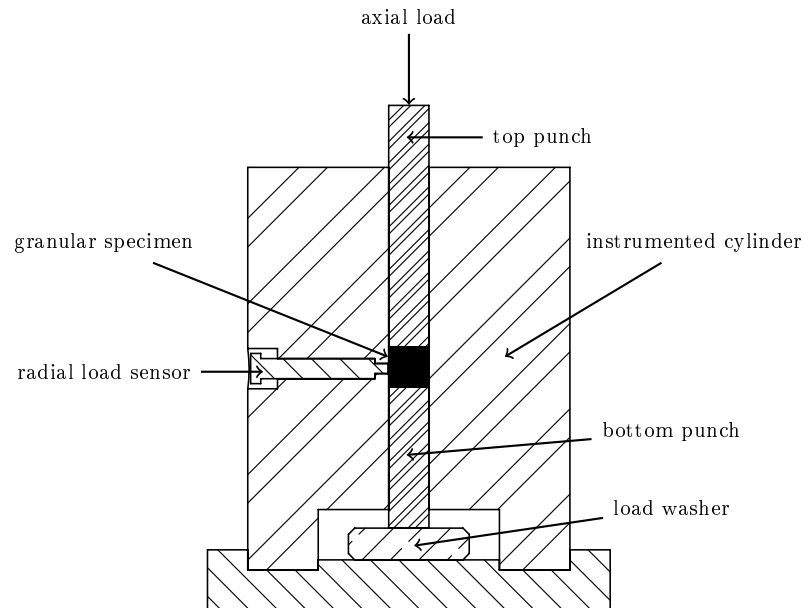


FIGURE 1.2: An adapted sketch of the instrumented die which directly measures within the void, simultaneously capturing constitutive data and material properties [67].

1.2.3 Triaxial Compaction

The last commonly used method to test granular materials is a triaxial compaction system. The apparatus consists of a cylinder, confining pressure chamber, bottom and top punches. Figure 1.3 depicts the cross-section of a typical pressure cell used for experiments. The sample is placed in a double-sealed compression chamber where the outer void is filled with a fluid providing hydro-static pressure while an axial load is applied to the top of the specimen, placing the sample in a uniform stress state. Researchers such as Sridhar and Fleck [68], Chojnacki and Chen [69], Lee and Kim [70] have shown this technique to be effective when validating material models. The testing methods outlined come with increasing costs, where the TWC is most cost effective in comparison to the triaxial apparatus.

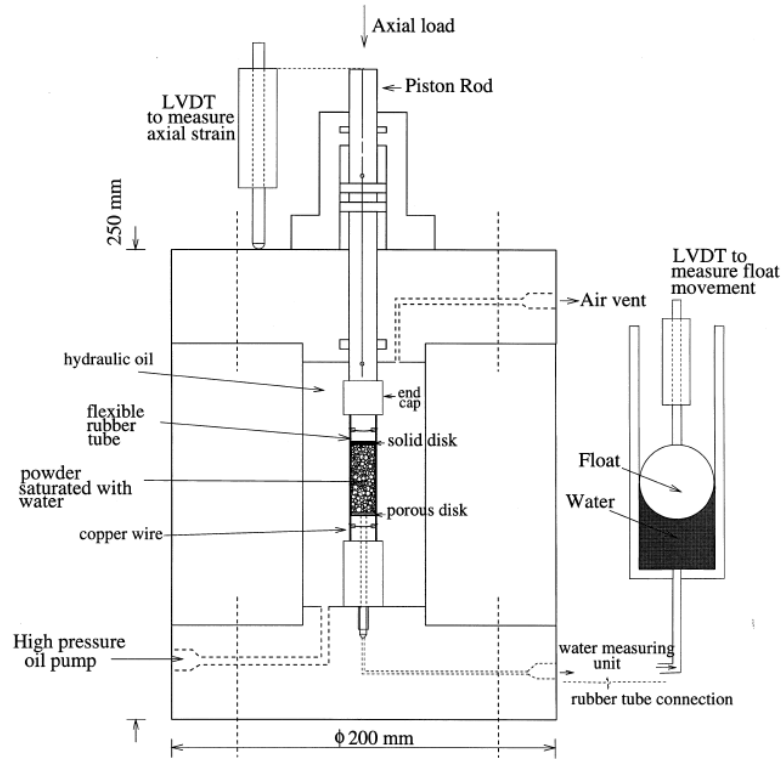


FIGURE 1.3: Sketch of the triaxial pressure cell used for compacting cylindrical powder specimens of diameter 12.7 mm for probing the yield surface [68].

1.3 Thesis Objectives

To better understand the behaviour of granular materials for defence and other applications, the shortcomings of powder flowability, particle variability, and particle performance relating to material strength must be addressed and understood [71]. Overall, the importance of fracture and fragmentation on the impact performance of ceramics [33, 38, 62, 72, 73] and metallics [74, 75] has been well documented in the literature. Building on these past works, the objectives of this thesis explore the behaviour of granular stainless steel 316, alumina, and boron carbide with an emphasis on the effect of particle size and shape on flow behaviour and variability in strength, bulk modulus, and frictional effects. A quasi-static experimental technique ($\dot{\epsilon}$ of 10^{-1}s^{-1}) is used to evaluate the triaxial flow stress as a function of particle size and, where applicable, shape. Before and after experiments, scanning electron microscopy (SEM) is used to investigate failure, fracture, and fragmentation mechanisms in the materials. Lastly, additional thoughts were focused on looking at curve fitting where specific attention was given to parameterize individual constants of the trends observed in the hydro-static response

of material density. By addressing these areas, advancements will be obtained to better understand the effects of particle size and shape on strength and failure of granular materials.

1.4 Thesis Goals

The goals of this thesis are as follows:

- ▶ Design a feasible compaction apparatus to test the various granular materials, taking into account the individual material difference.
- ▶ Study the particle-sized dependant hydro-static response of granular materials as a function of porosity of all three materials, relating the failure mechanisms occurring during quasi-static compaction.
- ▶ Study the particle size effects of the secant bulk modulus as a function of applied stress for granular stainless steel 316. This material is a popular choice in the defence industry for armour design.
- ▶ Study the particle size effects of the secant bulk modulus as a function of hydro-static pressure for granular alumina (Al_2O_3) and boron carbide (B_4C). These advanced ceramics are currently used in armour.
- ▶ Study the friction effects of confined compression observing particle size dependencies.
- ▶ Investigate the failure mechanisms occurring during confined quasi-static compression of granular stainless steel 316, alumina, and boron carbide.

1.5 Contributions

The contributions from this thesis are summarized in the following statements:

- ▶ Verifying the instrumented die experimental apparatus for consistent material response, and characterization.

- ▶ Particle geometry and distribution affect the quasi-static compression response, which dictates the failure path of the granular material.
- ▶ Noting the fragmentation and failure evolution happening at various porosities in granular stainless steel 316, alumina, and boron carbide which relates the material's sensitivity of strength and bulk modulus on fragment size. Such information is paramount in improving material design for additive manufacturing and ballistic protection.
- ▶ Experimental data presented in this thesis can be used in validating failure models and yield surfaces, underlining the particle-size dependant trends observed in stainless steel 316, Al_2O_3 , and B_4C .

These contributions are incorporated and discussed in detail in two journal papers that were published as an outcome of this thesis work.

1.6 Thesis Structure

The layout of this thesis will have the following structure: Chapter 2 provides a literature review of the derivation of fundamental material laws on which this work stands upon. The first compaction experiment is introduced in Chapter 3, where granular stainless steel 316 was compacted using the thick-walled cylinder (TWC) approach. Chapter 4 describes the second compaction experiment where granular alumina and boron carbide were compressed using the instrumented die approach. Further, the conclusions of this research are written in Chapter 5, where future work and recommendations are outlined. Lastly, the MATLAB code used to derive material characteristics can be found in Appendix A, uncertainty analysis and propagation of error can be found in Appendix B, before and after experiment SEM images can be found in Appendix C, theoretical equations and material laws can be found in Appendix D, supplementary material on curve fitting of material constants can be found in Appendix E, and the author's academic biography can be found in Appendix F.

Chapter 2

Theory of Mechanics of Granular Materials

This chapter is dedicated to establish the fundamental ground work of the theoretical laws that govern elastic behaviour of materials. In the following chapter, the law of elasticity is introduced and converted into the form which was used in determining the compaction behaviour of the material.

2.1 3D Hooke's Law

The relationships that are obtained from the experiments performed in this thesis stem from Hooke's law that describes the phenomenon of elasticity. The idea exists that when a material is loaded externally, deformation takes place. Hooke's law for linear elastic materials in Cartesian coordinates can be described as:

$$\sigma_{ik} = C_{iklm}\varepsilon_{kl} \quad (2.1)$$

where σ_{ik} is the second order stress tensor with its individual elements, ε_{kl} is the second order strain tensor with its individual elements, and C_{ijkl} is the fourth order stiffness tensor composed of stiffness coefficients [76]. A complete derivation of this relationship has been computed extensively in literature and, therefore, will not be explicitly shown (see reference [76, 77]). The stress components are symmetric based on the condition

that $\sigma_{ij} = \sigma_{ji}$ and $C_{ijkl} = C_{jikl}$, and therefore, the number of independent constants reduce from 81 to 54. Furthermore, the same symmetric relations can be applied to the strain components ($\varepsilon_{ij} = \varepsilon_{ji}$), thus for linear elasticity we get 36 independent constants and (2.1) reduces to the following:

$$\sigma_i = C_{ij}\varepsilon_j \quad \text{where } i = 1, 2, \dots, 6 \quad (2.2)$$

It is important to note that the plain strain assumption holds due to the cylindrical shaped body where the loads are applied in the z -direction. Furthermore, we assume that the surface tractions and body forces are independent of z . To further reduce the stiffness matrix, we assume that the material is isotropic and the elasticity matrix is expressed as follows:

$$\begin{bmatrix} \sigma_1 \\ \sigma_2 \\ \sigma_3 \end{bmatrix} = \begin{bmatrix} C_{11} & C_{12} & C_{13} \\ & C_{22} & C_{23} \\ \text{sym} & & C_{33} \end{bmatrix} \begin{bmatrix} \varepsilon_1 \\ \varepsilon_2 \\ \varepsilon_3 \end{bmatrix} \quad (2.3)$$

where σ_i ($i = 1, 2, 3$) is the stress tensor in the three principle directions, C_{ij} ($i, j = 1, 2, 3$) is the stiffness tensor in 3-D space, and ε_i ($i = 1, 2, 3$) is the strain tensor in the three principle directions. Refer to Appendix D for full derivation of the stress strain relation. The constitutive equations written in Cartesian coordinates are summarized as follows:

$$\begin{aligned} \sigma_{11} &= \frac{E}{(1+\nu)(1-2\nu)} [(1-\nu)\varepsilon_{11} + \nu(\varepsilon_{22} + \varepsilon_{33})] \\ \sigma_{22} &= \frac{E}{(1+\nu)(1-2\nu)} [(1-\nu)\varepsilon_{22} + \nu(\varepsilon_{33} + \varepsilon_{11})] \\ \sigma_{33} &= \frac{E}{(1+\nu)(1-2\nu)} [(1-\nu)\varepsilon_{33} + \nu(\varepsilon_{22} + \varepsilon_{11})] \\ \sigma_{12} = \sigma_{21} &= \frac{E}{1+\nu}\varepsilon_{12} \\ \sigma_{13} = \sigma_{31} &= \frac{E}{1+\nu}\varepsilon_{13} \\ \sigma_{23} = \sigma_{32} &= \frac{E}{1+\nu}\varepsilon_{23} \end{aligned}$$

Furthermore, Hooke's law was derived in terms of cylindrical coordinates to represent the sample geometry used in the experiments. Hooke's law in cylindrical coordinates for 3-D space can be interpreted as the following:

$$\begin{bmatrix} \sigma_r \\ \sigma_z \\ \sigma_\theta \end{bmatrix} = \begin{bmatrix} C_{11} & C_{12} & C_{13} \\ & C_{22} & C_{23} \\ \text{sym} & & C_{33} \end{bmatrix} \begin{bmatrix} \varepsilon_r \\ \varepsilon_z \\ \varepsilon_\theta \end{bmatrix} \quad (2.4)$$

where σ_j ($j = r, z, \theta$) is the stress tensor in the principle direction using cylindrical coordinates, C_{ij} ($i, j = 1, 2, 3$) is the stiffness tensor in 3D space, and ε_i ($i = r, z, \theta$) is the strain tensor using in the principle directions using cylindrical coordinates. The complete derivation of the stiffness relationship has been extensively studied in the past [78] and is summarized in Appendix D. These mathematical relationships are used to convert the measured quantities in the experiments, into material parameters that allow for an understanding in the material behaviour and failure during compaction. The explicit form of the stress tensor is written as follows:

$$\begin{aligned} \sigma_r &= \frac{E(1-\nu)}{(1+\nu)(1-2\nu)} [(1-\nu)\varepsilon_r + \nu\varepsilon_\theta] \\ \sigma_\theta &= \frac{E(1-\nu)}{(1+\nu)(1-2\nu)} [(1-\nu)\varepsilon_\theta + \nu\varepsilon_r] \\ \sigma_z &= \frac{E\nu}{(1+\nu)(1-2\nu)} [\varepsilon_r + \varepsilon_\theta] \\ \tau_{r\theta} &= \frac{E}{1+\nu} \varepsilon_{r\theta} = 2G\varepsilon_{r\theta} = G\gamma_{r\theta} \\ \tau_{rz} &= \tau_{\theta z} = 0 \end{aligned}$$

Using these constitutive equations summarized above, the hydro-static stress component can be determined which is used to relate the material's compressive strength.

Chapter 3

Confined Uniaxial Compression of Granular Stainless Steel 316^a

This chapter is dedicated to explaining the compression experiment conducted in determining the material characterization of stainless steel 316 powder. In the following, the material characterization is explained, the experimental apparatus is described and illustrated, experimental results are interrupted, and material failure is discussed.

3.1 Material Composition and Geometry

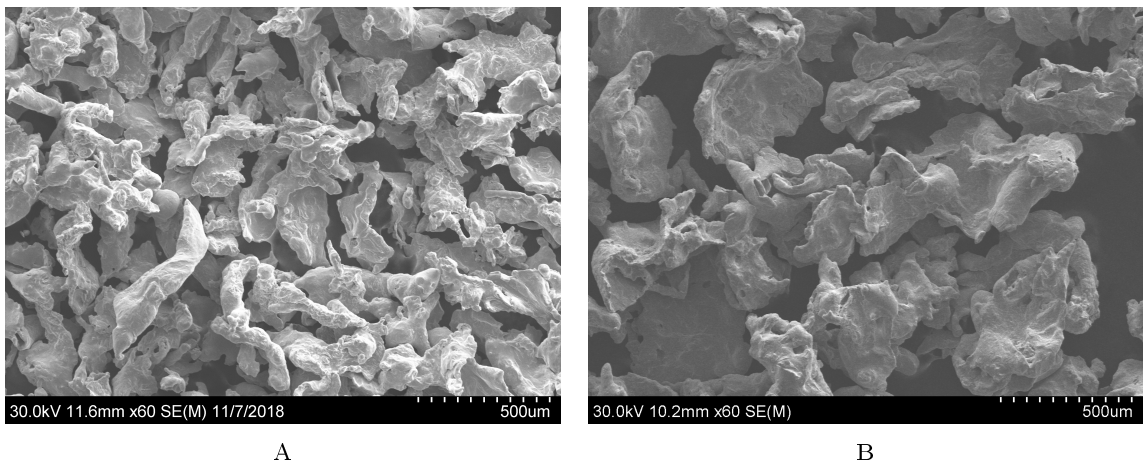
Stainless steel 316 powder was used in the experiment and the elemental composition was provided by the manufacturer and is summarized in (Table 3.1). The elemental breakdown is typical for this metal. The powder was sourced from Alfa Aesar by Thermo Fisher Scientific of Tewksbury, Massachusetts.

The stainless steel 316 powders used for the uniaxial compaction, range from 127 μm to 487 μm in size and exhibit a rough irregular shape. This is most likely due to the manufacturing process of using water atomization to create the powder [79]. For visual aid, SEM images were taken and the powder geometry is illustrated in Figure 3.1 for sieved particle sizes: $309 \pm 88 \mu\text{m}$ and $487 \pm 98 \mu\text{m}$. The images were taken with a Hitachi S-4800 Field Emission Scanning Electron Microscope.

^aInformation in this chapter has been published in: P. Nicewicz, T. Sano, J.D. Hogan, “Confined Uniaxial Compression of Granular Stainless Steel 316”. Powder Technology. Manuscript number: POWTEC-D-18-03323R1. Article reference: PTEC14359.

TABLE 3.1: Chemical composition of Alfa Aesar stainless steel 316 powder.

Element	% Mass
C	0.022
Cr	16.860
Mo	2.200
Mn	0.100
P	0.019
S	0.011
Ni	11.190
Si	0.730
Fe	0.0001

FIGURE 3.1: SEM images of the stainless steel 316 powder at two different particle sizes: A $127 \pm 34 \mu\text{m}$ and B $487 \pm 98 \mu\text{m}$, respectively.

3.2 Particle Distribution

Three different sizes were sieved, microscopically analyzed, and tested to observe the effects of mean particle diameter, (μm), on hydro-static pressure as a function of porosity. The mean and standard deviation was documented for each particle size for the range of: $127 \pm 34 \mu\text{m}$, $309 \pm 88 \mu\text{m}$, and $487 \pm 98 \mu\text{m}$, summarized in Table 3.2. The particle sizes were chosen based on the restrictions of the crucible design and access to materials with a higher Rockwell hardness. Every specimen tested was separately analyzed and sampled following principal sampling techniques for granular material outlined by Maynard [80].

The particle size distribution and shape was analyzed using the automated Malvern Morphologi G3 microscope (G3). The De Broukere mean diameter (volume moment mean diameter) was considered when analyzing the particle sizes. This parameter is

most relevant when determining the distribution of the bulk sample used in experiment and has been used by many in literature [81, 82]. The definition of this relation is on the basis of introducing another linear term in diameter, analogous to moments of inertia i.e. accounts for the centre of gravity of the particle distribution. The next point to underline is that the advantage of this method does not require the particle count. This was done by taking the square difference of the upper and lower bin to determine D_i which determined the mean particle distribution in the sample. The numerator is taken to the power of four (the power of three to account for the equivalent volume and the additional power to account for the centre of gravity) and the denominator is taken to the power of three (where it accounts for the mass of the particles). Seen below is the summarized equation:

$$D[4, 3] = \frac{\sum_1^n D_i^4}{\sum_1^n D_i^3} \quad (3.1)$$

To evaluate the variability of the powder, the span Δ , was calculated for each sample, as was similarly used by Engeli et al. [83]. The span was determined through the following and this takes into account the tenth (D_{10}), fiftieth (D_{50}), and ninetieth percentile (D_{90}):

$$\Delta = \frac{D_{90} - D_{10}}{D_{50}} \quad (3.2)$$

The particle size based on (3.1) and the span of the distribution based on (3.2) are summarized in Table 3.2. With an increase in mean particle diameter, the standard deviation increases while the span decreases, highlighted in Table 3.2. These particle statistics are considered later when mechanical behaviour is investigated.

TABLE 3.2: Particle size characterization observing the diameter distribution and circularity of each particle.

\emptyset [μm]	D_{10} [μm]	D_{50} [μm]	D_{90} [μm]	Δ	C
127 ± 34	94	125	169	0.601	0.77 ± 0.12
309 ± 88	233	314	364	0.417	0.64 ± 0.13
487 ± 98	413	480	549	0.283	0.63 ± 0.15

Particle shapes were also considered. Shown in Table 3.2, the average circularity, C , of the particles decreases as the average particle size increase. Circularity refers to how close the particles resemble a perfect sphere ($C = 1$). Less circular particles have a larger

deviation in the particle size. The circularity of the material is directly related to the manufacturing process such that the method of atomization dictates the final shape of the particle [79]. Here we computed particle circularity (C) defined as:

$$C = 2\sqrt{\frac{\pi A}{p}} \quad (3.3)$$

where A (m^2), and p (m), are the area and perimeter of the particle, respectively. As the particles increase in mean diameter the circularity decreases. The shape results are important because as noted by Schade et al. [16] the decrease in circularity causes the particles to align in other orientations and ineffectively fill in the voids. Schade et al. [16] determined that the difference in circularity is related to the atomization process of the granular material i.e. gas atomization produces spherical shaped particles and water atomization produces rough, irregular particles.

3.3 Experiment Configuration

3.3.1 Thick-walled Cylinder (TWC)

Illustrated in Figure 3.2 is a schematic of the experimental apparatus used to conduct confined uniaxial compression experiments on the granular material to obtain a triaxial response. The top punch, bottom punch, and sacrificial platens were fabricated from D2 tool steel and were heat treated using quenching and double tempering to reach a hardness of 62 HRC. The punches are used to press together the sacrificial platens that contact the granular material. The top and bottom punches are designed around the accessibility of the MTS 810 machine used in this study, and are 130 mm in length. The crucible was made out of 4340 steel and heat treated by quench and tempering followed by gas nitriding. The maximum hardness achieved was 52 HRC with an inner and outer diameter of 6.3 mm and 22.2 mm, respectively. The inner diameter was machined with a tight tolerance so that the sacrificial platens were able to seal in the granular material and to protect the punches from the granular media. The supporting beam, designed out of aluminum, was placed to differentiate between the normal forces on the top and bottom of the sample. The support beam was held up with aluminum blocks that attach to the MTS. Aluminum supports were designed for attaching the linear variable differential

transformer (LVDT) so that relative displacement could be recorded to minimize the deflection during compression. The operating parameters for the LVDT were ± 7.5 mm and 0.2% linearity error. The MTS machine outputs the applied load at a rate of 0.33 kN s^{-1} with a resolution of $305 \mu\text{V}$ per analogue-to-digital converter count, placing the specimen in a quasi-static stress state. Between the top punch and the crucible is a load washer from Omega Engineering Inc. The operating parameters for the load washer was 10 kN with an accuracy of $\pm 0.5\%$.

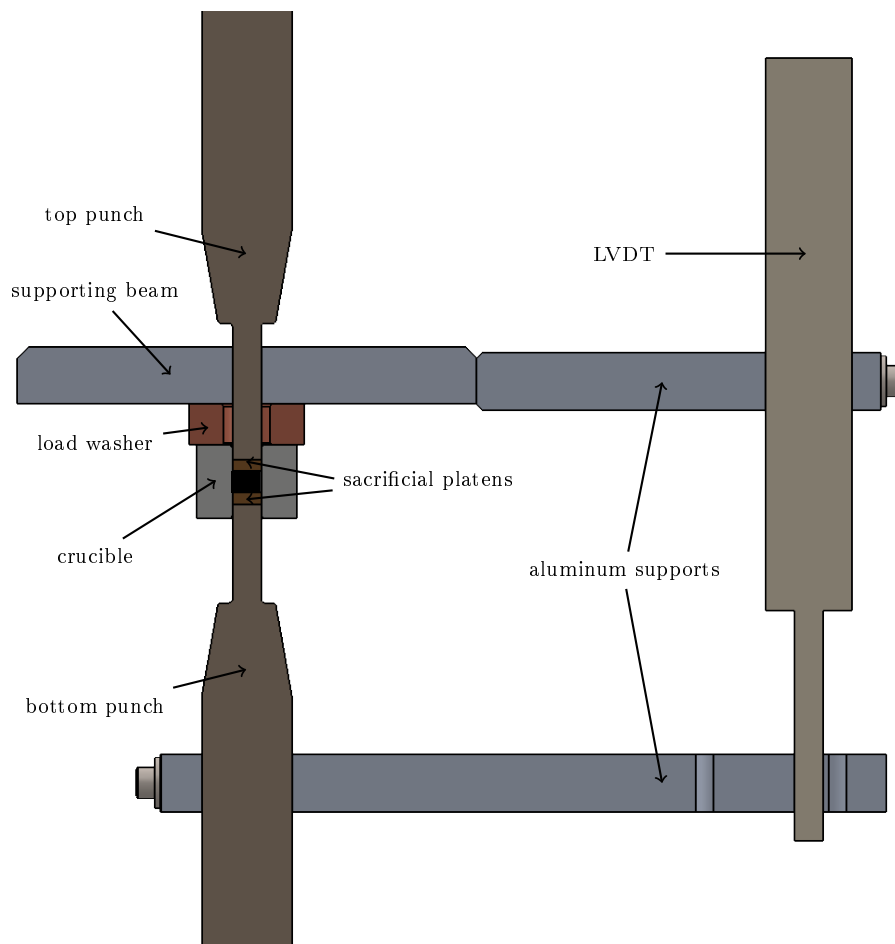


FIGURE 3.2: Schematic of the cross-section of the experimental set-up illustrating key components and dimensions. Due to the nature of the compression machine, the load was applied from the bottom.

For specimen preparation, one end of the crucible was closed using the sacrificial platen and punch. In order to limit the wall frictional effects occurring during confined compaction it is critical to maintain an aspect ratio of height to width of < 1 when determining the sample size [84]. Granular material was poured in and an aspect ratio of

0.76 ± 0.05 was achieved. The volume of material needed to satisfy this constraint is $150.8 \pm 3.3 \text{ mm}^3$. Sample volume was not the same for all samples and the uncertainty reflects the variation.

The supporting beam illustrated in Figure 3.2 creates a free floating state such that the compaction of the material is not affected by the weight of the crucible. The top punch was lowered, rested against the sacrificial platen on the top of the specimen with the assumption that the specimen has not been compacted. The LVDT was secured to the beam, so that the compaction depth could be measured relative to the displacement. The load washer was used to measure the combined frictional effects during the uniaxial compression.

3.3.2 TWC Theory

To better understand the response of the granular material during quasi-static confined uniaxial compression, we investigate the relationship between the hydro-static pressure and porosity by tracking the volumetric strain and relative density in the crucible. First, we track the time-evolving reduction in porosity of our test samples through measurements of initial mass m (kg), initial packing porosity ϕ_i (%), and the cross-head displacement δ (mm) of the punch that is used to compress our granular samples. The mass of the initial granular sample is measured by a digital scale with the precision of 0.01 g. The size of each sample was controlled by volume ($\sim 150.8 \text{ mm}^3$). Throughout the compression experiment, the change in volume, ΔV (m^3), is related to axial displacement:

$$\Delta V = A_0 \delta \quad (3.4)$$

where A_0 is the cross-section area of the void (m^2) and δ is the relative axial displacement during compression (m). From there, we can calculate the specimen density, ρ (kg m^{-3}), as it evolves during compaction:

$$\rho = \frac{m}{V_0 - \Delta V} \quad (3.5)$$

where m is the mass of the specimen (kg), and V_0 is the initial specimen volume (m^3). The evolving porosity is calculated by normalizing the specimen density with the solid bulk density:

$$\phi = 1 - \frac{\rho}{\rho_s} \quad (3.6)$$

where ϕ is the porosity fraction (unit less) and ρ_s is the bulk solid density (kg m^{-3}). For stainless steel the bulk density is taken as 8000 kg m^{-3} , which provided by the manufacturer.

Next, the hydro-static pressure is calculated by measuring the axial stress, σ_z (MPa), from the MTS machine and the radial stress, σ_r (MPa), is calculated from the strain read from the mounted strain gauges on the crucible, see schematic in Figure 3.2 for visual. The equation for hydro-static stress, P (MPa), in cylindrical coordinates is defined as [85]:

$$P = \frac{1}{3} (\sigma_z + 2\sigma_r)$$

where σ_z is calculated by dividing the axial force experienced by the sample, F_z (N), and the cross-sectional area of the void A_0 (m^2), assuming that the area does not significantly deform during compression as underlined by [85]:

$$\sigma_z = \frac{F_z}{A_0} \quad (3.7)$$

σ_z was computed by subtracting the axial force outputted by the MTS machine, F_{MTS} (N), and the friction forces, F_f (N), induced by the sacrificial platens and granular powder contacting the crucible walls:

$$F_z = F_{MTS} - F_f \quad (3.8)$$

To determine the radial stress, the crucible was assumed to be a thick walled cylinder (TWC). The TWC equation assumes that the crucible geometry is symmetric on θ ($^\circ$) and the stress is only a function of r (m). The problem is statically determinate and

so only the equilibrium equations must be satisfied. The coordinate axis are defined in Figure D.2. The derivation of the equilibrium equations along with the solution have been computed extensively in literature and therefore will not be explicitly shown (see reference [85] and [86] for full derivation). It is, however, summarized in Appendix D for completeness. Equation (3.3.2) can be rewritten to include the axial stress and radial stress to obtain an expression for hydro-static pressure as a function of measurable parameters:

$$P = \frac{1}{3} \left(\frac{F_z}{A_o} + E_c \varepsilon_r \frac{b^2 - a^2}{a^2 (1 - \nu_c^2)} \right) \quad (3.9)$$

where E_c (MPa) is the stiffness of the crucible, ν_c is Poisson's ratio of the crucible, a is the inner radius (m), b is the outer radius (m), and ε_r is the radial strain as a function of thickness. There are, however, limitations of using the TWC approach which has been identified by, for example, Kim et al. [87]. According to their research, shortcomings exists when measuring hoop strain. This is dependent on the inner diameter, cylinder thickness, and location of strain gauge along the axial direction. In our apparatus, the inner diameter is much smaller than the diameter tested by Kim et al. [87], further, when extrapolating from the two sizes that were compared, our void size is proportional to the maximum strain we measured. In addition, the strain gauge size and placement encompassed in our experiment the entire testing section and so we think that some of the uncertainty in the measurements is mitigated.

Next, the bulk modulus equations of the material was derived. This characteristic describes the compressibility of the material and relates the change in pressure of the material with respect to volume. This is given by:

$$B_{ep} = \frac{P}{\frac{\Delta V}{V_o}}$$

where B_{ep} represents the bulk modulus taking into account elastic and plastic behaviour (MPa), and all the other variables have been previously defined. This parameter evolves during loading and is an indicator of deformation in the granular sample. Similar calculations were done by Gustafsson et al. [88] when conducting confined compression experiments with iron ore.

Furthermore, the axial-to-radial effects were considered by calculating the Janssen coefficient of stainless steel powder. This parameter relates the radial and axial stresses during compaction which allows for simplification when conducting computer modelling of the compaction [89]. The Janssen constant, K , is given by:

$$K = \frac{\sigma_r}{\sigma_z} \quad (3.10)$$

Next, we looked at the frictional effects by monitoring the transmitted stress ratio, T (unitless). To do this, we calculated the ratio of transmitted stress, σ_t (MPa), over applied stress, σ_a (MPa). The applied stress, is the stress that the compression machine outputs and the transmitted stress, is the stress that is interpreted from the load washer. The difference in applied and transmitted stresses provides insight on how much energy is lost to friction in the crucible apparatus. This ratio is given by:

$$T = \frac{\sigma_t}{\sigma_a}$$

Lastly, to account for the uncertainty in the experiment, we conducted a systematic propagation of error, taking into account the uncertainty of the sensors and measured geometries. This will help in understand the accuracy of our results. Based on the guide outlined by Berendsen [90], Table 3.3 summarizes the relative uncertainty of critical material parameters that were calculated. The rules for calculating uncertainty have been derived and computed extensively in literature and will not be explicitly shown. Refer to [90] and Appendix B for full derivation and explanation respectively.

TABLE 3.3: Relative systemic error of the minimum and maximum cases for the mechanical properties of stainless steel 316.

Mechanical properties	Particle size 127 um	Particle size 487 um
Initial volume (V_o)	0.77%	0.90%
Porosity (ϕ)	0.97%	0.96%
Hydro-static pressure (P)	11%	10%
Bulk modulus (B_{ep})	12%	2.9%
Janssen coefficient (K)	1.5%	1.7%
Transmission ratio (T)	6.5%	6.6%

3.4 Compaction Results and Discussion

3.4.1 Hydro-static Response

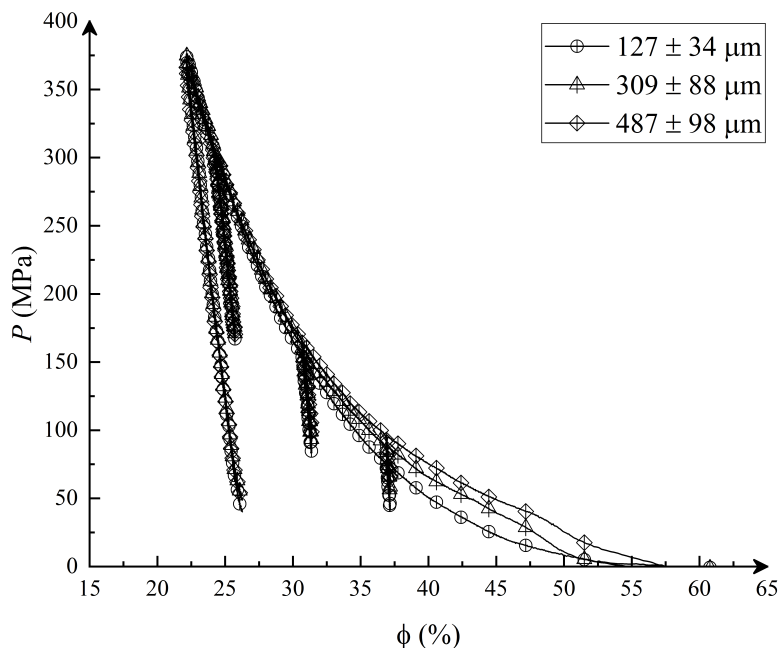


FIGURE 3.3: Quasi-static granular compaction of stainless steel 316 powder for particle sizes of: $127 \pm 34 \mu\text{m}$, $309 \pm 88 \mu\text{m}$, $487 \pm 98 \mu\text{m}$ depicting the load and unload response.

As an outcome of the confined uniaxial compaction, the following aspects were investigated: compressibility, loading path, average particle diameter and geometry of the material. Shown in Figure 3.3 is the relationship between the hydro-static pressure and porosity for three different particle size ranges; $127 \pm 34 \mu\text{m}$, $309 \pm 88 \mu\text{m}$, $487 \pm 98 \mu\text{m}$. The initial porosity for each test was 60 % for size $127 \pm 34 \mu\text{m}$, 66 % for size $309 \pm 88 \mu\text{m}$, and 67 % for size $487 \pm 98 \mu\text{m}$. For porosities above 30 %, smaller particles have lower hydro-static pressure. For porosities less than 30 %, the relationship between porosity and hydro-static pressure collapses onto a single curve for each particle size range studied. Previous work by Heckel [91] noted similar results when studying metallic powders such as iron, nickel, tungsten, and copper. Linear-like trends were observed for compressive stresses applied $>135 \text{ MPa}$.

In addition, no difference in load-unload behaviours are observed across all particle sizes for a given porosity. As the hydro-static pressure is reduced, the effect of unloading results in incremental increases in porosity (the linear curves back to the right). The

uncertainty for the hydro-static pressure parameter was calculated to be 11.3% and 10.9% for the small ($127 \pm 34 \mu\text{m}$) and larger particles ($487 \pm 98 \mu\text{m}$). This deviation was consistent for the particle sizes investigated, which shows that the equipment was consistent through out every test conducted. As a limitation to this work, additional tests should be conducted and a wider range of particle sizes should be included to account for any outlying behaviour.

3.4.2 Bulk Modulus

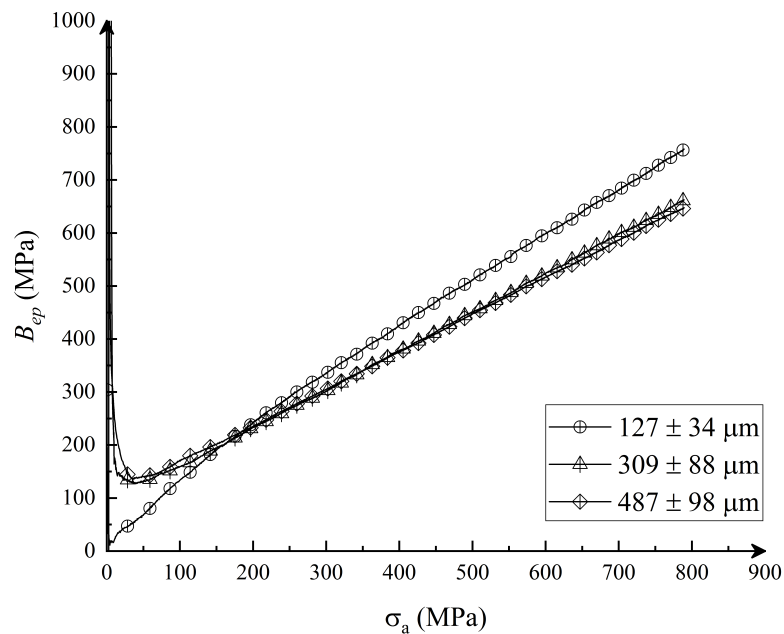


FIGURE 3.4: The bulk modulus of stainless steel 316 as a function of applied stress for particle sizes of: $127 \pm 34 \mu\text{m}$, $309 \pm 88 \mu\text{m}$, $487 \pm 98 \mu\text{m}$.

Next, the bulk modulus was investigated. Shown in Figure 3.4 is the relationship between the bulk modulus (described in Equation (3.3.2)) as a function of the applied stress. This plotting convention is typically seen in literature [92, 93]. This figure accounts for load behaviour carried out during compression. Notable in the figure is that the smaller particle size range reach a higher bulk modulus (760 MPa for $127 \pm 34 \mu\text{m}$) while the larger particles appear to reach a lower value (663 MPa for $309 \pm 88 \mu\text{m}$, and 648 MPa for $487 \pm 98 \mu\text{m}$). Similar studies conducted in the past showed that granular aluminum followed linear trends when loaded with a compressive stress of $>300 \text{ MPa}$ [94]. Interestingly, the aluminum particle trends observed were that larger particles (150 - 212 μm) had a slightly steeper slope than the smaller particles (53 - 75 μm) when

looking at the B_{ep} as function of pressure. The bulk modulus is also more sensitive to the smaller particles (it increases at a faster rate). Propagation of error was likewise completed looking at the B_{ep} . Based on our calculations, the relative uncertainty was 11.7% and 2.9% for the small particle size ($127 \pm 34 \mu\text{m}$) and large particle size ($487 \pm 98 \mu\text{m}$) respectively.

3.4.3 Friction

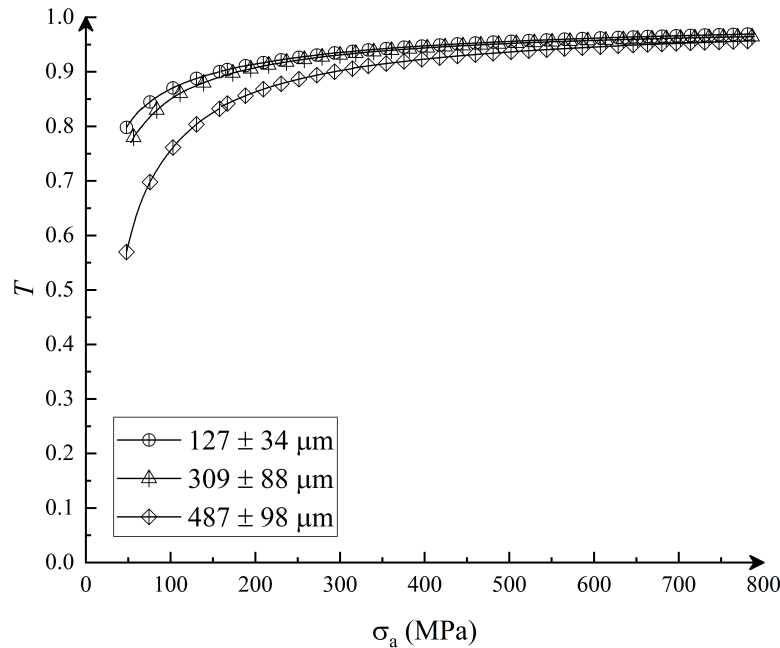


FIGURE 3.5: The transmission ratio relationship of granular stainless steel 316 as a function of applied stress for different particle sizes: $127 \pm 34 \mu\text{m}$, $309 \pm 88 \mu\text{m}$, $487 \pm 98 \mu\text{m}$.

Next, the wall friction effects can be probed by calculating the transmission ratio, which relates to the transmitted force through the material. Shown in Figure 3.5 is the transmission ratio as a function of applied load for all particle sizes. For a given applied stress the transmission ratio decreases for large particle sizes. For lower applied stresses, the values for lower applied stress is related to the compliance of the system. As the applied stress increases, the transmission ratio converges to 0.96. The small particles ($127 \pm 34 \mu\text{m}$) approach convergence faster in comparison to larger particles ($487 \pm 98 \mu\text{m}$). To account for the systematic error in the experiment, the uncertainty was calculated. For the small particles ($127 \pm 34 \mu\text{m}$) the relative uncertainty was 6.5% and for the large particles ($487 \pm 98 \mu\text{m}$) the relative uncertainty was 6.6%.

3.4.4 Janssen Coefficient

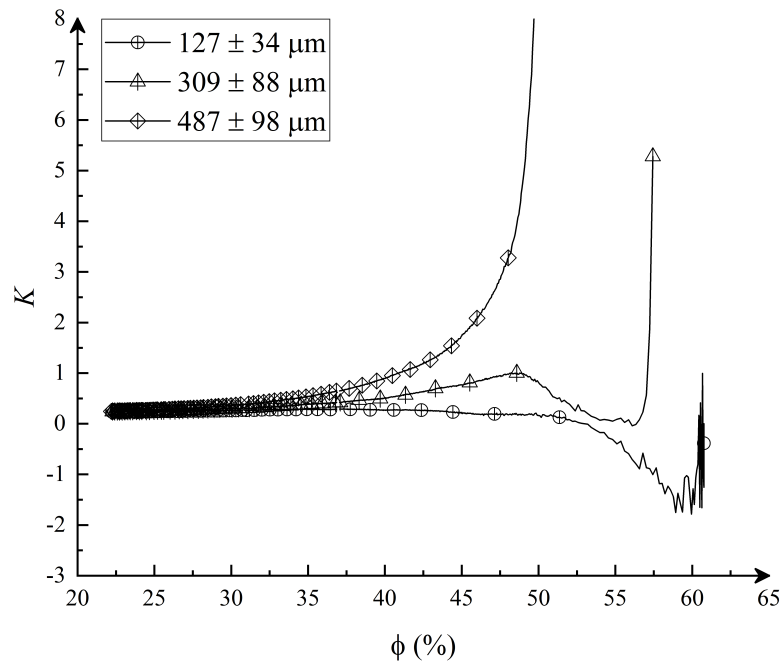


FIGURE 3.6: Janssen coefficient of stainless steel 316 as a function of porosity for varying particle sizes: $127 \pm 34 \mu\text{m}$, $309 \pm 88 \mu\text{m}$, $487 \pm 98 \mu\text{m}$.

Furthermore, we investigate the Janssen coefficient which is used to relate the axial to the radial stresses which helps in simplifying analytical models when simulating triaxial compression behaviour. Shown in Figure 3.6 is the relationship between the porosity and the Janssen coefficient for three particle size ranges. At higher porosity there is more variability in the Janssen coefficient across and within each particle size range. Specifically, larger particles have a higher Janssen coefficient for larger porosities. As the porosity is crushed out, (i.e reduced), the Janssen coefficient for all particle size ranges, converges to 0.23 (near 30% porosity). The typical range for the Janssen constant seen in bulk materials has been noted to be 0.3-0.6 by [95]. These values are typically seen in round-like particle shapes and so the interesting behaviour seen in Figure 3.6 is dependent on the elongated and rough edged particles. The relative uncertainty for the Janssen coefficient was 1.5% and 1.7% for the small ($127 \pm 34 \mu\text{m}$) and larger ($487 \pm 98 \mu\text{m}$) particles respectively.

3.4.5 SEM Images of Material Failure

Lastly, SEM images were taken of the consolidated stainless steel powder to investigate failure features on the compacted specimen's surfaces. Attempts were made to cut and polish the consolidated pucks after testing, but that only introduced further damage to the specimens. Shown in Figure 3.7A is the failure surface of the $309 \pm 88 \mu\text{m}$. This demonstrates that these particles withstood significant plastic deformation. Elongated laminate structures are noted (red arrows) on the surface, which are believed to be generated from particle shear stress during compaction. Shown in Figure 3.7B is the failure surface of the larger particles ($487 \pm 98 \mu\text{m}$). There is noticeably more fracturing and cracking (red arrows) and the surface appeared to be more jagged in comparison to the smaller particles. Such evidence has been noted before by Roberts and Rowe [96]. Based on theoretical equations and experimental evidence, larger particles crack because the stress required for brittle fracture is less than the stress required for plastic flow. Likewise, smaller particles undergo plastic deformation due to the stress required is lower than the brittle deformation stress.

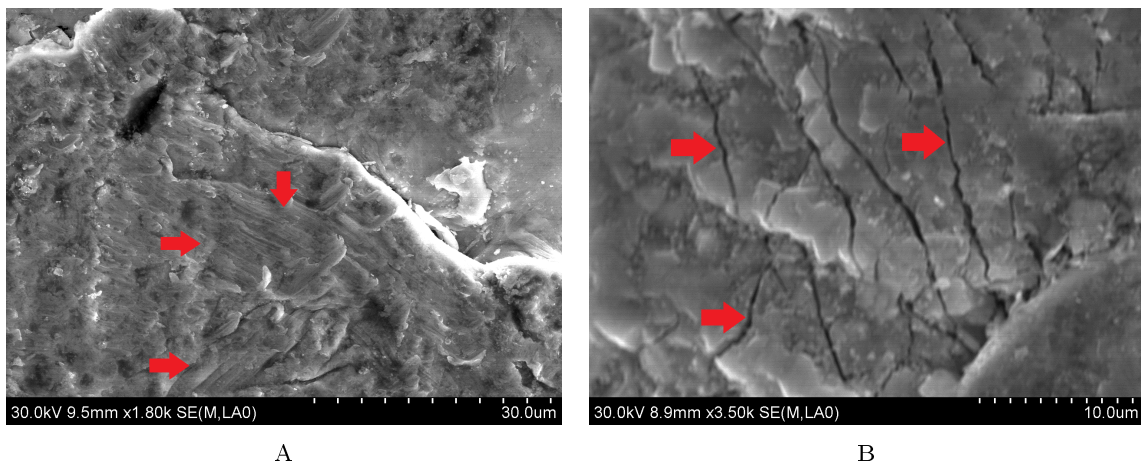


FIGURE 3.7: SEM images of the stainless steel 316 powder at two different particle sizes: position A $127 \pm 34 \mu\text{m}$ and position B $487 \pm 98 \mu\text{m}$ respectively. The red arrows indicate the failure within the material post-compaction.

3.4.6 Discussion and Summary

In this study, the mechanical response of granular stainless steel 316 was investigated for size ranges of: $127 \pm 34 \mu\text{m}$, $309 \pm 88 \mu\text{m}$, and $487 \pm 98 \mu\text{m}$. To accomplish this, a uniaxial compression experiment was adapted, utilizing equipment and sensors: MTS

810, loader washer, displacement LVDT, and strain gauges. Similar experiments have been performed in the powder metallurgy and defence industries [42, 44, 45, 97–99], but limited data exists for stainless steel 316. Similar work has been noted by Roberts and Rowe [96] that larger particles tend to fracture while smaller particles tend to plastically deform. Limitations to this work have been observed and noted. The use of (3.9) is limited based on the assumption of uniform radial stress and negligible friction. Kim et al. [87] underlined the limitations of our approach, using the TWC method. The other limitation of our design was the wall thickness of the crucible which would allow for a narrow range of radial strain. The result of this would be decreased range in strain measurements. To resolve the issue additional calibration tests could be done. Furthermore, the design of the crucible was based on the assumption that the radial stress is uniform which would result in having the specimen friction-free. However, we mitigated this issue by having the length of the strain gauge encompass the entire height of the specimen. Additional thought is given to the design parameters and so further calibration testing will be conducted to narrow the variability of the results and to validate the simplification of (3.3.2) from 3D to 2D space as highlighted by Meyer and Faber [42]. To better validate the material behaviour, additional tests could be conducted to eliminate the outlying trends.

First the relationship between hydro-static pressure and porosity as a function of particle size was investigated. Other researchers have also looked at hydro-static pressure effects on granular material [45, 100]. In our experiments (Figure 3.3), it was observed that deviations in the hydro-static pressure among the particle sizes were sensitive for porosities greater than 30%. For porosities less than 30%, the behaviour converges independent of particle size. This behaviour has been observed before [101] when studying low carbon stainless steel 316 and the result was determined that densification of the material was sensitive to particle size. Cristofolini et al. [101] also demonstrated that initial porosity of the material highly influenced the loading path and that force dissipation during loading mostly originated from wall friction. These behaviours of granular stainless steel 316 have previously not been greatly considered or linked back to global granular response. These linkages are believed to be valuable contributions in the additive manufacturing and other powder based industries. When calculating the uncertainty in porosity for the smallest and largest average particle sizes, values of 0.97% for the $127 \pm 34 \mu\text{m}$ size and 0.96% for the $487 \pm 98 \mu\text{m}$ were obtained.

Despite general insensitivities in particle size influence on the relationship between porosity and hydro-static pressure, it was observed that the bulk modulus was sensitive to particle size (Figure 3.4). In experiment, smaller particle sizes had higher bulk stiffness, were more sensitive to applied stress. Indeed, similar experiments [102, 103] demonstrated that particle size and compaction pressure influenced the mechanical response of the material. More importantly, the particle distribution with particles of different sizes required less energy to compact. In our experiments the ranging particle sizes dictated the mechanical response differences, which is observed to be associated with failure. Specifically, smaller particles ($127 \pm 34 \mu\text{m}$) undergo more plastic deformation (Figure 3.7A) as a consequence of compaction, while the larger particle ($487 \pm 98 \mu\text{m}$) exhibits more fracture and micro-cracking (Figure 3.7B). Note that these particle size-dependent trends have been noted in other fields [53, 104, 105], and in particular this brittle-ductile transition behaviour has been noted by Roberts and Rowe [96].

In addition to bulk response, the stress transmission ratio monitored the frictional behaviour in compaction of granular stainless steel. In order to maximize the stress transmission through the material and minimize wall effects, the samples must maintain an aspect ratio of < 1 . Referring to Figure 3.5, the transmission ratio for the smaller particles ($127 \pm 34 \mu\text{m}$), the curve begins a steep climb and later plateaus as the applied stress increases. Similar research conducted by Fleck and Cocks [84], showed that increasing the aspect ratio beyond 1 resulted in a significant decrease in the stress transmission. This leads us to better replicating an isotropic compaction environment. Other studies conducted by Perez-Gandarillas et al. [106] underlined the idea that lower axial transmission was observed with an increase in particle size. They concluded that part of the loading energy was consumed by the breakage of larger particles. Tracking these relationships allows for a better understanding of the complex behaviour of fragmentation that could lead to more accurate failure modelling. Expanding on the idea of friction, additional research referencing frictional effects have been investigated by Staf et al. [64], where they determined the frictional coefficient, of granular ceramics, was a function of pressure. They determined that particle size and distribution were key factors in the compactability of a material. In contrary, as a result of larger particle geometry, the slope in the curve for the larger particles ($487 \pm 98 \mu\text{m}$) in our experiments is shallower and does not increase as abruptly.

Lastly, the Janssen-Walker theory [107] was explored. The Janssen coefficient is often

used to simplify the relationship of granular stresses experienced in the axial and radial directions, so that the complex behaviour can be simplified and implemented, for example, in existing material models to predict granular failure. Yousuff and Page [108] has shown this radial-axial relationship when studying iron powders. From the experiments a conclusion can be made that for all three particle sizes tested the Janssen coefficient converged to a value of 0.23 (Figure 3.6). This explains that the radial wall stress was approximately 1/5 of the axial load regardless of the particle size. It was also observed that more variability exists for larger particle sizes ($487 \pm 98 \mu\text{m}$) and porosities (+50%). Altogether limited research exists on particle size dependencies and the observation highlights the importance of studying particle variability when researching granular metals. The idea of incorporating length scales into failure modelling, reduces the variability in predicting material behaviour, but more importantly advances the forefront of powder material design.

3.4.7 Concluding remarks

Using this confined uniaxial compaction technique, triaxial characteristics of granular stainless steel 316 as a function of ranging particle sizes was investigated. The results showed an influence of particle size in the compaction curves and the bulk modulus was sensitive to particle size. It is believed to occur due to the failure mechanism that are likely related to the particle size, shape, and initial porosity. Further research must be conducted to better understand and classify the failure regimes occurring in the material.

Chapter 4

Quasi-static Confined Uniaxial Compaction of Granular Alumina and Boron Carbide^a

This chapter is dedicated to explaining the confined uniaxial compression experiment conducted in determining the material response of granular Al_2O_3 and B_4C . In the following, material characterization is explained, the experimental apparatus is described and illustrated, experimental results are interrupted, and material failure is discussed.

4.1 Material Composition and Geometry

Alumina and boron carbide powder was used in the experiment and was purchased from Panadyne Inc, Montgomeryville, Pennsylvania. The average particle sizes for Al_2O_3 used for the uniaxial compaction were four different size ranges: $133 \pm 38 \mu\text{m}$, $201 \pm 42 \mu\text{m}$, $290 \pm 52 \mu\text{m}$, and $414 \pm 57 \mu\text{m}$. Likewise, the average particle size range for B_4C consisted of: $152 \pm 26 \mu\text{m}$, $171 \pm 23 \mu\text{m}$, $303 \pm 46 \mu\text{m}$, and $461 \pm 44 \mu\text{m}$. These particles sizes were determined using the PartAn 3D Dynamic Image Analyzer, and the sampling methods and other particle characteristics are subsequently discussed.

^aInformation in this chapter was submitted for publication in: P. Nicewicz, P. Peciar, O. Macho, T. Sano, J.D. Hogan. "Quasi-static Confined Uniaxial Compaction of Granular Alumina and Boron Carbide Observing the Particle Size Effects". Journal of the American Ceramic Society. *Under review*. Manuscript number: JACERS-44392

4.1.1 Alumina

To study the particle shape, size features before experiments, and the failure after experiments of Al_2O_3 , the Zeiss EVO MA10 Scanning Electron Microscope (SEM) was used and the samples were coated with gold/palladium at 4 nm to improve the quality of the images taken. Shown in Figure 4.1A is an SEM image of Al_2O_3 powder ($133 \pm 38 \mu\text{m}$) before the experiment. The overall geometry appears to be elongated with sharp edges with an average aspect ratio (width to height) of 0.2. There is also some minor porosity in the fragments. These shape and porosity features are consistent across all fragment sizes for alumina used in this study. Note, the other images in Figure 4.1 are discussed later in Section 4.4.3.1.

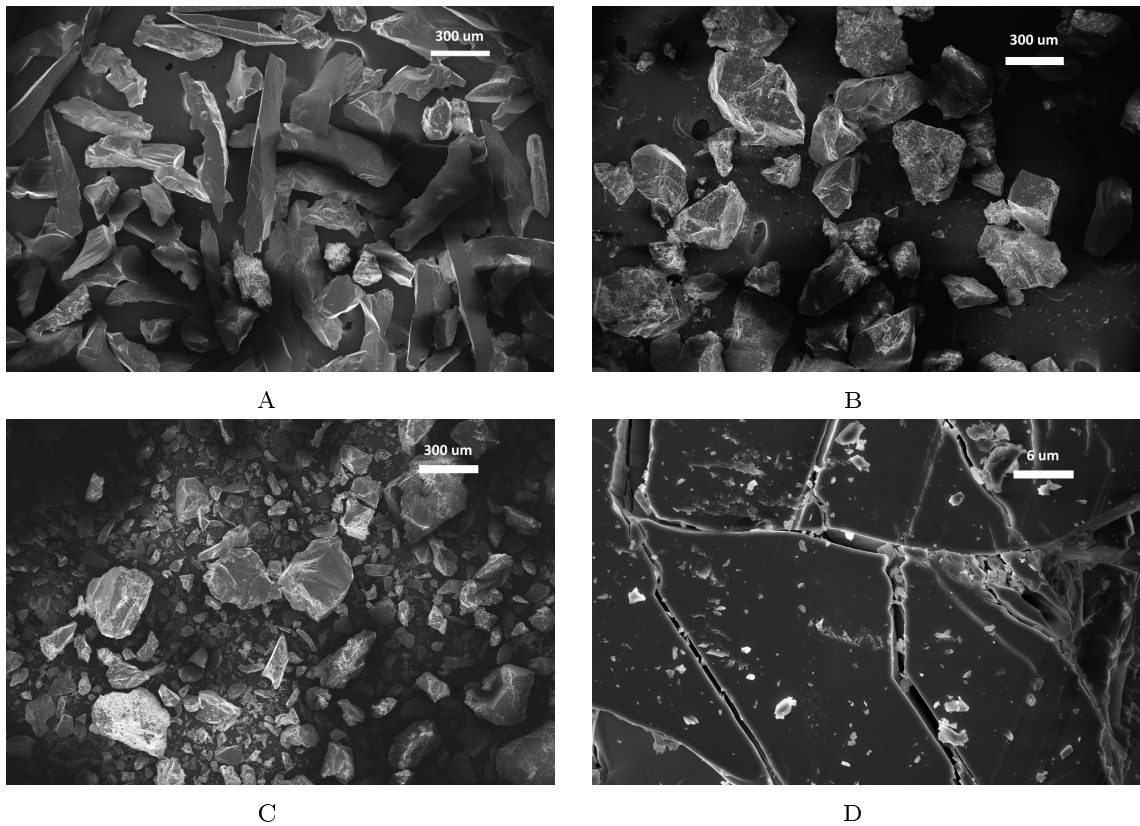


FIGURE 4.1: SEM images were taken of the Al_2O_3 powder to observe powder morphology before experiments and failure features post-experiment. Position A depicts the Al_2O_3 powder ($133 \pm 38 \mu\text{m}$) before compression. B depicts the Al_2O_3 powder ($133 \pm 38 \mu\text{m}$) after compression. Lastly, position C depicts the large Al_2O_3 powder ($414 \pm 57 \mu\text{m}$) after the experiment showing the resulting material size and shapes and D depicts surface features of the $414 \pm 57 \mu\text{m}$ Al_2O_3 powder.

4.1.2 Boron Carbide

For boron carbide, the particle geometry and structure of the powder was imaged using a JSM-IT300 SEM. Those samples were coated with palladium at 4 nm to improve the quality of the images. Shown in Figure 4.2A is an SEM image of the boron carbide fragments for sizes of $152 \pm 26 \mu\text{m}$. The particles have aspect ratios close to 1, with some appearing spherical and other appearing block-like in nature. There is some minor porosity in the fragments. Next, the fragment size range of $303 \pm 46 \mu\text{m}$ for boron carbide is shown in Figure 4.2B. Here, the larger fragments are also mostly near-spherical, but with fewer block like fragments shown than for the smaller sizes. The other images in Figure 4.2 are discussed later when we investigate material failure post experiment.

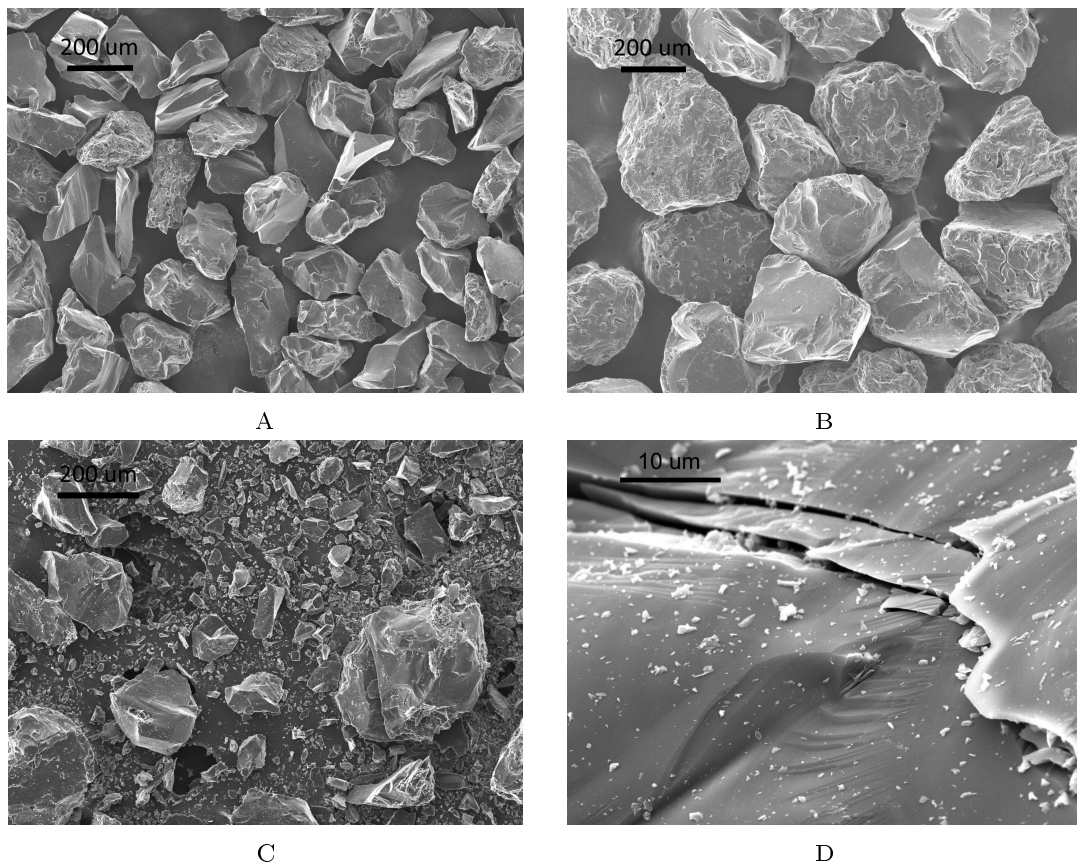


FIGURE 4.2: SEM images of B_4C were taken to observe the small and large particles, focusing on powder morphology before and after experiment. Position A depicts $152 \pm 26 \mu\text{m}$ B_4C powder before compression. Position B depict the $303 \pm 46 \mu\text{m}$ particle size showing the overall geometry before compression. Position C depict the postmortem $303 \pm 46 \mu\text{m}$ powder visualizing the overall fragment distribution and D depicts the surface features post experiment.

4.2 Particle Distribution

Four different size ranges were sieved, microscopically analyzed, and tested to observe the effects of mean particle diameter, $\bar{\phi}$ (μm), and shape, on hydro-static pressure, P (MPa), as a function of porosity, ϕ (%), for alumina and boron carbide. The alumina and boron carbide were initially sieved, and the particle size and shape were investigated, before compaction, using the PartAn 3D Dynamic Image Analyzer. The particle size distribution was analyzed on the basis of dynamic image analysis where the area equivalent diameter, Da (μm), was considered. This parameter is relevant when determining the distribution of the bulk sample used in the experiment and is the default principle used by the PartAn analyzer. To calculate this parameter the following equation is used:

$$Da = \left(\frac{4A}{\pi} \right)^{\frac{1}{2}} \quad (4.1)$$

where A (μm^2) is the area of the projected image. The same sieves and machine were used to analyze and test B_4C powder. The mean and standard deviation were documented for each particle size, and these results are summarized in Table 4.1 for alumina and Table 4.2 for boron carbide. Three samples of each material were tested and each specimen was sampled following principal sampling techniques for granular material outlined by Maynard [80]. To evaluate the relative variability of the powder, the span was calculated for each sample as was similarly used by Engeli et al. [83] where the equation takes into account the tenth (D_{10}), fiftieth (D_{50}), and ninetieth percentile (D_{90}):

$$\Delta = \frac{D_{90} - D_{10}}{D_{50}} \quad (4.2)$$

TABLE 4.1: Al₂O₃ Powder Characterization: the material span is Δ (unitless), the tenth percentile D_{10} (μm), the fiftieth percentile D_{50} (μm), and ninetieth percentile D_{90} (μm) of the distribution.

$\emptyset[\mu\text{m}]$	$D_{10}[\mu\text{m}]$	$D_{50}[\mu\text{m}]$	$D_{90}[\mu\text{m}]$	Δ
133 ± 38	97	160	240	0.894
201 ± 42	170	220	290	0.545
290 ± 52	250	310	390	0.452
414 ± 57	370	430	520	0.349

TABLE 4.2: B₄C Powder Characterization: the material span is Δ (unitless), the tenth percentile D_{10} (μm), the fiftieth percentile D_{50} (μm), and ninetieth percentile D_{90} (μm) of the distribution.

$\emptyset[\mu\text{m}]$	$D_{10}[\mu\text{m}]$	$D_{50}[\mu\text{m}]$	$D_{90}[\mu\text{m}]$	Δ
152 ± 26	130	170	210	0.471
171 ± 23	150	180	210	0.333
303 ± 46	280	320	370	0.281
461 ± 44	430	470	520	0.191

4.3 Experiment Configuration

4.3.1 Instrumented Die

Illustrated in Figure 4.3 is a schematic of the experimental apparatus used to conduct uniaxial confined compaction experiments on the granular material. The top and bottom punches are fabricated from O2 tool steel so that the high stiffness would transfer a maximum load through the specimen. The punches are used to press together the granular material. The top and bottom punches are designed around the accessibility of the Kistler electro-mechanical press machine used in this study. The crucible was made out of O2 tool steel with an inner diameter of 6 mm. The inner diameter was machined with a tight tolerance to seal in the granular material during compaction. The force was measured from the top and bottom axial load cell, depicted in Figure 4.3. To calculate the radial stress in the sample, the radial displacement deflected the radial load cell that outputs a force magnitude. The diameter of the radial rod was 3 mm. Attached

to the press was a LVDT (not shown in Figure 4.3) so that relative displacement could be recorded to track the initial and final volume of the specimen. The press machine outputted the applied load from the top, at a rate of 0.5 mm s^{-1} , placing the specimen under a quasi-static strain rate.

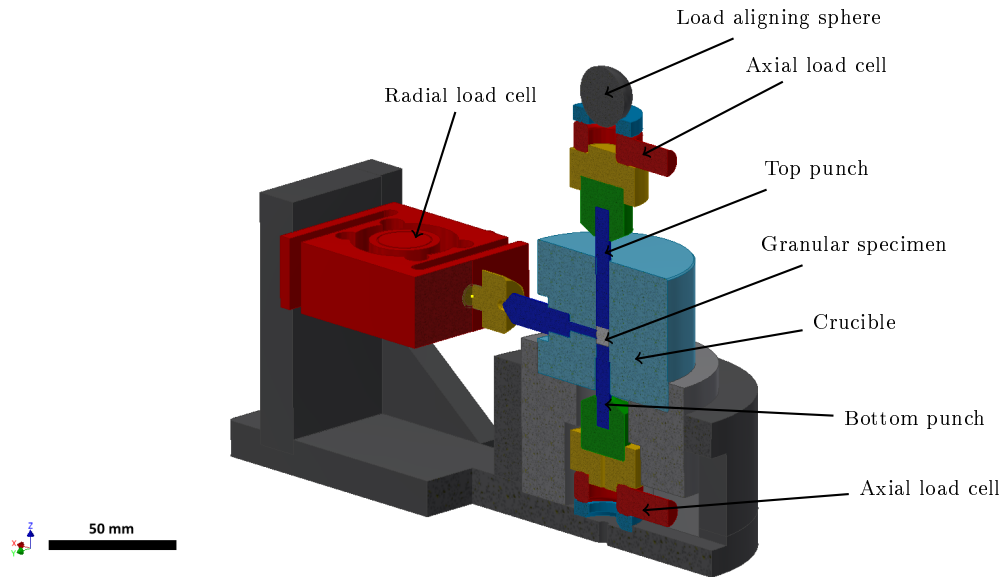


FIGURE 4.3: An isometric cross-section view is shown of the compaction apparatus used in compressing Al_2O_3 & B_4C powders to show the different components. The colour in the figure is to distinguish various components that constitute the apparatus.

In order to limit the wall frictional effects occurring during confined compaction, it is critical to maintain an aspect ratio of height to width of < 1 for the poured powder according to Fleck and Cocks [84]. The granular material was poured into the crucible void and a final aspect ratio of 0.59 was achieved during compaction. The obtained void volume was not the same for all samples because of the varying particle size and the uncertainty in initial volume was $209 \pm 13 \text{ mm}^3$ for Al_2O_3 , and $209 \pm 7 \text{ mm}^3$ for B_4C . The differences are as a result of the nature of small amounts of granular material and the geometrical constraints of the void size making it difficult to obtain identical amounts of material. Shown in Table 4.3 (for alumina) and Table 4.4 (for boron carbide) are the sample specifications for each test presented here, including mean diameter with standard deviation, initial mass, initial volume, initial density, final density, initial porosity, and final porosity after the experiment.

TABLE 4.3: Alumina experiment parameters: mean diameter \bar{O} (μm), mass m (g), initial void volume V_o (mm^3), initial density ρ_i (kg m^{-3}), final density ρ_f (kg m^{-3}), initial porosity ϕ_i (%), and final porosity ϕ_f (%).

\bar{O} [μm]	m [g]	V_o [mm^3]	ρ_i [kg m^{-3}]	ρ_f [kg m^{-3}]	ϕ_i	ϕ_f
133 \pm 38	0.3265	198	1647	3199	58.7%	19.8%
133 \pm 38	0.3249	183	1779	3237	55.4%	18.8%
133 \pm 38	0.3306	188	1758	3439	55.9%	13.7%
201 \pm 42	0.3174	188	1686	3273	57.7%	17.9%
201 \pm 42	0.3327	195	1705	3362	57.2%	15.7%
201 \pm 42	0.3311	204	1626	3581	59.2%	10.2%
290 \pm 52	0.3651	200	1821	3371	54.3%	15.4%
290 \pm 52	0.3587	198	1807	3253	54.7%	18.4%
290 \pm 52	0.3495	176	1991	3552	50.1%	10.9%
414 \pm 57	0.3202	168	1907	3630	52.2%	9.0%
414 \pm 57	0.3062	161	1900	3634	52.3%	8.9%
414 \pm 57	0.3220	164	1963	3722	50.8%	6.7%

TABLE 4.4: Boron carbide experiment parameters: mean diameter \bar{O} (μm), mass m (g), initial void volume V_o (mm^3), initial density ρ (kg m^{-3}), final density ρ (kg m^{-3}), initial porosity ϕ_i (%), and final porosity ϕ_f (%).

\bar{O} [μm]	m [g]	V_o [mm^3]	ρ_i [kg m^{-3}]	ρ_f [kg m^{-3}]	ϕ_i	ϕ_f
152 \pm 26	0.2728	201	1359	2228	46.1%	11.6%
152 \pm 26	0.2843	221	1287	2135	48.9%	15.3%
152 \pm 26	0.2650	197	1349	2232	46.5%	11.4%
171 \pm 23	0.2731	200	1364	2132	45.9%	15.4%
171 \pm 23	0.2847	202	1410	2189	44.0%	13.1%
171 \pm 23	0.2825	200	1409	2099	44.1%	16.7%
303 \pm 46	0.2321	207	1121	1777	55.5%	29.5%
303 \pm 46	0.2666	191	1393	2148	44.7%	14.8%
303 \pm 46	0.2725	196	1393	2118	44.7%	15.9%
461 \pm 44	0.1680	201	836	2358	66.8%	6.4%

To perform the testing, the material was carefully poured into the void and the top punch

was rested up on the sample. The top hydraulic arm was then lowered to compress the granular material to a maximum force of 50 kN. The LVDT was secured to the top arm, so that the relative compaction depth could be measured.

4.3.2 Instrumented Die Theory

To better understand the response of the granular material during quasi-static triaxial compression, the relationship between the hydro-static pressure and porosity was investigated by tracking the axial stress, radial stress, and relative density in the confined crucible. First, the reduction in porosity of our test samples was tracked through measurements of initial mass m (kg), initial packing porosity ϕ_i (%), and the cross-head displacement δ (mm) of the top punch that is used to compress the samples. The mass of the initial granular sample was measured by a digital scale with the precision of 0.0001 g, and values for each experiment are listed in Table 4.1 (for alumina) and Table 4.2 (for boron carbide). The sample size was volume controlled with a limiting void volume of 209 mm^3 . Throughout the compression experiment, the change in displacement, δ (mm), is related to change in volume, ΔV (m^3). Refer to (3.4) where the relation has been defined before in Section 3.3.2. The density of the sample was tracked using (3.5) and further calculated in terms of porosity, outlined in (3.6). The relative density was normalized by the bulk solid density, ρ_s (kg m^{-3}). For Al_2O_3 and B_4C , the bulk density is taken as 3987 kg m^{-3} and 2520 kg m^{-3} , respectively. These equations have also been defined before in Section 3.3.2.

Next, the hydro-static pressure is calculated by measuring the difference in axial stress, σ_z (MPa), from the top and bottom load cell and the radial stress, σ_r (MPa), from the perpendicular mounted load cell. Refer to the schematic in Figure 4.3 for orientation. The equation for hydro-static stress, P (MPa), is written in (3.3.2), shown in Section 3.3.2. To calculate the axial stress, σ_z , we divide the difference in axial force experienced by the sample, F_z (N), and the cross-sectional area of the void A_0 (m^2), assuming that the area does not change during compression. As mentioned before, F_z was computed by subtracting the axial forces outputted by the top and bottom load cell, respectively, so that we can account for the wall friction effects introduced during compaction.

To determine the radial stress, the radial force was transferred from the material by a thin shaft that was located at the centre of the uncompressed specimen (see Figure 4.3). As compaction commenced, the thin shaft was pressed against the load cell mounted perpendicular to the apparatus, which recorded the force. Using (4.3), the radial stress was calculated:

$$\sigma_r = \frac{F_r}{A_r} \quad (4.3)$$

where F_r is the radial force (N) and A_r is the cross-sectional area, (m^2). By machining the moving pieces with high transitional tolerances, the contact friction between the shaft and hole can be neglected.

Next, the bulk modulus was investigated, focusing on the particle size effects. The bulk modulus describes the compressibility of the material and relates the change in volume of the material, ΔV (m^3), as a function of change in pressure, ΔP (MPa). The bulk modulus relationship is derived in (3.3.2). Likewise, this material constant took into account the elastic and plastic behaviour during compaction. This parameter evolves during loading and is an indicator of deformation in the granular sample. (Refer to Section 3.3.2 for derivation).

Lastly, we look at frictional effects by monitoring the transmitted stress ratio, T . To do this, we calculate the ratio of transmitted stress, σ_t (MPa), over the applied stress, σ_a (MPa). The applied stress is read from the top axial load washer while the transmitted stress is recorded by the bottom axial load washer. The difference in applied and transmitted stresses provides insight on how much energy is lost to friction in the crucible apparatus. This ratio has been previously defined in (3.3.2) in Section 3.3.2.

To account for the uncertainty in the experiment, we conducted a systematic propagation of error, taking into account the uncertainty of the sensors and measured geometries. This helps in understanding the accuracy of the results. Based on the guide outlined by Berendsen [90], Table 4.5 summarizes extreme cases of the relative uncertainty of critical material parameters that were calculated. The rules for calculating uncertainty have been derived and computed extensively in literature and will not be explicitly shown. Refer to [90] and Appendix B for full derivations and summery respectively.

TABLE 4.5: Systematic uncertainty: propagation of error.

Constants	Al ₂ O ₃ 133 ± 38 μm	Al ₂ O ₃ 414 ± 57 μm	B ₄ C 152 ± 26 μm	B ₄ C 303 ± 46 μm
V_o	0.7%	0.7%	0.6%	0.5%
ϕ	2.5%	3.1%	1.7%	1.4%
P	1.2%	1.0%	1.2%	1.5%
B_{ep}	1.9%	1.9%	1.8%	1.5%
T	1.9%	1.9%	2.0%	2.9%

4.4 Compaction Results and Discussion

4.4.1 Hydro-static Response

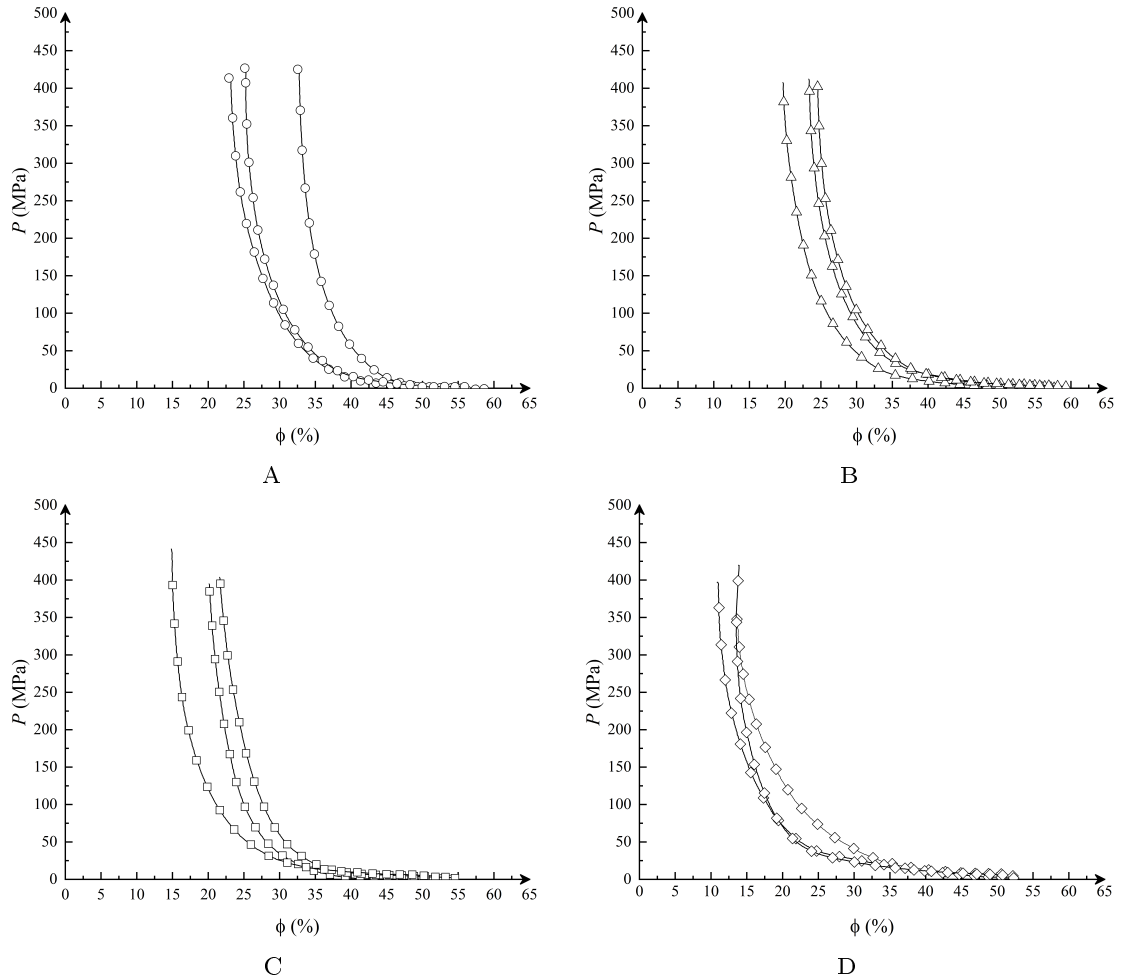


FIGURE 4.4: In the figure we see the hydro-static pressure response of granular Al_2O_3 . In A, the hydro-static pressure response as a function of porosity was captured for the range of particles $133 \pm 38 \mu\text{m}$. In B, the hydro-static pressure response as a function of porosity was captured for the particle size range $201 \pm 42 \mu\text{m}$. In position C the hydro-static pressure response was captured for the particle size range $290 \pm 52 \mu\text{m}$. In position D, the hydro-static pressure response was captured for particle size range $414 \pm 57 \mu\text{m}$.

First, the hydro-static pressure response as a function of porosity and particle size in alumina was investigated Figure 4.4. Figure 4.4A is for the smallest particle size ($133 \pm 38 \mu\text{m}$) and Figure 4.4D is for the biggest particle size ($414 \pm 57 \mu\text{m}$). As the particle size is decreased, the curves shift to the right, with values of porosity for an average hydro-static pressure of 375 MPa reported of $27 \pm 4 \%$ for $133 \pm 38 \mu\text{m}$, $22 \pm 2 \%$ for 201 ± 42

μm , $20 \pm 3 \%$ for $290 \pm 52 \mu\text{m}$, and $12 \pm 1 \%$ for $414 \pm 57 \mu\text{m}$. We note the variabilities for a given particle size at this hydro-static pressure, and that not all tests begin at the same initial porosities ϕ_i .

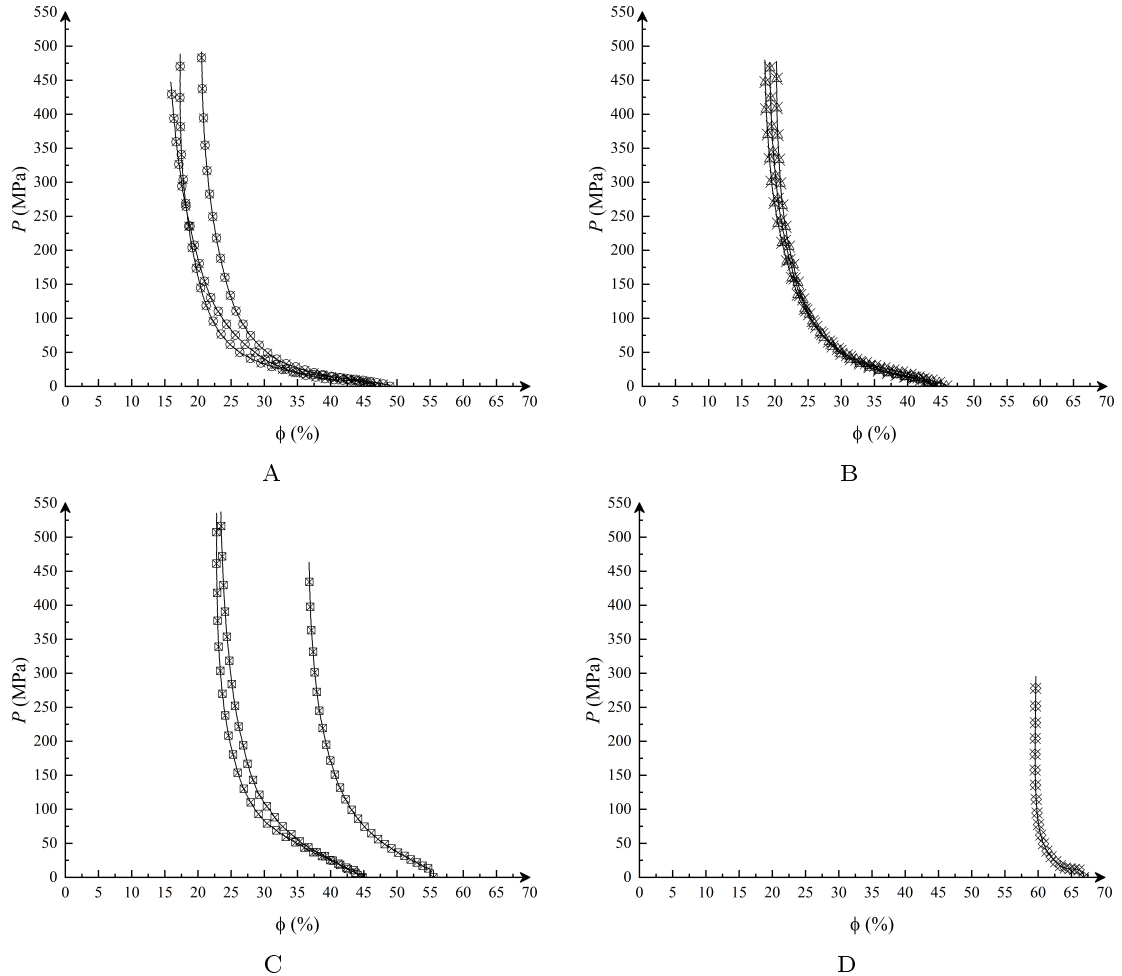


FIGURE 4.5: In the figure we see the hydro-static pressure response of granular B_4C . In A, the hydro-static pressure response as a function of porosity was captured for the range of particles: $152 \pm 26 \mu\text{m}$. In B, the hydro-static pressure response as a function of porosity was captured for the particle size range: $171 \pm 23 \mu\text{m}$. In position C the hydro-static pressure response was captured for the particle size range: $303 \pm 46 \mu\text{m}$. In position D, the hydro-static pressure response was captured for particle size range: $461 \pm 44 \mu\text{m}$.

Next, shown in Figure 4.5 are the hydro-static pressure-porosity curves as a function of particle size for granular B_4C . In this figure, the smaller particles ($152 \pm 26 \mu\text{m}$) are shown in Figure 4.5A, and the larger particle ($461 \pm 44 \mu\text{m}$) are shown in Figure 4.5D. From Figure 4.5, we observe that the curves shift to the right for increasing particle size. For the same average hydro-static pressure of 375 MPa , we find that the resulting porosity is $18 \pm 2 \%$ for particle size $152 \pm 26 \mu\text{m}$, $20 \pm 1 \%$ for $171 \pm 23 \mu\text{m}$, and 25 ± 2

% for $303 \pm 46 \mu\text{m}$. Since there is only one test for $461 \pm 44 \mu\text{m}$ (Figure 4.5D), not much significance is put on it. However, this data is still plotted with the other particle size data-set for completeness. It is important to note that lower porosities were achieved for the Al_2O_3 powder compared to the B_4C even though the applied load was the same.

4.4.2 Bulk Modulus

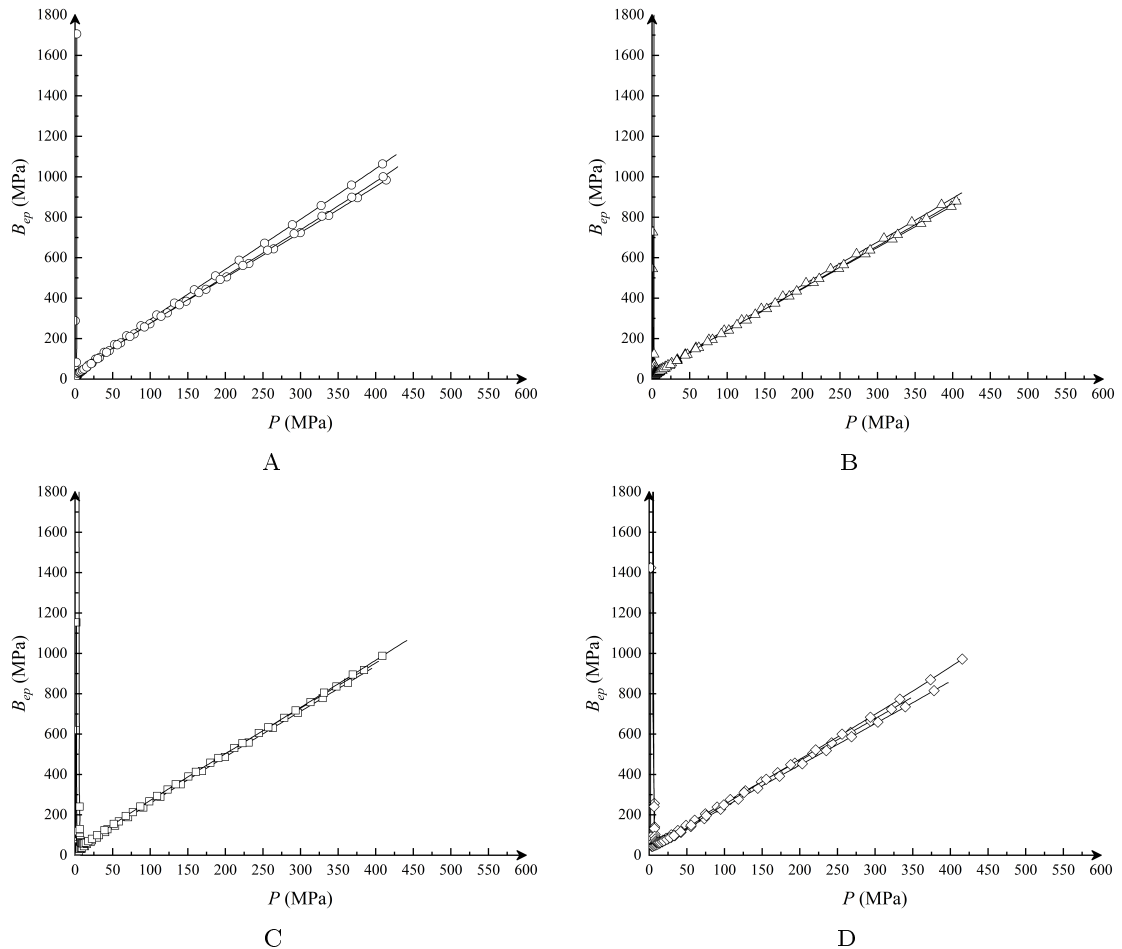


FIGURE 4.6: In the figure we see the bulk modulus response of the Al_2O_3 powder as a function of hydro-static pressure. In A, the bulk modulus response as a function of hydro-static pressure was captured for the range of particles: $133 \pm 38 \mu\text{m}$. In B, the bulk modulus response as a function of hydro-static pressure was captured for the particle size range: $201 \pm 42 \mu\text{m}$. In position C the bulk modulus response as a function of hydro-static pressure was captured for the particle size range: $290 \pm 52 \mu\text{m}$. In position D, the bulk modulus response as a function of hydro-static pressure was captured for particle size range: $414 \pm 57 \mu\text{m}$.

Next, we discuss the compaction effects of the materials described by the bulk modulus in Figure 4.6 and Figure 4.7. Referring to Figure 4.6, the behaviour of Al_2O_3 particles

do not follow a distinct trend in that the bulk modulus is not greater or lesser depending on the particle size. The average bulk modulus at the chosen hydro-static pressure of 400 MPa is 988 MPa for $133 \pm 38 \mu\text{m}$ depicted in Figure 4.6A, 873 MPa for $201 \pm 42 \mu\text{m}$ in Figure 4.6B, 959 MPa for $290 \pm 52 \mu\text{m}$ depicted in Figure 4.6C. For the largest size ($414 \pm 57 \mu\text{m}$) illustrated in Figure 4.6D, the average maximum hydro-static pressure reached was 347 MPa and the corresponding average bulk modulus was 869 MPa.

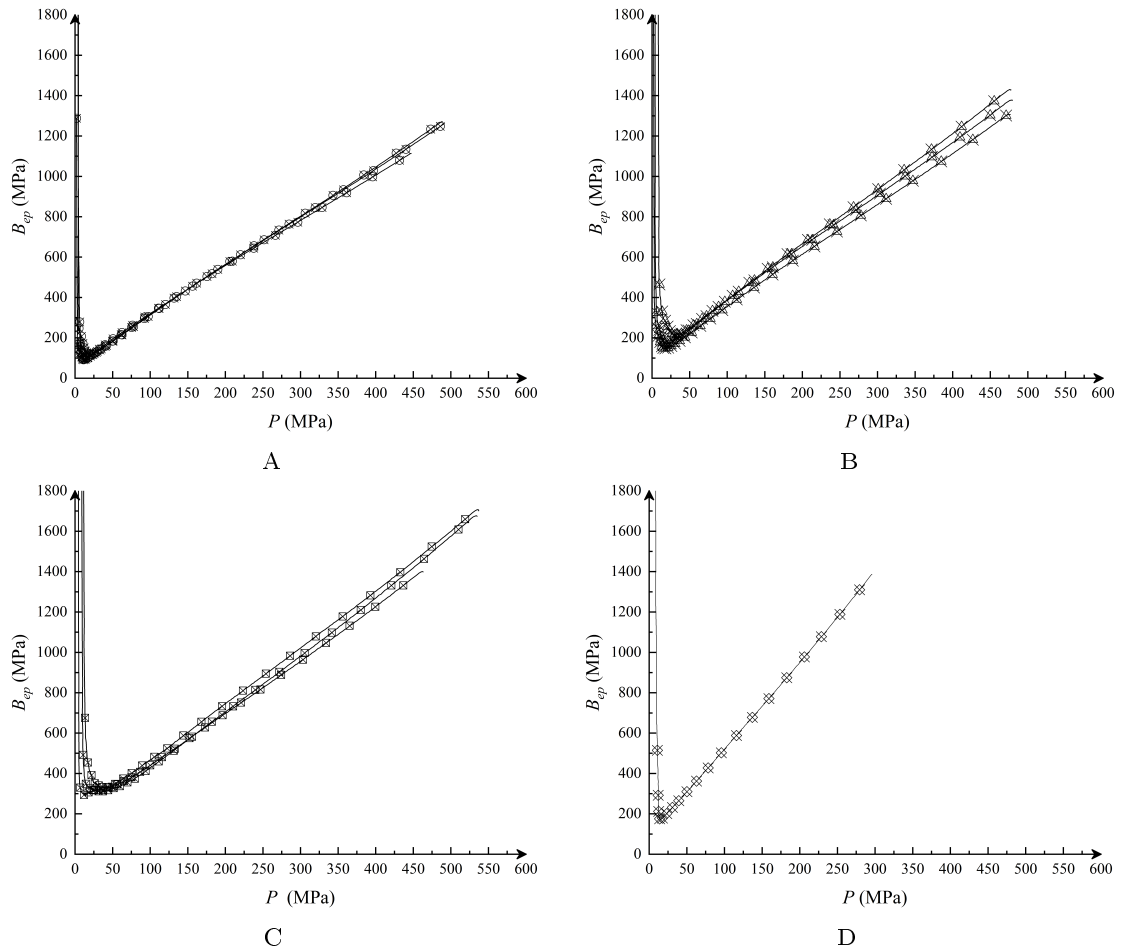


FIGURE 4.7: In the figure we see the bulk modulus response of granular B_4C . In A, the bulk modulus response as a function of hydro-static pressure was captured for the range of particles: $152 \pm 26 \mu\text{m}$. In B, the bulk modulus response as a function of hydro-static pressure was captured for the particle size range: $171 \pm 23 \mu\text{m}$. In position C the bulk modulus response as a function of hydro-static pressure was captured for the particle size range: $303 \pm 46 \mu\text{m}$. In position D, the bulk modulus response as a function of hydro-static pressure was captured for particle size range: $461 \pm 44 \mu\text{m}$.

Conversely, clear trends exist when looking at the bulking effects as a function of hydro-static pressure for the B_4C in Figure 4.7. Namely, the bulk appears to increase with increasing particle size, meaning the material behaviour becomes stiffer for increasing particle size. Furthermore, we can note that higher overall bulk modulus was achieved

for the B_4C powder in comparison to the Al_2O_3 powder for the same applied load. At a hydro-static pressure of 400 MPa a bulk modulus of 1031 MPa for $152 \pm 26 \mu m$ depicted in Figure 4.7A, 1164 MPa for $171 \pm 23 \mu m$ shown in Figure 4.7B, and 1270 MPa for $303 \pm 46 \mu m$ shown in Figure 4.7C. As mentioned before, there is only one test for $461 \pm 44 \mu m$ where the bulk modulus of 1387 MPa was reached with a hydro-static pressure of 295 MPa, and so the data-set is only plotted for completeness and illustrated in Figure 4.7D.

4.4.3 Friction

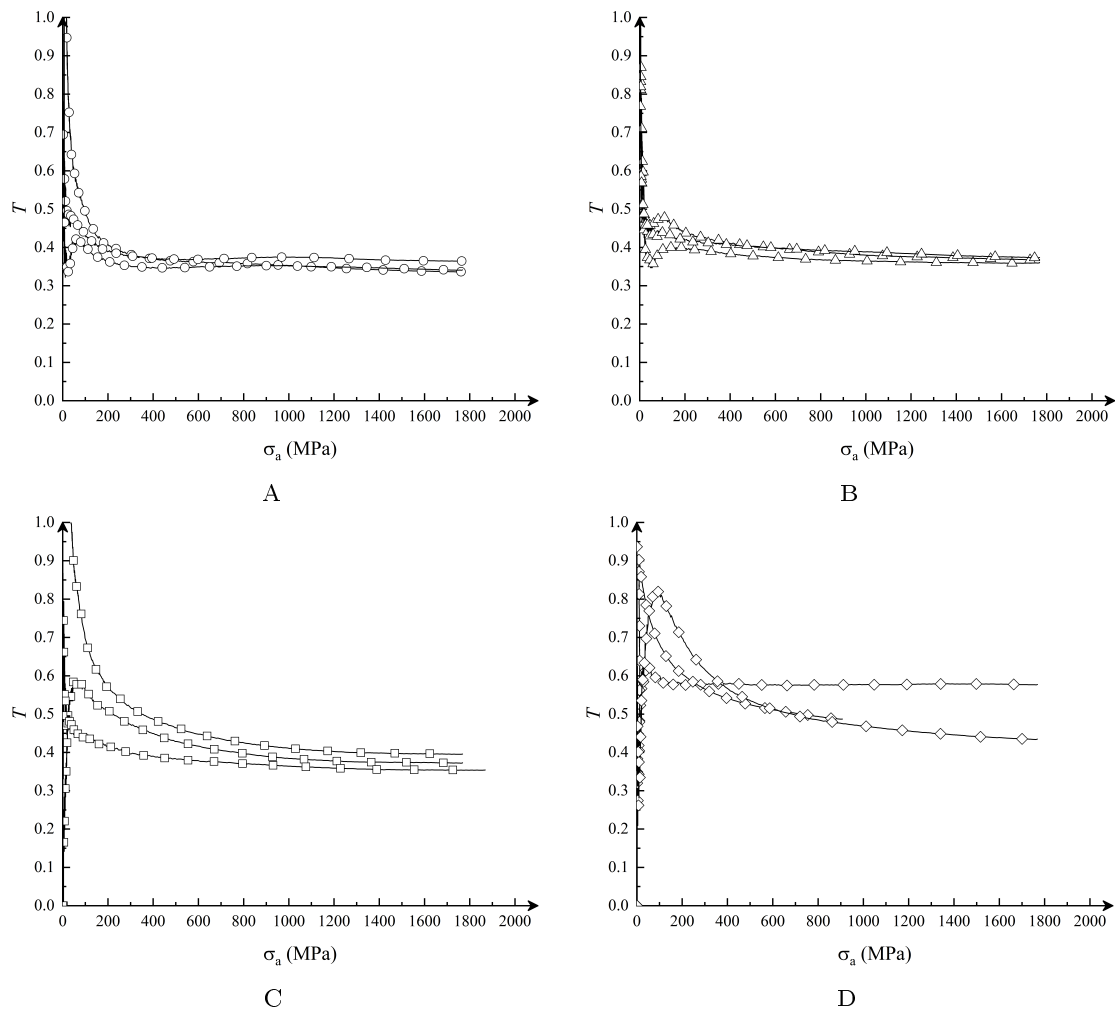


FIGURE 4.8: In the figure we see the transmission ratio of the Al_2O_3 powder as a function of applied stress. In position A, the transmission ratio response as a function of the applied stress was captured for the range of particles: $133 \pm 38 \mu m$. In position B, the transmission ratio as a function of applied stress was captured for the particle size range: $201 \pm 42 \mu m$. In position C the transmission ratio was captured for the particle size range: $290 \pm 52 \mu m$. In position D, the transmission ratio was captured for particle size range: $414 \pm 57 \mu m$.

The transmission ratio relates the force transferred from the compression machine through the material. In Figure 4.8, the transmission ratio for the Al_2O_3 powder is plotted as a function of applied stress. With the applied load below 600 MPa, the trend observed is when increasing the particle size, the transmission ratio increases. This is believed to be a consequence of the larger particles having a smaller contact area that result in less friction, and consequently, for more stress being transmitted. For higher applied stress (1600 MPa) the average transmission ratio for each particle size converges to: 0.35 for $133 \pm 38 \mu\text{m}$, 0.37 for $201 \pm 42 \mu\text{m}$, 0.38 for $290 \pm 52 \mu\text{m}$, and 0.50 for $414 \pm 57 \mu\text{m}$.

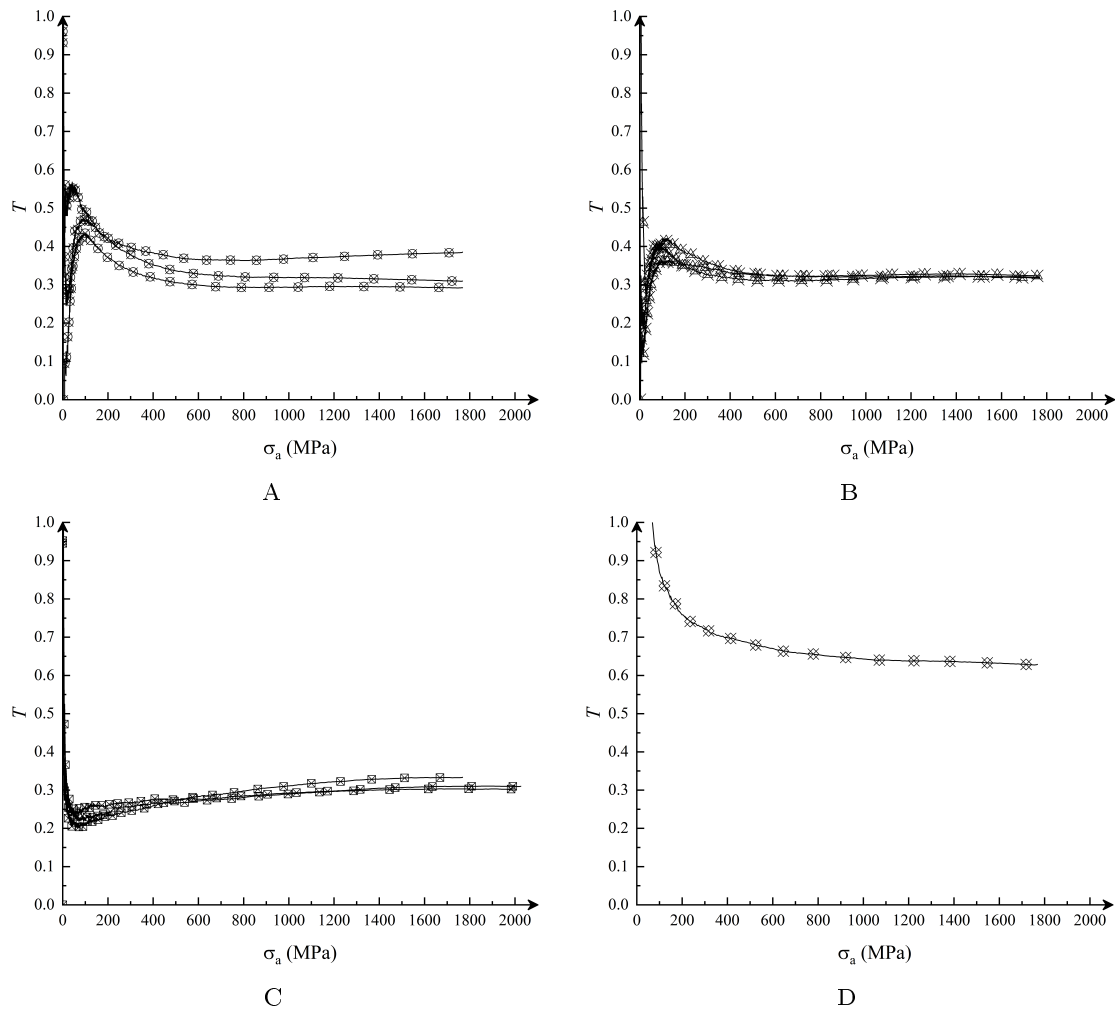


FIGURE 4.9: In the figure we see the transmission ratio of the B_4C powder as a function of the applied stress. In position A, the transmission ratio response as a function of the applied stress was captured for the range of particles: $152 \pm 26 \mu\text{m}$. In position B, the transmission ratio as a function of applied stress was captured for the particle size range: $171 \pm 23 \mu\text{m}$. In position C the transmission ratio was captured for the particle size range: $303 \pm 46 \mu\text{m}$. In position D, the transmission ratio was captured for particle size range: $461 \pm 44 \mu\text{m}$.

Unlike the Al_2O_3 , there appears to be no clear trend in the B_4C transmission ratio behaviour, depicted in Figure 4.9. Taken at 1600 MPa, the average ratio for $152 \pm 26 \mu\text{m}$ is 0.33, for $171 \pm 23 \mu\text{m}$ is 0.32, for $303 \pm 46 \mu\text{m}$ is 0.31, and for $461 \pm 44 \mu\text{m}$ particle size, there was only one test and so we only plot for completeness.

4.4.3.1 Failure

With the mechanical properties outlined, SEM images in Figure 4.1 and Figure 4.2 were investigated observing failure process. Recalling that the fragment size, shape, and internal feature morphologies were already presented for Figure 4.1A and discussed in the Section 4.1, we investigate failure and fragmentation features in alumina in Figure 4.1B. The particles no longer appear to have elongated structures and have been reduced to shapes having a aspect ration closer to 1. Shown in Figure 4.1C is a collection of alumina fragments post-experiment for an initial particle size of $414 \pm 57 \mu\text{m}$. From the image, notice that most of the fragments now appear with fewer smaller fragments. In the image, there are few large particles between $150 \mu\text{m}$ and $366 \mu\text{m}$ in size, with many more smaller fragments that are between $40 \mu\text{m}$ and $88 \mu\text{m}$ in size. Similar observations were made by [42], where a great amount of fine-grained fragments were recovered post compression. Lastly, shown in Figure 4.1D is an higher magnification SEM image of an alumina fragment surface for the test with initial particle sizes $414 \pm 57 \mu\text{m}$. The image depicts two sets of near parallel fractures emerging from a central crack that spans from right to left in the image. These fractures are interpreted to be a consequence of bending resulting from the elongated initial particle shape for this material

The approach was similar when investigating the failure and fragmentation features in boron carbide in Figure 4.2C and Figure 4.2D. Recall, the SEM image in Figure 4.2A and Figure 4.2B depicts typical fragments for a particle size of $152 \pm 26 \mu\text{m}$ and $303 \pm 46 \mu\text{m}$, respectively, demonstrating some block like fragments for sizes of $152 \pm 26 \mu\text{m}$ but mostly near-spherical particles with aspect ratios close to 1 for sizes of $303 \pm 46 \mu\text{m}$ and $461 \pm 44 \mu\text{m}$. Shown in Figure 4.2C is a collection of fragments taken after an experiment for the $303 \pm 46 \mu\text{m}$ particle size. In the image, we see that there are very few larger block like fragments that are between $175 \mu\text{m}$ and $336 \mu\text{m}$ in size. These larger fragments have some fractures in them and many smaller comminuted fragments in their surface. There are also many smaller fragments between $30 \mu\text{m}$ and $82 \mu\text{m}$ in size that

are plate-like and angular. Lastly, an SEM image of a fragment surface for a particle that was $303 \pm 46 \mu\text{m}$ in size is shown in Figure 4.2D. The fragment surface further highlights some shallow surface fracturing and the presence of many smaller comminuted fragments that are $0.1 \mu\text{m}$ to $2 \mu\text{m}$ in size.

The densification of the advanced ceramics was additionally investigated with an empirical approach. Supplementary material on the empirical curve fitting located in Appendix E, was conducted to generally describe the trends observed in the compaction curves illustrated in Figure 4.4. Working from research conducted by Lee and Kim [70], the function form of (E.1) was used where equation constants (A , B , and C) were computed. For the Al_2O_3 powder, constant A increased with increasing particle size while the constants B and C approached a plateau with increasing particle size. On the contrary, the B_4C powder were unique in that constant A increases with particle size and reaching a maximum point where it decreases. For constant B , the value increases with increasing particle size and constant C decreases with increasing particle size. Future studies will be conducted to relay the information incorporating this behaviour in the Drucker-Prager empirical model.

4.4.4 Distributions

To track the evolution particle size distributions as a consequence of compaction, measurements were taken of the materials before and after compression. To do this, we show the cumulative distribution of the particle sizes taken as the maximum spanning length provided by the Morphologi G3 microscope and the Microtrac PartAn 3-D microscope. The cumulative distribution is defined as:

$$G(x) = \int_0^x g(\bar{x}) d\bar{x} \quad (4.4)$$

where $g(\bar{x})$ is the probability distribution of the particle sizes. The particle size data set in each direction is a discrete set of n particles with sizes of $l_i (i = 1 \dots n)$. Ordering this data for increasing particle size, and assigning a probability of $1/n$ to each particle, the normalized empirical cumulative distribution function can be computed as the sum of these probabilities:

$$G_e(l) = \frac{1}{n} \sum_{i=1}^n I(l_i \leq l) \quad (4.5)$$

where the indicator function I has a value of 1 if $l_i \leq l$ and 0 otherwise. Shown in Figure 4.12 are the cumulative distributions of particle sizes before and after for the alumina experiments. The average of the medians after compression (50th percentiles) are: $7.0 \pm 0.2 \mu\text{m}$ for the $133 \pm 38 \mu\text{m}$ particles, $6.0 \pm 0.1 \mu\text{m}$ for the $201 \pm 42 \mu\text{m}$ particles, $5.0 \pm 0.1 \mu\text{m}$ for the $290 \pm 52 \mu\text{m}$ particles, and $6.0 \pm 0.1 \mu\text{m}$ for the $414 \pm 57 \mu\text{m}$ particles. Similarly, shown in Figure 4.13 are the cumulative distributions of particle sizes before and after for the boron carbide experiments. The average of the medians after compression (50th percentiles) are: $5.0 \pm 0.1 \mu\text{m}$ for the $152 \pm 26 \mu\text{m}$ particles, $5.0 \pm 0.4 \mu\text{m}$ for the $171 \pm 23 \mu\text{m}$ particles, $5.0 \pm 0.3 \mu\text{m}$ for the $303 \pm 46 \mu\text{m}$ particles, and $5.0 \pm 0 \mu\text{m}$ standard deviation for the $461 \pm 44 \mu\text{m}$ particles. Generally, trends in the change in sizes or final sizes are challenging to unravel given the different initial starting sizes and porosities, and final hydro-static pressures experienced by the compacted materials.

4.5 Discussion and Summary

In this chapter, we explored the mechanical response of alumina and boron carbide powder, in hopes of better understanding the effects of particle size and shape on the uniaxial compaction response under quasi-static strain rates. In the literature, there exists limited studies on the behaviour of granular ceramics [43, 45, 62, 109–111], with many authors noting as much [46, 112]. Few studies have accounted for particle size effects [113, 114]. To address the gap in understanding granular ceramic behaviour, this study focused on the mechanical response (e.g., hydro-static pressure, bulk modulus, transmission ratio) and failure of granular alumina and boron carbide materials of varying particle sizes. The particle size ranges for alumina powder were $95 \mu\text{m}$ to $471 \mu\text{m}$, and for boron carbide were $126 \mu\text{m}$ to $505 \mu\text{m}$. The particle size ranges were chosen based on resulting fragmentation sizes derived during impact into boron carbide by Krell and Strassburger [8], as well to compare with other studies in the literature of comparable sizes (e.g., [43, 100]). Also note that the alumina particles were mostly elongated in shape while the boron carbide fragments has aspect ratios closer to 1. The selection of an elongated shape for particles is also motivated by the impact fragmentation work by Krell and Strassburger [8] where shard-like fragments were observed as a consequence of ballistic testing, while the choice of uniform shapes is to conform with geometries commonly selected in the literature [44, 115]. To study the uniaxial confined response of the materials, an apparatus

for confined quasi-static compression was designed and adapted from literature [63–65]. Other studies in the literature have used different experimental approaches, including the thick-walled cylinder set-ups for confined uniaxial compaction under quasi-static and dynamic loading [42], plate impact testing [30], and thick-walled implosion compaction experiments [116]. In thick-walled cylinder implosion experiments performed on granular alumina by Nesterenko et al. [116] and silicon carbide by Shih et al. [113], both noted the importance of shear localization and comminution in the responses of granular ceramics. We also note the importance of comminution in our quasi-static confined compaction experiments, as evidenced by Figures 4.1 and 4.2.

To better understand the effect of particle size on the mechanical response, investigations were made on the bulk modulus and transmission ratio as a function of pressure where the unique trends are depicted in Figures 4.10A and 4.10B respectively. For bulk modulus, the Al_2O_3 did not exhibit any clear trends in behaviour as a function of particle size, while the boron carbide demonstrated a greater sensitivity of the bulk modulus on hydrostatic pressure (steeper slope) and an overall greater bulk modulus as a function of increasing particle size (1031 ± 72 MPa for 152 ± 26 μm , 1164 ± 50 MPa for 171 ± 23 μm , and 1270 ± 136 MPa for 303 ± 46 μm). These values align with those reported in literature by Dyachkov et al. [117]. For the transmission ratio, which probed the effects of friction, clear trends were observed in the alumina material (0.35 ± 0.01 for 133 ± 38 μm , 0.370 ± 0.006 for 201 ± 42 μm , 0.38 ± 0.01 for 290 ± 52 μm , and 0.50 ± 0.06 for 414 ± 57 μm) where similarities have been observed before [118, 119]. Specifically, these values align with those reported by Dimilia and Reed [119] of ~ 0.4 at 100 MPa. Boron carbide, on the other hand, did not exhibit clear trends which has not been noted previously. The global behaviour of the material response was depicted by choosing the tests that resulted with the largest deviation with respect to a given particle size. Generally, the high variability across all mechanical property measurements is likely a consequence of the variable spatial distribution of particle size and shape distributions among samples as a result of sample preparation and setup.

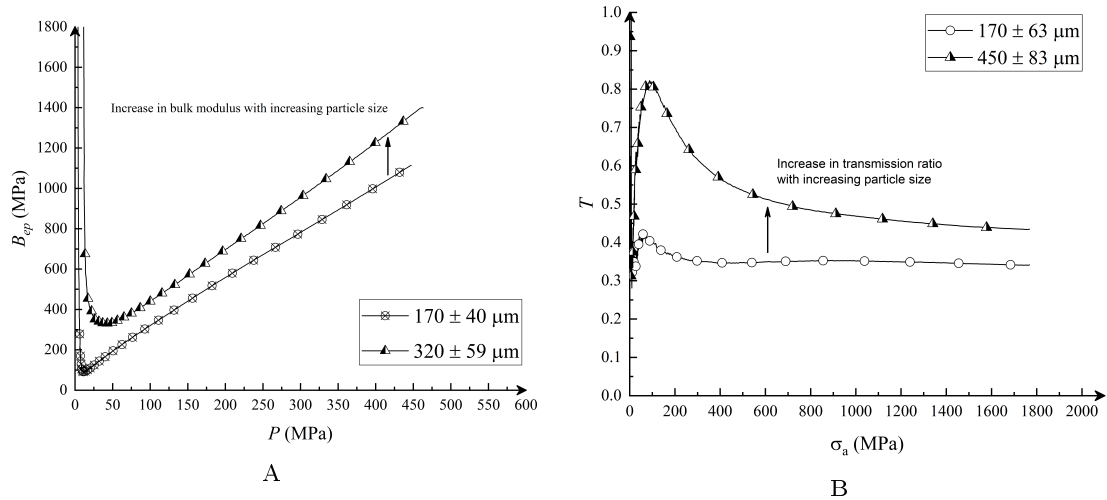


FIGURE 4.10: In A we see the overall trend of the bulk modulus for granular B_4C , depicting the sensitivity of particle size on bulk modulus as a function of hydro-static pressure. Illustrated in the B is the overall trend of the transmission ratio of granular Al_2O_3 . As the particle size increases, the transmission ratio increases. To show the global behaviour of the material response, the tests with the largest deviation with respect to a given particle size were chosen.

In addition to probing the effects of particle size and bulk modulus and transmission ratio, we also explored the effects of particle size on the hydro-static response as a function of porosity. This relation is important when developing yield surfaces for brittle failure [114, 120, 121]. Two distinct trends were observed from our experiments. In the alumina samples with elongated particle shape, increasing the particle size resulted in the curve shifted to the left which is depicted in Figure 4.11A. At 375 MPa, the porosity was observed to decrease for increasing particle size ($27 \pm 4 \%$ porosity at $133 \pm 38 \mu\text{m}$, to $12 \pm 1 \%$ porosity at particle size $414 \pm 57 \mu\text{m}$). Conversely for boron carbide, as the particle size increased from $152 \pm 26 \mu\text{m}$ to $461 \pm 44 \mu\text{m}$, less porosity was crushed out ($18 \pm 2 \%$ for particle size $152 \pm 26 \mu\text{m}$, to $25 \pm 2 \%$ for particle size $303 \pm 46 \mu\text{m}$). The trend was illustrated in Figure 4.11B. Additionally, the spread of the hydro-static curves for repeated experiments for B_4C was smaller in comparison to Al_2O_3 . Comparing the results from our study, Carneim and Messing [115] conducted similar confined compaction tests of alumina powder for the purpose of investigating the effects of compaction stress on granular rearrangement. They noted that when increasing the sample diameter, the required compaction stress decreases as a result of a decrease in the die wall friction. Notably, for a compaction stress of ~ 100 MPa and alumina powder size of $75 \mu\text{m}$ to $150 \mu\text{m}$ with 2% binder, Carneim and Messing [115] reported a porosity of 43%. In our experiments involving $170 \mu\text{m}$ powders, we were able to achieve 41% porosity at the

same hydro-static pressure. Taken together, the results demonstrate the sensitivity of particle size on mechanical responses, and this highlights the importance incorporating these considerations into failure models. This is discussed next.

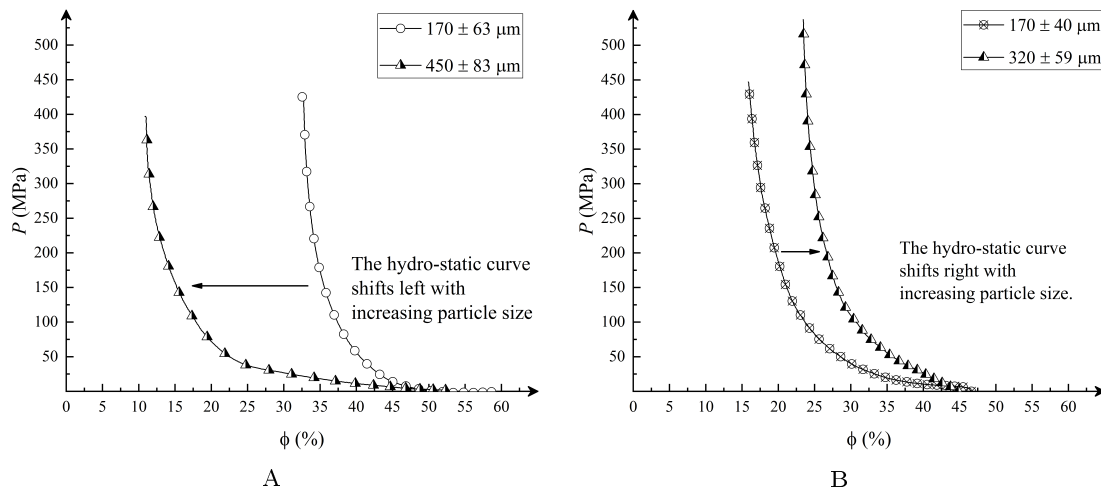


FIGURE 4.11: In the figure are illustrated the overall trends seen in the granular Al_2O_3 , position A, and granular B_4C , position B, depicting the hydro-static pressure response as a function of porosity for increasing particle sizes. To show the global response of the material, individual tests with respect to a given particle size were chosen.

In all mechanical response measurements, note the variability in results at a given average particle size (Figures 4.4 to 4.9). This variability is likely a consequence of the variable spatial distribution of particle size and shape distributions among samples as a result sample preparation and setup. The slight deviation is a result of the particle size and shape distribution. Table 4.6 summarizes the standard deviation obtained for the three samples tested at a given average particle size.

TABLE 4.6: Standard deviation in material properties at each particle size tested for granular Al_2O_3 and B_4C .

	Al_2O_3 average particle size				B_4C average particle size			
	133 μm	201 μm	290 μm	414 μm	152 μm	171 μm	303 μm	461 μm
Porosity (at 375 MPa)	16%	10%	15%	12%	11%	4%	24%	-
Bulk modulus (at 400 MPa)	5%	1%	6%	9%	2%	4%	11%	-
Transmission ratio (at 1600 MPa)	3%	2%	5%	12%	12%	1%	4%	-

Lastly, there are numerous modelling approaches in the literature that attempt to describe granular compaction and comminution [112, 120, 122], with some models requiring adjustable parameters that have no fundamental physical basis [123]. In an attempt to incorporate these granular behaviours, the breakage model first developed by Einav [124] and then expanded upon by Cil et al. [46], takes into account relative density, loading

rate, and particle size distribution when describing granular behaviour. The micro-mechanical model of Cil et al. [46] was initially developed for soil mechanics [125–127]. Cil et al. [46] noted the importance of incorporating relative density, porosity, particle size distribution, and particle breakage into constitutive modelling of brittle granular materials. These parameters are not often considered in classical failure models that only account for strength to void ratios [128]. The Cil et al. [46] study highlighted the complex nature of granular ceramics experiencing multi-axial loading conditions during projectile impact and introduced the breakage model as a potential solution. The breakage term, described by (4.6), represents as an internal state variable in a computational modelling framework that accounts for how the particle sizes evolve and become smaller during loading:

$$B_r = \frac{\int_{d_m}^{d_M} (F(d) - F_0(d))d^{-1}dd}{\int_{d_m}^{d_M} (F_u(d) - F_0(d))d^{-1}dd} \quad (4.6)$$

The relative breakage term is integrated between the grain size, $d_{m,M}$, over the initial distribution $F_0(d)$, current distribution $F(d)$, and ultimate distribution $F_u(d)$. $F_0(d)$ can be measured before each experiment, although in this study we did random sampling of the suite of experiments at given size to measure those size distributions. $F(d)$ represents the size distribution at an intermediate state (e.g., Figure 4.12 & Figure 4.13). From the current experiments, $F_u(d)$ is unknown, however it may take a similar functional form to those in Figure 4.12 and Figure 4.13 for $F(d)$. Note that many fits (e.g., Weibull, log-normal, exponential) were attempted for the data in Figures 4.12 and 4.13, and none provided adequate description of the data. In the study by Einav [124], tests were performed to various strains and particle sizes measured, $F_u(d)$ was assumed to take the functional form of $\frac{d}{d_M}^{3-\alpha}$ where α is a constant, and the breakage model form was derived. Notable in the results presented in the paper by Einav [124] and others in the literature [46] is that it is commonly assumed that the lower and upper bound of the size distributions in $F_0(d)$, $F(d)$, and $F_u(d)$ remain the same during compaction. Our results on alumina and boron carbide show that the lower and upper bounds likely changes during compaction, and so that raises the question of how these distributions evolve. Unravelling the path of breakage warrants future work given the complexity of the competition between scale-dependent compaction, flow, fracture, comminution, and surface abrasion.

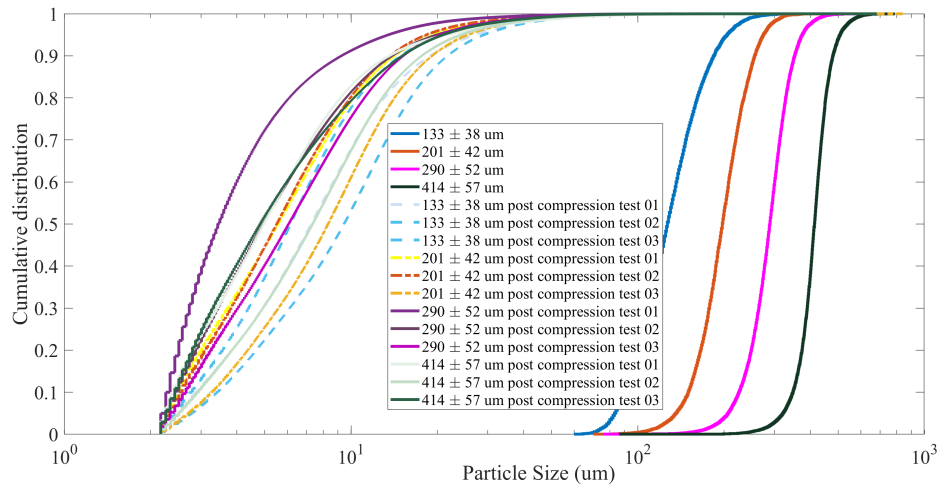


FIGURE 4.12: The cumulative distribution of the particles for Al_2O_3 powder for the range of particles: $133 \pm 38 \mu\text{m}$, $201 \pm 42 \mu\text{m}$, $290 \pm 52 \mu\text{m}$, and $414 \pm 57 \mu\text{m}$.

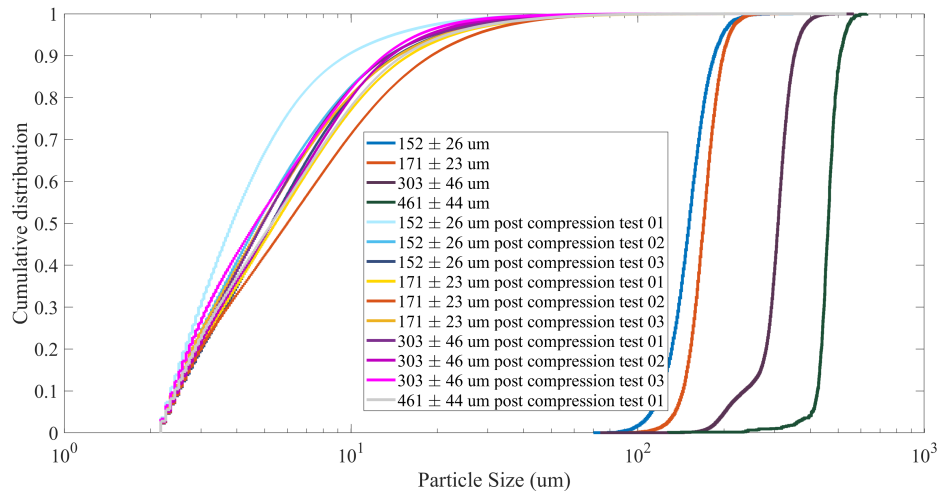


FIGURE 4.13: The cumulative distribution of the particles for B_4C powder for the range of particles: $152 \pm 26 \mu\text{m}$, $171 \pm 23 \mu\text{m}$, $303 \pm 46 \mu\text{m}$, and $461 \pm 44 \mu\text{m}$.

As evident by the Cil et al. [46] study and others ([51, 112]), limited experimental data for granular advanced ceramics exists for parametrizing the breakage model and often times sand is used as a substitute. Sand is likely not a good analogue for accurate parameterization when modelling advanced ceramics. The work presented in this study builds from the validation attempts conducted by Cil et al. [46]. More specifically, the particle distribution data of alumina and boron carbide can be used for validating the breakage index. Beyond this, the data for hydro-static pressure response as a function of porosity provided in this study can verify the particle gradation parameter. This will be valuable in the literature.

Taken together, these results highlight the importance of particle size *and* shape of the granular behaviour of materials. The mechanical testing results were linked with particle size, shape, and failure features before and after the experiments. It was observed that the particles for the alumina were elongated (aspect ratio < 1) with some initial internal cracking and porosity. For boron carbide, the particles had aspect ratios close to 1 and were mostly near-spherical. Post-experiment, increased fragmentation in the larger particles for alumina were observed when compared to smaller particles, with multiple sites of thin surface fractures that are believed to represent particle failure through bending. The boron carbide exhibited greater fragmentation, surface comminution and shallow fractures. Overall, it may be said these trends are thought to occur based on the following ideas:

- i The geometry of both materials is vastly different. Al_2O_3 is elongated and jagged while B_4C is spherical.
- ii The Al_2O_3 had a large number of larger particles postmortem, with multiple surface fractures. B_4C on the other hand, fragmented into many more minuscule particles with shallow fractures and surface comminution.
- iii Larger B_4C particles are stiffer when compared to large Al_2O_3 .
- iv Al_2O_3 was initially more porous than B_4C .

4.5.1 Concluding Remarks

Conducting uniaxial quasi-static compaction experiments using the instrumented die, we determined the triaxial behaviour of granular Al_2O_3 and B_4C as a function of particle size and shape. The results showed particle size influenced the compaction curves where hydro-static pressure is related as a function of porosity, the bulk modulus response as a function of hydro-static pressure, and the transmission ratio as a function of applied stress. The trends described in this chapter are thought to be influenced by the failure exhibiting in the material during compaction. Further research must be conducted to better understand the particle size dependencies on mechanical properties of granular Al_2O_3 and B_4C , so that improvements can be made in material design.

Chapter 5

Conclusion

5.1 Conclusion

In this thesis the objective was to investigate the effect of particle size and material characteristics on flow behaviour of granular materials. To accomplish this, two approaches were used to determine the confined compression response of granular materials as a function of ranging particle sizes. In the first case, granular stainless steel 316 was investigated using a uniaxial confined compaction experiment apparatus under quasi-static loading conditions. The results showed an influence of particle size in the compaction curves where hydro-static pressure is described as a function of porosity. In these experiments, the bulk modulus was determined to be sensitive with respect to average particle sizes. This is believed to occur due to the failure mechanism that is likely related to the particle size, shape, and initial porosity. The smaller particles ($127 \pm 34 \mu\text{m}$) appeared to exhibit higher flow stresses and underwent plastic deformation, while the larger particles ($487 \pm 98 \mu\text{m}$) developed micro-cracks which lead to fracture. The effects of particle-size dependencies were unique in the hydro-static-pressure-porosity curve up to a threshold of 30% porosity. The failure path of this material is believed to be dictated by the particle shape. Brittle failure was likewise observed when analyzing the postmortem SEM images. With this, the apparatus used to record the information was deemed sufficient and reliable when conducting multiple tests. Comparable brittle-ductile transition behaviour has been observed before Roberts and Rowe [96], however, further research must be conducted to expand our understanding of particle size effects on mechanical properties of

the material in order to better establish failure regimes exhibited during triaxial loading conditions.

The second approach pursued in this thesis utilized the instrumented die experimental apparatus, observing the quasi-static uniaxial confined compression response of granular Al_2O_3 and B_4C as a function of particle size and shape. The instrumented die was more robust than the TWC, showing less abrasion to the void walls. The results showed an influence of particle size in the compaction curves where porosity is related as a function of hydro-static pressure, the bulk modulus is related to hydro-static pressure, and the transmission ratio is related to the applied stress. The elongated alumina powder showed large variations among each sample tested for the hydro-static response, while the boron carbide powder, with an aspect ratio close to 1, was less variable. Such results underline the importance of particle geometry when linking with material strength. In the bulk modulus response of both materials, the alumina showed no clear trend as a function of particle size. Observing the boron carbide response, we see that as the particle size increases the change in the bulk modulus increases in addition to a vertical shift of the material trends. This is believed to be influenced by two ideas: the initial elongated geometry of the alumina and the way both materials fail through fragmentation. The Al_2O_3 initially was elongated and so the fractures are interpreted to be a consequence of bending resulting from the less-than-spherical particle shape for this material. The B_4C fragments highlighted some shallow surface fracturing and the presence of many smaller comminuted fragments which is believed to handle higher compaction pressures. It is important to note the considerable range in results at a set particle size. Such behaviour is believed to be a result of large particle size standard deviation which can effect material responses as high as 24% as seen in Table 4.6.

5.2 Implications

In this thesis we investigated the mechanical response of granular stainless steel 316, alumina, and boron carbide by testing the powdered materials under quasi-static confined compression experiments. All three granular materials depicted unique trends when placed in these stress states. Researchers in the past have completed similar experiments, however, the importance of particle-size dependant behaviour was not well documented. In addition, these types of experiments were limited due to their expensive nature and

complexity when using a powdered ceramic material. Specifically, the hard nature of advanced ceramics creates hardships when attempting to record the compaction behaviour. Experimental results of the crush curves, bulk modulus, and friction response presented in this thesis, provide valuable data-sets to the additive manufacturing industry and defence design literature.

Altogether this work makes the following contributions:

- ▶ Understanding the shortcomings of stainless steel 316 particle variability, characteristics and product performance to ultimately improve repeatability of additive manufacturing in large scale production.
- ▶ Emphasizing the effect of particle size and shape on: flow stress, variability in strength, irregularity in bulk modulus for improved material design in ballistic protection.
- ▶ Recognizing that fracture, fragmentation, and particle shape of granular advanced ceramics can be tailored to maximize projectile erosion and energy dissipation during blast-mitigating scenarios.
- ▶ Experimental data of the granular materials can be used to validate existing failure models to more accurately describe granular behaviour in simulations by incorporating particle-size length scales in computer models.

5.3 Future Work and Recommendations

To date, there has been a limited amount of data that looks at particle-size dependent failure behaviour of granular advanced materials. The data generated in this thesis is useful for validation and development of computational models. The limitations in accurately predicting failure, can be addressed by including length scales in failure models (i.e. particle size, particle geometry). This thesis established a rigorous methodology for compacting granular metallics and ceramics with initial steps to validating and further developing failure models for predicting material failure in defence applications. In order to build upon the current work, the following improvements are suggested:

-
- i Consider measuring all principle strain directions for granular Al_2O_3 and B_4C using strain gauges to compute the yield profiles in existent models such as the Drucker-Prager material model [129].
 - ii Compacting the materials under dynamic strain rates, as failure has been noted to be rate dependant [130, 131]. This could be done using the split Hopkison Kolsky bar.
 - iii Conduct calibration compaction tests using a soft material to validate material properties of experimental components used, accounting for compliance in testing, similarly seen in the Meyer and Faber [42] study.
 - iv Consider testing a wider range of particle size for advanced ceramics to account for the various geometries seen during impact.
 - v Consider compression experiments using a combination of granular advanced ceramic such as: SiC, TiC, WC, to observe any inter-connected particle behaviour or bounded experimental trends. The idea of constraining the experiment by controlling particle size (50 μm to 500 μm) and proportions (10 % to 90 %) could optimize the mechanical performance.
 - vi Investigate the yielding function in densification of granular Al_2O_3 and B_4C in order to modify the Drucker-Prager failure model incorporating particle-size dependencies. Such empirical models are heavily used in granular failure simulation.

Bibliography

- [1] Jeffrey Malcolm Benson and Ettienne Snyders. The need for powder characterization in the additive manufacturing industry and the establishment of a national facility. *The South African Journal of Industrial Engineering*, 26(2):104, August 2015. ISSN 22247890. doi: 10.7166/26-2-951.
- [2] M. H. Es-Saheb. Uniaxial strain rate effects in pharmaceutical powders during cold compaction. *Journal of Materials Science*, 27(15):4151–4159, 1992. ISSN 0022-2461, 1573-4803. doi: 10.1007/BF01105119.
- [3] Andrew Feeney, Sakalima Sikaneta, Patrick Harkness, and Margaret Lucas. Ultrasonic compaction of granular geological materials. *Ultrasonics*, 76:136–144, April 2017. ISSN 0041624X. doi: 10.1016/j.ultras.2017.01.004.
- [4] Jian-gu Qian, Jian-bo Gu, Xiao-qiang Gu, and Mao-song Huang. Discrete numerical modeling of granular materials considering crushability. *Journal of Mountain Science*, 14(4):758–770, April 2017. ISSN 1672-6316, 1993-0321. doi: 10.1007/s11629-016-4051-y.
- [5] C. Davalos, J. Cante, J.A. Hernandez, and J. Oliver. On the numerical modeling of granular material flows via the Particle Finite Element Method (PFEM). *International Journal of Solids and Structures*, 71:99–125, October 2015. ISSN 00207683. doi: 10.1016/j.ijsolstr.2015.06.013.
- [6] M.J. Jiang, H.-S. Yu, and D. Harris. A novel discrete model for granular material incorporating rolling resistance. *Computers and Geotechnics*, 32(5):340–357, July 2005. ISSN 0266352X. doi: 10.1016/j.compgeo.2005.05.001.

- [7] I M Cameron and D T Gethin. Exploration of die wall friction for powder compaction using a discrete finite element modelling technique. page 20, 2001. doi: 10.1088/0965-0393/9/4/304.
- [8] Andreas Krell and Elmar Strassburger. Order of influences on the ballistic resistance of armor ceramics and single crystals. *Materials Science and Engineering: A*, 597:422–430, 03 2014. doi: 10.1016/j.msea.2013.12.101.
- [9] Sachith Dunatunga and Ken Kamrin. Continuum modelling and simulation of granular flows through their many phases. *Journal of Fluid Mechanics*, 779:483–513, September 2015. ISSN 0022-1120, 1469-7645. doi: 10.1017/jfm.2015.383.
- [10] J. D. Goddard. Continuum Modeling of Granular Media. *Applied Mechanics Reviews*, 66(5):050801, May 2014. ISSN 0003-6900. doi: 10.1115/1.4026242.
- [11] N.P. Kruyt, I. Agnolin, S. Luding, and L. Rothenburg. Micromechanical study of elastic moduli of loose granular materials. *Journal of the Mechanics and Physics of Solids*, 58(9):1286–1301, September 2010. ISSN 00225096. doi: 10.1016/j.jmps.2010.06.003.
- [12] J. Tomas. Product Design of Cohesive Powders– Mechanical Properties, Compression and Flow Behavior. *Chemical Engineering & Technology*, 27(6):605–618, June 2004. ISSN 0930-7516, 1521-4125. doi: 10.1002/ceat.200406134.
- [13] Conor P. Schlick, Austin B. Isner, Ben J. Freireich, Yi Fan, Paul B. Umbanhowar, Julio M. Ottino, and Richard M. Lueptow. A continuum approach for predicting segregation in flowing polydisperse granular materials. *Journal of Fluid Mechanics*, 797:95–109, June 2016. ISSN 0022-1120, 1469-7645. doi: 10.1017/jfm.2016.260.
- [14] Amir R. Khoei. Introduction. In *Computational Plasticity in Powder Forming Processes*, pages 1–18. Elsevier, 2005. ISBN 978-0-08-044636-3. doi: 10.1016/B978-008044636-3/50001-8.
- [15] John H. Martin, Brennan D. Yahata, Jacob M. Hundley, Justin A. Mayer, Tobias A. Schaedler, and Tresa M. Pollock. 3D printing of high-strength aluminium alloys. *Nature*, 549(7672):365–369, September 2017. ISSN 0028-0836, 1476-4687. doi: 10.1038/nature23894.

- [16] Christopher T Schade, Thomas F Murphy, and Chris Walton. Development of atomized powders for additive manufacturing. page 11.
- [17] A.B. Spierings, N. Herres, and G. Levy. Influence of the particle size distribution on surface quality and mechanical properties in AM steel parts. *Rapid Prototyping Journal*, 17(3):195–202, April 2011. ISSN 1355-2546. doi: 10.1108/13552541111124770.
- [18] Yun Bai, Grady Wagner, and Christopher B. Williams. Effect of Particle Size Distribution on Powder Packing and Sintering in Binder Jetting Additive Manufacturing of Metals. *Journal of Manufacturing Science and Engineering*, 139(8):081019, June 2017. ISSN 1087-1357. doi: 10.1115/1.4036640.
- [19] J.K. Prescott and R.A. Barnum. On powder flowability. *Pharmaceutical Technology*, 24:60–84+236, 01 2000.
- [20] M.S. Kadiri, A. Michrafy, and J.A. Dodds. Pharmaceutical powders compaction: Experimental and numerical analysis of the density distribution. *Powder Technology*, 157(1-3):176–182, 2005. ISSN 00325910. doi: 10.1016/j.powtec.2005.05.025.
- [21] A. Michrafy, M.S. Kadiri, and J.A. Dodds. Wall Friction and its Effects on the Density Distribution in the Compaction of Pharmaceutical Excipients. *Chemical Engineering Research and Design*, 81(8):946–952, September 2003. ISSN 02638762. doi: 10.1205/026387603322482185.
- [22] David Train. An Investigatin into the Compaction of Powders. *Journal of Pharmacy and Pharmacology*, 8(1):745–761, 1956. ISSN 00223573. doi: 10.1111/j.2042-7158.1956.tb12206.x.
- [23] S M Walley. Historical review of high strain rate and shock properties of ceramics relevant to their application in armour. *Advances in Applied Ceramics*, 109(8):446–466, November 2010. ISSN 1743-6753, 1743-6761. doi: 10.1179/174367609X422180.
- [24] André Ben-Hur da Silva Figueiredo, Édio Pereira Lima Júnior, Alaelson Vieira Gomes, Gabriel Burlandy Mota de Melo, Sergio Neves Monteiro, and Ronaldo Sergio de Biasi. Response to Ballistic Impact of Alumina-UHMWPE Composites. *Materials Research*, 21(5), August 2018. ISSN 1980-5373, 1516-1439. doi: 10.1590/1980-5373-mr-2017-0959.

- [25] Eugene Medvedovski. Ballistic performance of armour ceramics: Influence of design and structure. Part 2. *Ceramics International*, 36(7):2117–2127, 2010. ISSN 02728842. doi: 10.1016/j.ceramint.2010.05.022.
- [26] Richard Lane, Benjamin Craig, and Wade Babcock. Materials for Blast and Penetration Resistance. 6(4):7, 2001.
- [27] T. Behner, A. Heine, and M. Wickert. Dwell and penetration of tungsten heavy alloy long-rod penetrators impacting unconfined finite-thickness silicon carbide ceramic targets. *International Journal of Impact Engineering*, 95:54–60, September 2016. ISSN 0734743X. doi: 10.1016/j.ijimpeng.2016.04.008.
- [28] Jeffrey J Swab, Andrew A Wereszczak, Jason Tice, Russ Caspe, Reuben H Kraft, and Jane W Adams. Mechanical and Thermal Properties of Advanced Ceramics for Gun Barrel Applications. page 92.
- [29] H.P Kirchner and R.M Gruver. The elevated temperature flexural strength and impact resistance of alumina ceramics strengthened by quenching. *Materials Science and Engineering*, 13(1):63–69, January 1974. ISSN 00255416. doi: 10.1016/0025-5416(74)90022-6.
- [30] T. Behner, A. Heine, and M. Wickert. Dwell and penetration of tungsten heavy alloy long-rod penetrators impacting unconfined finite-thickness silicon carbide ceramic targets. *International Journal of Impact Engineering*, 95:54–60, September 2016. ISSN 0734743X. doi: 10.1016/j.ijimpeng.2016.04.008.
- [31] Andreas Krell and Elmar Strassburger. Order of influences on the ballistic resistance of armor ceramics and single crystals. *Materials Science and Engineering: A*, 597:422–430, March 2014. ISSN 09215093. doi: 10.1016/j.msea.2013.12.101.
- [32] N.F. Mott, E.H. Linfoot, and Dennis Grady. *A Theory of Fragmentation*, pages 207–225. 01 2006. doi: 10.1007/978-3-540-27145-1_9.
- [33] D E Grady and M E Kipp. Mechanisms of dynamic fragmentation: Factors governing fragment size. page 4, 1985.
- [34] Sai Sarva and Sia Nemat-Nasser. Dynamic compressive strength of silicon carbide under uniaxial compression. *Materials Science and Engineering: A*, 317(1):140–144, 2001.

- [35] J. D. Hogan, Lukasz Farbaniec, M. Shaeffer, and K. T. Ramesh. Jace13353.pdf, 2014.
- [36] James David Hogan, Lukasz Farbaniec, Debjoy Mallick, Vladislav Domnich, Kanak Kuwelkar, Tomoko Sano, James W. McCauley, and Kaliat T. Ramesh. Fragmentation of an advanced ceramic under ballistic impact: Mechanisms and microstructure. *International Journal of Impact Engineering*, 102:47–54, April 2017. ISSN 0734743X. doi: 10.1016/j.ijimpeng.2016.12.008.
- [37] Donald A. Shockey, A. H. Marchand, S. R. Skaggs, G. E. Cort, M. W. Burkett, and R. Parker. Failure phenomenology of confined ceramic targets and impacting rods. *International Journal of Impact Engineering*, 9(3):263–275, 1990.
- [38] D. E. Grady. Fragmentation of solids under impulsive stress loading. *Journal of Geophysical Research: Solid Earth*, 86(B2):1047–1054, February 1981. ISSN 01480227. doi: 10.1029/JB086iB02p01047.
- [39] L. Farbaniec, J.D. Hogan, K.Y. Xie, M. Shaeffer, K.J. Hemker, and K.T. Ramesh. Damage evolution of hot-pressed boron carbide under confined dynamic compression. *International Journal of Impact Engineering*, 99:75–84, January 2017. ISSN 0734743X. doi: 10.1016/j.ijimpeng.2016.09.008.
- [40] J. D. Hogan, A. K. Robinson, Joey Tilson, Erez Krinsky, and K. T. Ramesh. On the Behavior of Fragmented Brittle Materials. June 2015.
- [41] Timothy J. Holmquist and Gordon R. Johnson. The failed strength of ceramics subjected to high-velocity impact. *Journal of Applied Physics*, 104(1):013533, July 2008. ISSN 0021-8979, 1089-7550. doi: 10.1063/1.2955456.
- [42] L. W. Meyer and I. Faber. Investigations on granular ceramics and ceramic powder. *Le Journal de Physique IV*, 7(C3):C3–565, 1997.
- [43] T.J. Vogler, M.Y. Lee, and D.E. Grady. Static and dynamic compaction of ceramic powders. *International Journal of Solids and Structures*, 44(2):636–658, January 2007. ISSN 00207683. doi: 10.1016/j.ijsolstr.2006.05.001.
- [44] Abhisek Choudhary, Pandu Ramavath, Papiya Biswas, Nukala Ravi, and Roy Johnson. Experimental Investigation on Flowability and Compaction Behavior

- of Spray Granulated Submicron Alumina Granules. *ISRN Ceramics*, 2013:1–6, 2013. ISSN 2090-7508. doi: 10.1155/2013/264194.
- [45] J.Y. Huang, S.S. Hu, S.L. Xu, and S.N. Luo. Fractal crushing of granular materials under confined compression at different strain rates. *International Journal of Impact Engineering*, 106:259–265, August 2017. ISSN 0734743X. doi: 10.1016/j.ijimpeng.2017.04.021.
- [46] Mehmet B. Cil, Ryan C. Hurley, and Lori Graham-Brady. A rate-dependent constitutive model for brittle granular materials based on breakage mechanics. *Journal of the American Ceramic Society*, page jace.16376, March 2019. ISSN 0002-7820, 1551-2916. doi: 10.1111/jace.16376.
- [47] Bradley E. Martin, Md. E. Kabir, Bo Song, and Wayne Chen. Compressive behavior of fine sand. Technical Report SAND2010-2289, 984089, April 2010.
- [48] Meifeng Cai and Dongmei Liu. Study of failure mechanisms of rock under compressive–shear loading using real-time laser holography. *International Journal of Rock Mechanics and Mining Sciences*, 46(1):59–68, January 2009. ISSN 13651609. doi: 10.1016/j.ijrmms.2008.03.010.
- [49] J. Huang, S. Xu, and S. Hu. Effects of grain size and gradation on the dynamic responses of quartz sands. *International Journal of Impact Engineering*, 59:1–10, September 2013. ISSN 0734743X. doi: 10.1016/j.ijimpeng.2013.03.007.
- [50] John P. Borg and Tracy J. Vogler. Mesoscale calculations of the dynamic behavior of a granular ceramic. *International Journal of Solids and Structures*, 45(6):1676–1696, March 2008. ISSN 00207683. doi: 10.1016/j.ijsolstr.2007.10.027.
- [51] D.R. Curran, L. Seaman, T. Cooper, and D.A. Shockey. Micromechanical model for comminution and granular flow of brittle material under high strain rate application to penetration of ceramic targets. *International Journal of Impact Engineering*, 13(1):53–83, January 1993. ISSN 0734743X. doi: 10.1016/0734-743X(93)90108-J.
- [52] M.F. Ashby and S.D. Hallam (Née Cooksley). The failure of brittle solids containing small cracks under compressive stress states. *Acta Metallurgica*, 34(3):497–510, March 1986. ISSN 00016160. doi: 10.1016/0001-6160(86)90086-6.

- [53] Joanne T. Fredrich, Brian Evans, and Teng-Fong Wong. Effect of grain size on brittle and semibrittle strength: Implications for micromechanical modelling of failure in compression. *Journal of Geophysical Research*, 95(B7):10907, 1990. ISSN 0148-0227. doi: 10.1029/JB095iB07p10907.
- [54] Amnaya Awasthi, Ziyi Wang, Natalie Broadhurst, and Philippe Geubelle. Impact response of granular layers. *Granular Matter*, 17(1):21–31, February 2015. ISSN 1434-5021, 1434-7636. doi: 10.1007/s10035-015-0547-3.
- [55] Michael A. Homel, James E. Guilkey, and Rebecca M. Brannon. Continuum effective-stress approach for high-rate plastic deformation of fluid-saturated geomaterials with application to shaped-charge jet penetration. *Acta Mechanica*, 227(2):279–310, February 2016. ISSN 0001-5970, 1619-6937. doi: 10.1007/s00707-015-1407-2.
- [56] John Dalsgaard Sørensen and Hans F. Burcharth. Reliability analysis of geotechnical failure modes for vertical wall breakwaters. *Computers and Geotechnics*, 26(3-4):225–245, April 2000. ISSN 0266352X. doi: 10.1016/S0266-352X(99)00040-3.
- [57] A. F. Fossum and R. M. Brannon. On a viscoplastic model for rocks with mechanism-dependent characteristic times. *Acta Geotechnica*, 1(2):89–106, September 2006. ISSN 1861-1125, 1861-1133. doi: 10.1007/s11440-006-0010-z.
- [58] M.J. Adams, M.A. Mullier, and J.P.K. Seville. Agglomerate strength measurement using a uniaxial confined compression test. *Powder Technology*, 78(1):5–13, January 1994. ISSN 00325910. doi: 10.1016/0032-5910(93)02777-8.
- [59] W.M. Ye, Y.J. Cui, L.X. Qian, and B. Chen. An experimental study of the water transfer through confined compacted GMZ bentonite. *Engineering Geology*, 108(3-4):169–176, October 2009. ISSN 00137952. doi: 10.1016/j.enggeo.2009.08.003.
- [60] Seth I. Soil Behaviour Characteristics Under Applied Forces in Confined and Unconfined Spaces. In Stanisaw Grundas, editor, *Advances in Agrophysical Research*. InTech, July 2013. ISBN 978-953-51-1184-9. doi: 10.5772/52774.
- [61] Mengcheng Zhou, Shangyu Huang, Jianhua Hu, Yu Lei, Yong Xiao, Bei Li, Shiwei Yan, and Fangli Zou. A density-dependent modified Drucker-Prager Cap model for die compaction of Ag_{57.6}-Cu_{22.4}-Sn₁₀-In₁₀ mixed metal powders. *Powder*

- Technology*, 305:183–196, January 2017. ISSN 00325910. doi: 10.1016/j.powtec.2016.09.061.
- [62] Kathryn Dannemann. Ceramic Phenomenological Experiments- Compressive Strength of SiC. page 65, 2004.
- [63] Sung-Tae Hong, Yuri Hovanski, Curt A. Lavender, and K. Scott Weil. Investigation of Die Stress Profiles During Powder Compaction Using Instrumented Die. *Journal of Materials Engineering and Performance*, 17(3):382–386, June 2008. ISSN 1059-9495, 1544-1024. doi: 10.1007/s11665-008-9229-1.
- [64] Hjalmar Staf, Erik Olsson, Per Lindskog, and Per-Lennart Larsson. Determination of the Frictional Behavior at Compaction of Powder Materials Consisting of Spray-Dried Granules. *Journal of Materials Engineering and Performance*, 27(3):1308–1317, March 2018. ISSN 1059-9495, 1544-1024. doi: 10.1007/s11665-018-3205-1.
- [65] Per Lindskog, Daniel C. Andersson, and Per-Lennart Larsson. An Experimental Device for Material Characterization of Powder Materials. *Journal of Testing and Evaluation*, 41(3):20120107, May 2013. ISSN 00903973. doi: 10.1520/JTE20120107.
- [66] D.M.M. Guyoncourt, J.H. Tweed, A. Gough, J. Dawson, and L. Pater. Constitutive data and friction measurements of powders using instrumented die. *Powder Metallurgy*, 44(1):25–33, January 2001. ISSN 0032-5899, 1743-2901. doi: 10.1179/003258901666130.
- [67] R J Crawford and D W Paul. Radial and axial die pressures during solid phase compaction of polymeric powders. page 6.
- [68] I Sridhar and N.A Fleck. Yield behaviour of cold compacted composite powders. *Acta Materialia*, 48(13):3341–3352, August 2000. ISSN 13596454. doi: 10.1016/S1359-6454(00)00151-8.
- [69] John T. Chojnacki and Weinong W. Chen. Mechanical Response of Borosilicate and Soda-Lime Glass Under Dynamic Triaxial Compression. *Journal of Dynamic Behavior of Materials*, 2(2):251–258, June 2016. ISSN 2199-7446, 2199-7454. doi: 10.1007/s40870-016-0063-5.

- [70] S.C. Lee and K.T. Kim. A study on the Cap model for metal and ceramic powder under cold compaction. *Materials Science and Engineering: A*, 445-446:163–169, February 2007. ISSN 09215093. doi: 10.1016/j.msea.2006.09.013.
- [71] Stefania Cacace, Ali Gökhan Demir, and Quirico Semeraro. Densification Mechanism for Different Types of Stainless Steel Powders in Selective Laser Melting. *Procedia CIRP*, 62:475–480, 2017. ISSN 22128271. doi: 10.1016/j.procir.2016.06.010.
- [72] James Hogan, Andrew Robinson, Joe Tilson, Erez Krinsky, and K.T. Ramesh. On the behavior of fragmented brittle materials. 06 2015.
- [73] Hong Wang and K.T Ramesh. Dynamic strength and fragmentation of hot-pressed silicon carbide under uniaxial compression. *Acta Materialia*, 52(2):355–367, January 2004. ISSN 13596454. doi: 10.1016/j.actamat.2003.09.036.
- [74] Dennis E. Grady and Marlin E. Kipp. Fragmentation properties of metals. *International Journal of Impact Engineering*, 20(1-5):293–308, January 1997. ISSN 0734743X. doi: 10.1016/S0734-743X(97)87502-1.
- [75] K. E. N’souglo, A. Srivastava, S. Osovski, and J. A. Rodríguez-Martínez. Random distributions of initial porosity trigger regular necking patterns at high strain rates. *Proceedings of the Royal Society A: Mathematical, Physical and Engineering Science*, 474(2211):20170575, March 2018. ISSN 1364-5021, 1471-2946. doi: 10.1098/rspa.2017.0575.
- [76] Ganesh Rana. 3D Constitutive Equations, 2014.
- [77] Teodor M Atanackovic and Ardeshir Guran. Theory of Elasticity for Scientists and Engineers. page 378.
- [78] T G Sitharam and L Govindaraju. Applied Elasticity for Engineers. *National Programme on Technology Enhanced Learning (NPTEL)*, page 21.
- [79] Bandar AL-Mangour. Powder metallurgy of stainless steel: State-of-the art, challenges, and development. page 45.
- [80] Eric Maynard. Five fundamentals for effective blend sampling. *Powder and Bulk Engineering Magazine*, page 3, 2015.

- [81] G. Bahar Basim and Mohsen Khalili. Particle size analysis on wide size distribution powders; effect of sampling and characterization technique. *Advanced Powder Technology*, 26(1):200–207, January 2015. ISSN 09218831. doi: 10.1016/j.appt.2014.09.009.
- [82] Carl Levoguer. Using laser diffraction to measure particle size and distribution. *Metal Powder Report*, 68(3):15–18, May 2013. ISSN 00260657. doi: 10.1016/S0026-0657(13)70090-0.
- [83] Roman Engeli, Thomas Etter, Simone Hovel, and Konrad Wegener. Processability of different IN738LC powder batches by selective laser melting. *Journal of Materials Processing Technology*, 229:484–491, March 2016. ISSN 09240136. doi: 10.1016/j.jmatprotec.2015.09.046.
- [84] N. A Fleck and A. C. F Cocks. *IUTAM Symposium on Mechanics of Granular and Porous Materials: Proceedings of the IUTAM Symposium Held in Cambridge, U.K., 15-17 July 1996*. Springer Netherlands, Dordrecht, 1997. ISBN 978-94-011-5520-5. OCLC: 851391570.
- [85] Mauricio Barrera and Hector Sanchez. Design of a Die for the Cold Compaction Calibration of Powdered Materials. *Suplemento de la Revista Latinoamericana de Metalurgia y Materiales S*, 1:223–234, 2009.
- [86] Cesar A. Sciammarella and F. M. Sciammarella. *Experimental Mechanics of Solids*. Wiley, 2012.
- [87] Daesung Kim, Sanghoon Kim, Hyunho Shin, and Kyong Yop Rhee. Feasibility of measuring the pressure vs. volume relationship of compressible solids using a thick-walled cylinder. *Powder Technology*, 322:490–496, December 2017. ISSN 00325910. doi: 10.1016/j.powtec.2017.08.052.
- [88] G. Gustafsson, H.-Å. Häggblad, P. Jonsén, and P. Marklund. Determination of bulk properties and fracture data for iron ore pellets using instrumented confined compression experiments. *Powder Technology*, 241:19–27, June 2013. ISSN 00325910. doi: 10.1016/j.powtec.2013.02.030.
- [89] Benjy Marks, Bjørnar Sandnes, Guillaume Dumazer, Jon Alm Eriksen, and Knut Jørgen Måløy. Compaction of granular material inside confined geometries. *Frontiers in Physics*, 3, June 2015. ISSN 2296-424X. doi: 10.3389/fphy.2015.00041.

- [90] Herman J. C. Berendsen. *A Student's Guide to Data and Error Analysis*. Student's Guides. Cambridge University Press, 2011. doi: 10.1017/CBO9780511921247.
- [91] R W Heckel. Density-Pressure Relationships in Powder Compaction. page 7.
- [92] R. Holtzman, D. B. Silin, and T. W. Patzek. Mechanical properties of granular materials: A variational approach to grain-scale simulations. *International Journal for Numerical and Analytical Methods in Geomechanics*, 33(3):391–404, February 2009. ISSN 03639061, 10969853. doi: 10.1002/nag.725.
- [93] V. Magnanimo, L. La Ragione, J. T. Jenkins, P. Wang, and H. A. Makse. Characterizing the shear and bulk moduli of an idealized granular material. *EPL (Europhysics Letters)*, 81(3):34006, February 2008. ISSN 0295-5075, 1286-4854. doi: 10.1209/0295-5075/81/34006.
- [94] N.W. Page and M.K. Warpenius. Loading relations for metal powders pressed to high density. *Powder Technology*, 61(1):87–94, April 1990. ISSN 00325910. doi: 10.1016/0032-5910(90)80069-B.
- [95] Dietmar Schulze. Stresses in Silos. <http://www.dietmar-schulze.de/spanne.html>, 2019.
- [96] R J Roberts and R C Rowe. Brittle-ductile transitions in die compaction of sodium chloride. page 5, 1989.
- [97] Bin Liu, WenMao Huang, Lu Huang, and HaoWei Wang. Size-dependent compression deformation behaviors of high particle content B4C/Al composites. *Materials Science and Engineering: A*, 534:530–535, February 2012. ISSN 09215093. doi: 10.1016/j.msea.2011.12.003.
- [98] Biplob Mitra, Jon Hilden, and James D. Litster. Effects of the granule composition on the compaction behavior of deformable dry granules. *Powder Technology*, 291: 487–498, April 2016. ISSN 00325910. doi: 10.1016/j.powtec.2016.01.009.
- [99] Göran Frenning. Analysis of pharmaceutical powder compaction using multiplicative hyperelasto-plastic theory. *Powder Technology*, 172(2):103–112, March 2007. ISSN 00325910. doi: 10.1016/j.powtec.2006.11.001.
- [100] Eduardo Suescun Florez, Sina Kashuk, Magued Iskander, and Stephan Bless. Predicting the Uniaxial Compressive Response of Granular Media over a Wide Range

- of Strain Rates Using the Strain Energy Density Concept. *Journal of Dynamic Behavior of Materials*, 1(3):330–346, September 2015. ISSN 2199-7446, 2199-7454. doi: 10.1007/s40870-015-0028-0.
- [101] I. Cristofolini, A. Molinari, G. Pederzini, and A. Rambelli. Study of the uniaxial cold compaction of AISI 316L stainless steel powders through single action tests. *Powder Technology*, 295:284–295, July 2016. ISSN 00325910. doi: 10.1016/j.powtec.2016.03.045.
- [102] B V Ponraj and A Rajadurai. Parametric study on the compacting and sintering behaviour of powder metallurgical stainless steel components. (9):4, 2015.
- [103] C. A. Lowe and A. W. Longbottom. Effect of particle distribution on the compaction behavior of granular beds. *Physics of Fluids*, 18(6):066101, 2006. ISSN 10706631. doi: 10.1063/1.2213641.
- [104] A. Tarokh and A. Fakhimi. Relationship Between Grain Size and Fracture Properties of Rock. In *ARMA-2013-168*, page 10, ARMA, January 2013. American Rock Mechanics Association. ISBN 978-0-9894844-0-4.
- [105] R. H. Brzesowsky, S. J. T. Hangx, N. Brantut, and C. J. Spiers. Compaction creep of sands due to time-dependent grain failure: Effects of chemical environment, applied stress, and grain size. *Journal of Geophysical Research: Solid Earth*, 119(10):7521–7541, October 2014. ISSN 21699313. doi: 10.1002/2014JB011277.
- [106] L. Perez-Gandarillas, A. Mazor, D. Souriou, O. Lecoq, and A. Michrafy. Compaction behaviour of dry granulated binary mixtures. *Powder Technology*, 285:62–67, November 2015. ISSN 00325910. doi: 10.1016/j.powtec.2015.05.003.
- [107] R.M Nedderman. *Statics and Kinematics of Granular Materials - Method of Differential_slices.Pdf*. Cambridge University Press, October 2009. ISBN 978-0-511-60004-3.
- [108] M. Yousuff and N.W. Page. Die stress and internal friction during quasi-static and dynamic powder compaction. *Powder Technology*, 76(3):299–307, 1993. ISSN 0032-5910. doi: [https://doi.org/10.1016/S0032-5910\(05\)80011-7](https://doi.org/10.1016/S0032-5910(05)80011-7).

- [109] Charles E. Anderson. Compression testing and response of SiC-N ceramics: Intact, damaged and powder. In *Advances in Ceramic Armor: A Collection of Papers Presented at the 29th International Conference on Advanced Ceramics and Composites, Jan 23-28, 2005, Cocoa Beach, FL, Ceramic Engineering and Science Proceedings, Vol 26*, page 109. John Wiley & Sons, 2009.
- [110] Sia Nemat and Sai Sarva. Micro-mechanisms of compression failure. page 17, 2002.
- [111] James Lankford, W. W. Predebon, J. M. Staehler, G. Subhash, B. J. Pletka, and C. E. Anderson. The role of plasticity as a limiting factor in the compressive failure of high strength ceramics. *Mechanics of Materials*, 29(3):205–218, 1998.
- [112] R. W. Klopp and D. A. Shockey. The strength behavior of granulated silicon carbide at high strain rates and confining pressure. *Journal of Applied Physics*, 70(12):7318–7326, December 1991. ISSN 0021-8979, 1089-7550. doi: 10.1063/1.349750.
- [113] C. J. Shih, V. F. Nesterenko, and M. A. Meyers. High-strain-rate deformation and comminution of silicon carbide. *Journal of Applied Physics*, 83(9):4660–4671, May 1998. ISSN 0021-8979, 1089-7550. doi: 10.1063/1.367252.
- [114] C.J. Shih, M.A. Meyers, and V.F. Nesterenko. High-strain-rate deformation of granular silicon carbide. *Acta Materialia*, 46(11):4037–4065, July 1998. ISSN 13596454. doi: 10.1016/S1359-6454(98)00040-8.
- [115] Robert D Carneim and Gary L Messing. Response of granular powders to uniaxial loading and unloading. page 8, 2001.
- [116] V. F. Nesterenko, M. A. Meyers, and H. C. Chen. Shear localization in high-strain-rate deformation of granular alumina. *Acta materialia*, 44(5):2017–2026, 1996.
- [117] S A Dyachkov, A N Parshikov, and V V Zhakhovsky. SPH simulation of boron carbide under shock compression with different failure models. *Journal of Physics: Conference Series*, 815:012012, February 2017. ISSN 1742-6588, 1742-6596. doi: 10.1088/1742-6596/815/1/012012.
- [118] B.J. Briscoe and S.L. Rough. The effects of wall friction in powder compaction. *Colloids and Surfaces A: Physicochemical and Engineering Aspects*, 137(1-3):103–116, June 1998. ISSN 09277757. doi: 10.1016/S0927-7757(97)00210-0.

- [119] Robert A. Dimilia and James S. Reed. Stress Transmission During the Compaction of a Spray-Dried Alumina Powder in a Steel Die. *Journal of the American Ceramic Society*, 66(9):667–672, September 1983. ISSN 0002-7820, 1551-2916. doi: 10.1111/j.1151-2916.1983.tb10619.x.
- [120] Sidney Chocron, Charles E. Anderson, Kathryn A. Dannemann, Arthur E. Nicholls, and Nikki L. King. Intact and Predamaged Boron Carbide Strength under Moderate Confinement Pressures. *Journal of the American Ceramic Society*, 95(1): 350–357, January 2012. ISSN 00027820. doi: 10.1111/j.1551-2916.2011.04931.x.
- [121] S. Stupkiewicz, A. Piccolroaz, and D. Bigoni. Elastoplastic coupling to model cold ceramic powder compaction. *Journal of the European Ceramic Society*, 34(11): 2839–2848, September 2014. ISSN 09552219. doi: 10.1016/j.jeurceramsoc.2013.11.017.
- [122] D.R. Curran, L. Seaman, T. Cooper, and D.A. Shockey. Micromechanical model for comminution and granular flow of brittle material under high strain rate application to penetration of ceramic targets. *International Journal of Impact Engineering*, 13(1):53–83, January 1993. ISSN 0734743X. doi: 10.1016/0734-743X(93)90108-J.
- [123] Robert David Carneim. Characterization of Uniaxial Compaction in Spray Dried Ceramic Powders. page 124.
- [124] Itai Einav. Breakage mechanics—Part I: Theory. *Journal of the Mechanics and Physics of Solids*, 55(6):1274–1297, June 2007. ISSN 00225096. doi: 10.1016/j.jmps.2006.11.003.
- [125] Ali Daouadji, Pierre-Yves Hicher, and Aff Rahma. An elastoplastic model for granular materials taking into account grain breakage. *European Journal of Mechanics - A/Solids*, 20(1):113–137, January 2001. ISSN 09977538. doi: 10.1016/S0997-7538(00)01130-X.
- [126] Wei Hu, ZhenYu Yin, Christophe Dano, and Pierre-Yves Hicher. A constitutive model for granular materials considering grain breakage. *Science China Technological Sciences*, 54(8):2188–2196, August 2011. ISSN 1674-7321, 1862-281X. doi: 10.1007/s11431-011-4491-0.
- [127] R. Kumar, W. Ketterhagen, A. Sarkar, J. Curtis, and C. Wassgren. Breakage modeling of needle-shaped particles using the discrete element method. *Chemical*

- Engineering Science: X*, 3:100027, August 2019. ISSN 25901400. doi: 10.1016/j.cesx.2019.100027.
- [128] A. Tengattini, A. Das, and I. Einav. A constitutive modelling framework predicting critical state in sand undergoing crushing and dilation. *Géotechnique*, 66(9):695–710, September 2016. ISSN 0016-8505, 1751-7656. doi: 10.1680/jgeot.14.P.164.
- [129] Jürgen Almanstötter. A modified Drucker–Prager Cap model for finite element simulation of doped tungsten powder compaction. *International Journal of Refractory Metals and Hard Materials*, 50:290–297, May 2015. ISSN 02634368. doi: 10.1016/j.ijrmhm.2015.02.005.
- [130] N. H. Murray, N. K. Bourne, Z. Rosenberg, and J. E. Field. The spall strength of alumina ceramics. *Journal of Applied Physics*, 84(2):734–738, July 1998. ISSN 0021-8979, 1089-7550. doi: 10.1063/1.368130.
- [131] Timothy J Holmquist, Douglas W Templeton, and Krishan D Bishnoi. Constitutive modeling of aluminum nitride for large strain, high-strain rate, and high-pressure applications. *International Journal of Impact Engineering*, 25(3):211–231, March 2001. ISSN 0734743X. doi: 10.1016/S0734-743X(00)00046-4.
- [132] A. I. Lur’e and Alexander Belyaev. *Theory of Elasticity*. Foundations of Engineering Mechanics. Springer, Berlin ; New York, 2005. ISBN 978-3-540-24556-8.
- [133] Piaras Kelly. *Mechanics Lecture Notes: An introduction to Solid Mechanics*.
- [134] S. Shima and M. Oyane. Plasticity theory for porous metals. *International Journal of Mechanical Sciences*, 18(6):285–291, June 1976. ISSN 00207403. doi: 10.1016/0020-7403(76)90030-8.

Appendix A

Data Processing

A.1 MATLAB Code - Confined Uniaxial Compression of Granular Stainless Steel 316

```
clear all; close all
%% Input Sample Data
filename01 = 'SSType316_300um_May282018_01.dat'; %Import .dat file
%% Import Data
% Determine the number of headers to ignore
fid = fopen(filename01);
s=textscan(fid,'%s');
fclose(fid);
str=s{:};
idx = strfind(str, 'Data');
idx = find(not(cellfun('isempty', idx)));
headers = length(idx);
% Read the data, ignoring headers
fid = fopen(filename01);
% Getting rid of 5 lines before first row of data
data = textscan(fid,'%f%f%f%f%f', 'HeaderLines', 5);
force = data{:,1}; % [N]
displacement = data{:,2};% [mm]
time = data{:,3}; % [s]
friction = data{:,4}; % [V]
displacement_lvdt_V = data{:,5}; % [V]
```

```

epsilon_1 = data{:,6}; % [V]
% Getting rid of lines at the MTS time step print out
for i = 1:headers
    data = textscan(fid,'%f%f%f%f%f', 'HeaderLines', 3);
    force = [force; data{:,1}]; % [N]
    displacement = [displacement; data{:,2}]; % [mm]
    time = [time; data{:,3}]; % [s]
    friction = [friction; data{:,4}]; % [mV]
    displacement_lvdt_V = [displacement_lvdt_V; data{:,5}]; % [V]
    epsilon_1 = [epsilon_1; data{:,6}]; % [V]
end
%% Determine the start of the test
% Data only used when a negative force is obtained
for i = 1:length(time)
    if ((time(i) >=0))
        start = i;
        break
    end
end
%% Determine the end of the test
% The data is cut off when maximum desired load is reached
for j = 1:length(time)
    if (time(j) >=307.58398)
        finish = j;
        break
    end
end
%% Renaming the variables
force = force(start:finish);
displacement = displacement(start:finish) ;
time = time(start:finish);
friction = friction(start:finish);
displacement_lvdt_V = displacement_lvdt_V(start:finish);
epsilon_1 = epsilon_1(start:finish);
%% Calculations to determine relationships
% Initializing constants
SampleDiameter = 0.00635; % [m]
A_o = pi*((SampleDiameter/2).^2); % [m2]

```

```

E_c = 1.93e11; % [Pa]
nu_c = 0.25;
V = input('Volume of sample: ');
V_o = V./1e9; % [m3]
a = 0.00635/2; % [m]
b = 0.02223/2; % [m]
gain = 1000; % [unitless]
GF = 2.05; % [unitless]
Vex = 2 ; % [V]
hi = 0.0045; % [m]
m = input('What is the mass of the sample? '); % [Kg]
% Converting aux instruments
D_LVDT = (-1.5.*(displacement_lvdt_V))./1000; % [m]
D_LVDT=D_LVDT-D_LVDT(1,1); % Setting LVDT to zero
strain = ((epsilon_1)./(gain.*Vex.*GF)); % [strain]
LoadWasher = 459.655.*(friction) - 30.006;% [N]
% Calculating relationships
h = hi - abs(max(D_LVDT)); % [m]
rho_s = 8000 ; % [Kg/m3]
F_z = force - LoadWasher; % [N]
sigma_z = -F_z./A_o; % [Pa]
sigma_theta = strain.*((2.*a.^2.*(1-nu_c.^2))./(E_c.*(b.^2-a.^2))).^(-1); %
[Pa]
sigma_hyd = 1/3.*(sigma_z + 2.*sigma_theta); % [Pa]
sigma_hyd_MTS = 1/3.*(force./A_o + 2.*sigma_theta); % [Pa]
force_average = (force + LoadWasher)./2; % [Pa]
sigma_average = -(force_average)./A_o; % [Pa]
sigma_applied = -force./A_o; % [Pa]
sigma_applied = sigma_applied/1e6; % Converting to [MPa]
k_mean = sigma_theta./sigma_average; % Janssen constant using average stress
k = sigma_theta./sigma_z; % Janssen constant using stress
sigma_hyd = sigma_hyd/1e6; % Converting to MPa
delta_V = A_o.*(D_LVDT); % Change in volume
rho_lvdt = m./(V_o + delta_V); % Density [Kg/m-3]
phi = 1-(rho_lvdt./rho_s); % [%]
TR = LoadWasher./force; % Transmission ratio
Bulk = -sigma_hyd./(delta_V./V_o); % Secant bulk modulus
phi = 100.*phi; % Porosity in percent

```

```

sigma_z = sigma_z/1e6; % Converting to MPa
%% Discrepancy between using and not using the load washer; testing to see
    significance
diff = ( sigma_hyd_MTS-sigma_hyd)./sigma_hyd;
maximum = abs(max(diff));
%% Plot Porosity vs. Hydrostatic pressure
figure
plot(phi,sigma_hyd);
title('Porosity vs. janssen average','FontSize',16);
xlabel('Porosity, %','FontSize',16);
ylabel('Average Janssen, MPa','FontSize',16);
legend('Location','NorthEast');

```

A.2 MATLAB Code - Quasi-static Confined Uniaxial Compaction of Granular Al₂O₃ and B₄C

```

clear all; close all
%% Input Sample Data
filename01 = 'B4C_400_01.csv'; %Import data file
%% Import Data
% Determine the number of headers to ignore
data = csvread(filename01,3);
axial_top = data(:,1); % [kN]
axial_bottom = data(:,2);% [kN]
radial = data(:,3); % [kN]
displacement = data(:,4); % [mm]
axial_top = axial_top.*1000; %[N]
axial_bottom = axial_bottom.*1000;%[N]
radial = radial.*1000;%[N]
displacement = displacement./1000;%[m]
% Calculate the compliance of the equipment
compliance = (-0.00000001.*axial_top + 3E-8.*axial_top);
displacement = displacement-compliance;
displacement = displacement-displacement(1,1);
%% Calculations

```

```

% Initializing constants
SampleDiameter = 0.006;    % [m]
A_o = pi.*((SampleDiameter./2).^2);    % [m2]
radial_D = 0.003;    % [m]
A_radial = pi.*((radial_D./2).^2);    % [m2]
V = input('What is the initial volume: ');    % [mm3]
V_o = V./(1E9);    % Convert to [m3]
mass = input('What is the mass of the sample? ');    % [g]
m = mass/1000;    % [Convert to kg]

% Calculating relationships
rho_s = 2520;    % [Kg/m3]
    %B4C          2520
    %Alumina      3987
    %20-B4C-80-A1 3694
    %30-B4C-70-A1 3547
    %40-B4C-60-A1 3400
    %50-B4C-50-A1 3253
    %60-B4C-40-A1 3107
    %80-B4C-20-A1 2813

F_z = axial_top - axial_bottom;    % [N]
sigma_z = (1/(1E6)).*(F_z./A_o);    % [MPa]
sigma_top = (1/(1E6)).*(axial_top./A_o);    % [MPa]
sigma_bottom = (1/(1E6)).*(axial_bottom./A_o);    % [MPa]
sigma_theta = (1/(1E6)).*(radial./A_radial);    % [MPa]
sigma_hyd = 1/3.*(sigma_z + 2.*sigma_theta);    % [MPa]
sigma_dev = abs(sigma_z - sigma_theta);    % [MPa]
delta_V = A_o.*(displacement);    % Change in volume [m3]
rho = m./(V_o - delta_V);    % Density [kg/m-3]
phi = 1-(rho./rho_s);    % Pososity
phi = 100.*phi;    % Porosity [%]
D = rho./rho_s;    % Relative density
bulk = sigma_hyd./(delta_V./V_o);    % Secant bulk modulus
Z_z = (delta_V+V_o);    % Volume
TR = sigma_bottom./sigma_top;    % Transmission ratio
janssen = sigma_theta./sigma_z;    % Janssen constant

%% Incremental Bulk Modulus
dv = diff(delta_V);    % [m3]
dp = diff(sigma_hyd);    % [MPa]

```

```
bulk_in = V_o.*(dp./dv); % [MPa]
%% Hydrostatic Pressure vs Porosity comparison
figure
plot(D,sigma_hyd);
xlabel('Relative density');
ylabel('Hydro-static pressure MPa');
%% Dev vs Hyd
figure
plot(sigma_hyd,sigma_dev);
ylabel('Deviatoric MPa');
xlabel('Hydro-static MPa');
```

Appendix B

Uncertainty - Propagation of Error

In order to account for uncertainty in the measurements obtained from the experiments, error propagation analysis was conducted, investigating the systematic error. The theory of deriving the equations has been extensively studied in the past and will only be summarized here for completeness. Refer to [90] for full derivation.

Five general rules were followed when calculating the error propagation. To better explain, suppose you measure some quantities x, y, z, \dots with the uncertainties $\delta x, \delta y, \delta z, \dots$. You use these measured quantities to calculate the dependant variable f which is composed of x, y, z, \dots . The uncertainties in each measured variable propagate and the listed rules are followed. Note that we assume the measured quantities have errors that are random and uncorrelated.

1. Addition and Subtraction: Suppose that if

$$f = x + y - z$$

then the error will be

$$\delta f = \sqrt{(\delta x)^2 + (\delta y)^2 + (\delta z)^2}$$

2. Multiplication and division: Suppose that if

$$f = \frac{xy}{z}$$

then the error will be

$$\frac{\delta f}{|f|} = \sqrt{\left(\frac{\delta x}{x}\right)^2 + \left(\frac{\delta y}{y}\right)^2 + \left(\frac{\delta z}{z}\right)^2}$$

3. Multiplying a measured quantity with a constant C : If the function

$$f = Cx$$

then the propagation of uncertainty will be

$$\delta f = |C|\delta x$$

4. The uncertainty in the power rule where n is an exact number such that

$$f = x^n$$

then the propagation of uncertainty will be

$$\frac{\delta f}{|f|} = |n|\frac{\delta x}{|x|}$$

5. The general formula for propagating the uncertainty in any function: Suppose that if

$$f = f(x, y, \dots)$$

then the uncertainty is

$$\delta f = \sqrt{\left(\frac{\partial f}{\partial x}\delta x\right)^2 + \left(\frac{\partial f}{\partial y}\delta y\right)^2 \dots}$$

A sample calculation for completeness has been provided. Referring to (3.4):

$$\Delta V = A_o\delta$$

where A_o was calculated using:

$$A_o = \frac{\pi}{4}(d)^2$$

so we begin by calculating the uncertainty in A_o where d is the diameter measured with a digital caliper with a resolution of 0.02 mm:

$$\begin{aligned}\delta A_o &= \sqrt{\frac{\pi}{4} \left(\frac{\partial A_o}{\partial d} \right)^2} \\ &= \sqrt{\frac{\pi}{4} (2d(0.02))^2} \\ &= \sqrt{\frac{\pi}{4} (12(0.02))^2} \\ &= 0.213 \text{ mm}\end{aligned}$$

To put this value into relative terms, we divide by the nominal value $A_o = 28.3\text{mm}$, and the relative systematic uncertainty is 0.01 %.

Appendix C

SEM Images of Tested Materials

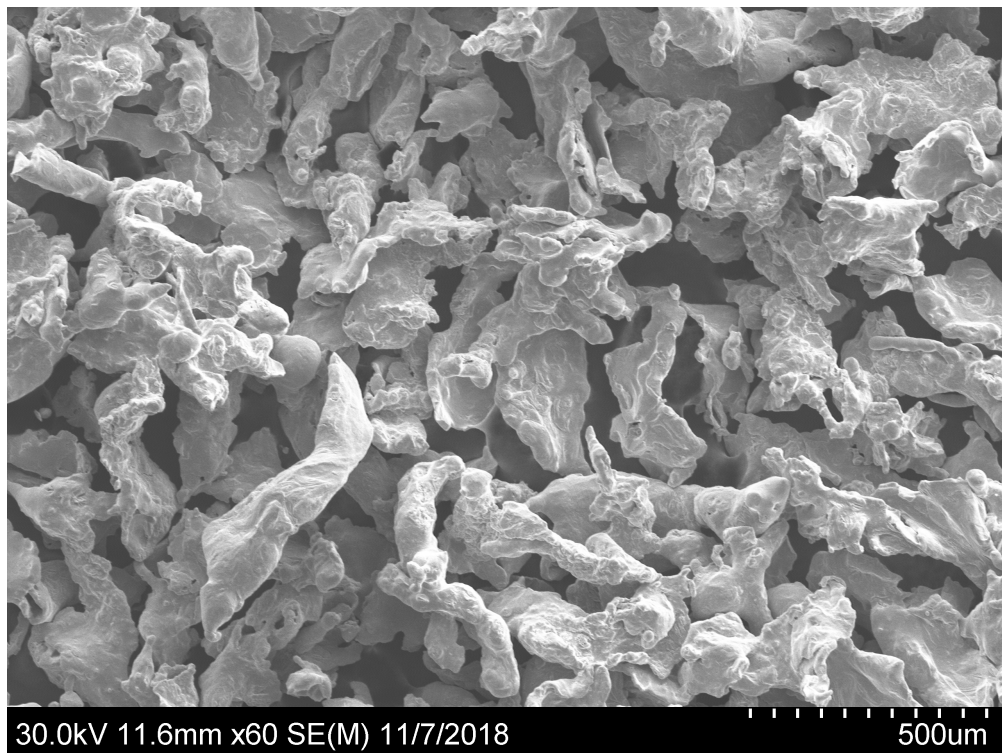


FIGURE C.1: SEM image of stainless steel 316 powder with an average particle size of $127 \pm 34 \mu\text{m}$ before the quasi-static compaction.

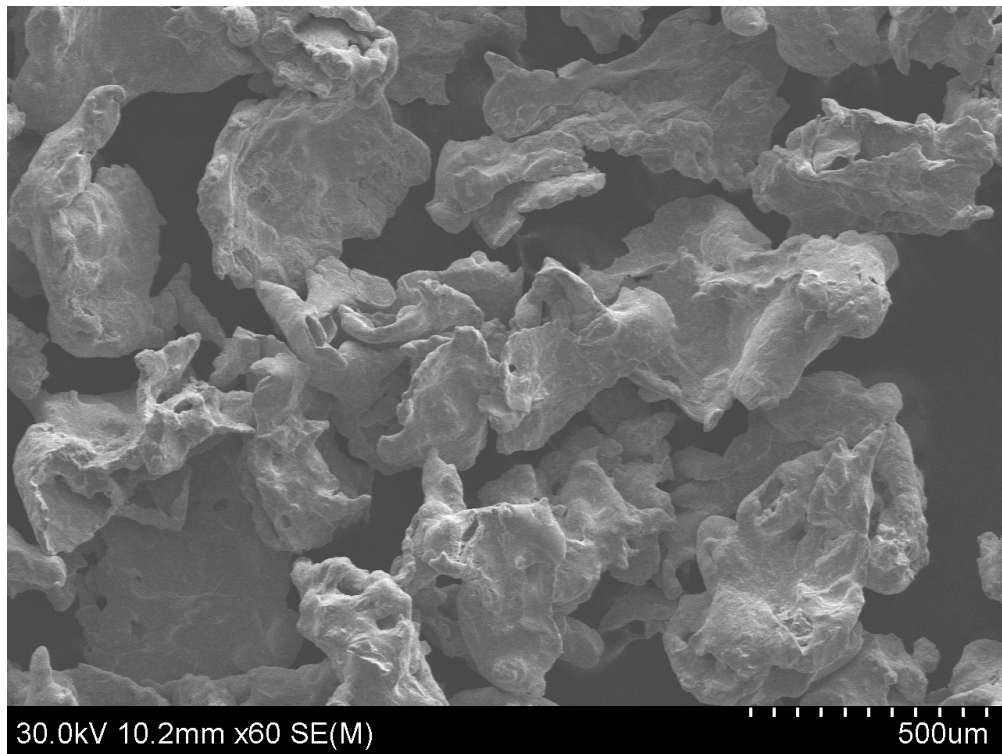


FIGURE C.2: SEM image of stainless steel 316 powder with an average particle size of $487 \pm 98 \mu\text{m}$ before the quasi-static compaction.

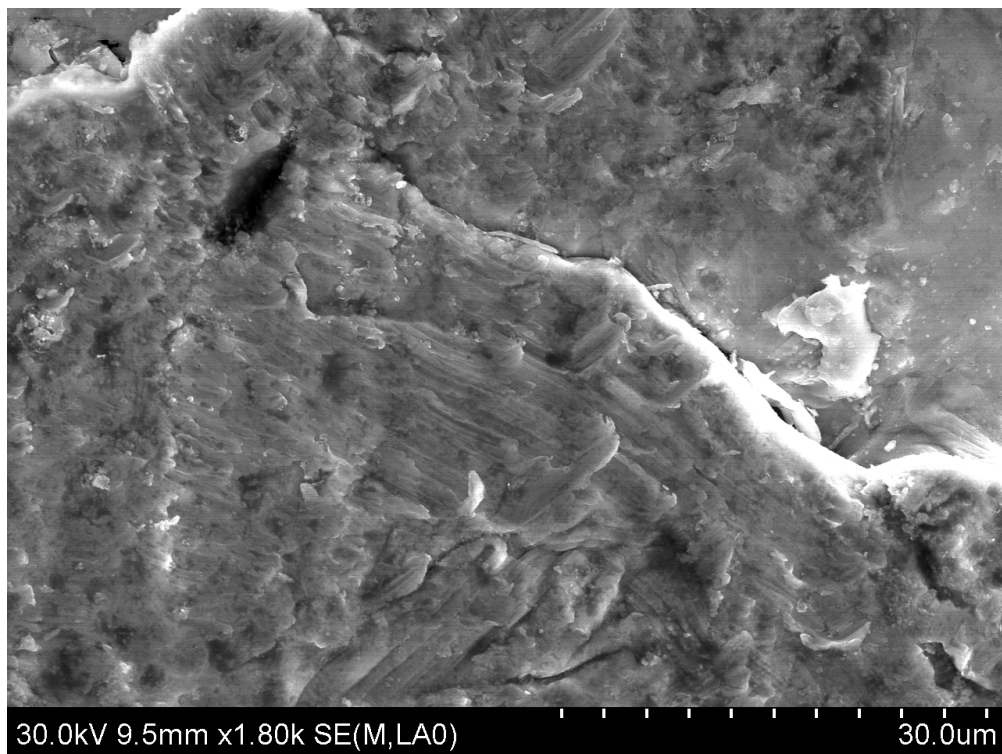


FIGURE C.3: SEM image of the stainless steel 316 powder at an average particle size of $127 \pm 34 \mu\text{m}$ post compaction.

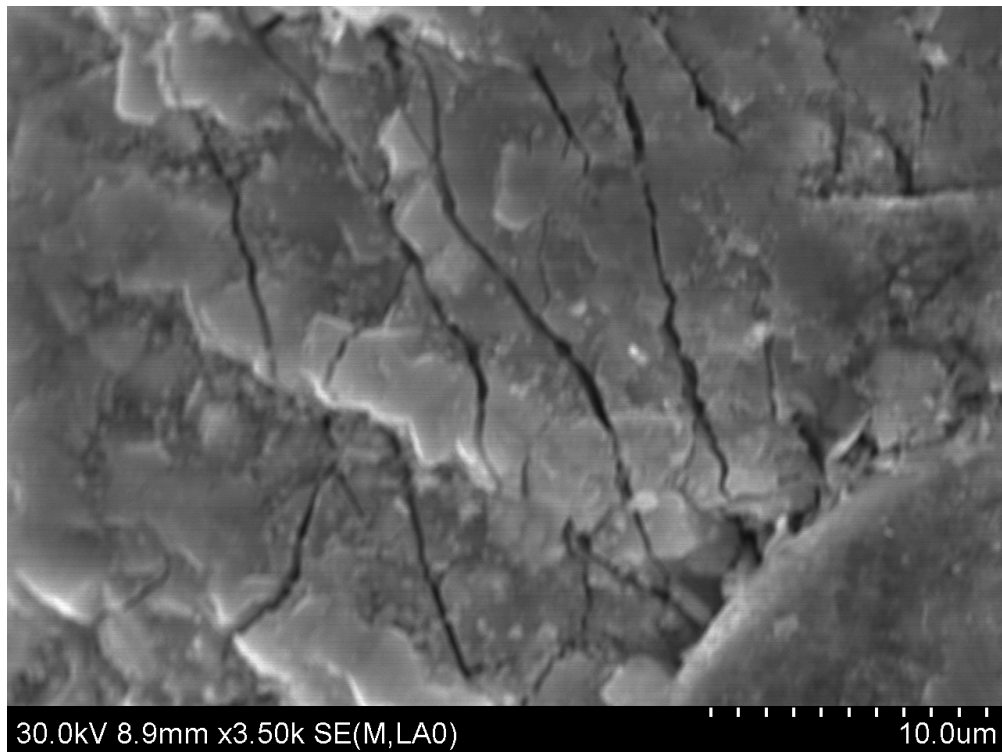


FIGURE C.4: SEM image of the stainless steel 316 powder at an average particle size of $487 \pm 98 \mu\text{m}$ post compaction.

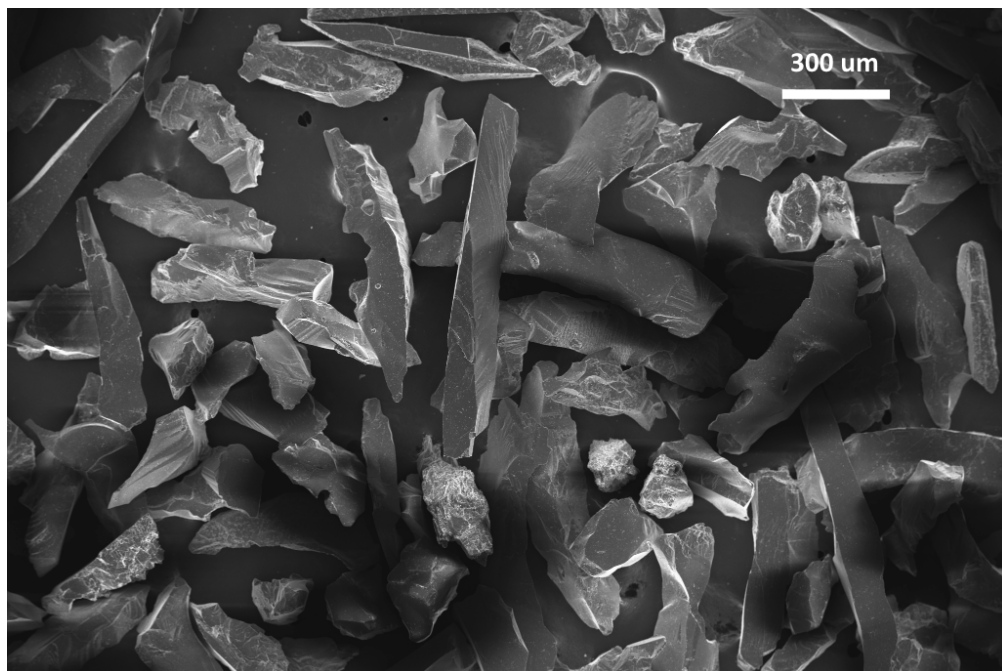


FIGURE C.5: SEM images were taken of the Al_2O_3 powder to observe powder morphology before experiments and failure features post-experiment. The following depicts the Al_2O_3 with an average particle size $170 \pm 63 \mu\text{m}$ before compression.

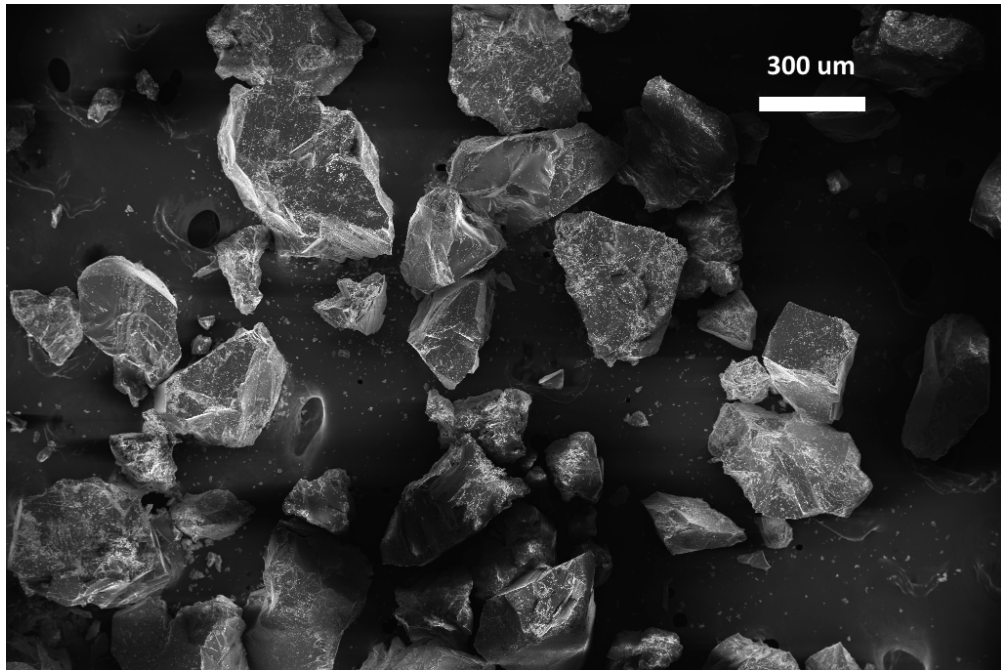


FIGURE C.6: The following is an SEM image of Al₂O₃ powder with an average particle size $170 \pm 63 \mu\text{m}$ after compression.

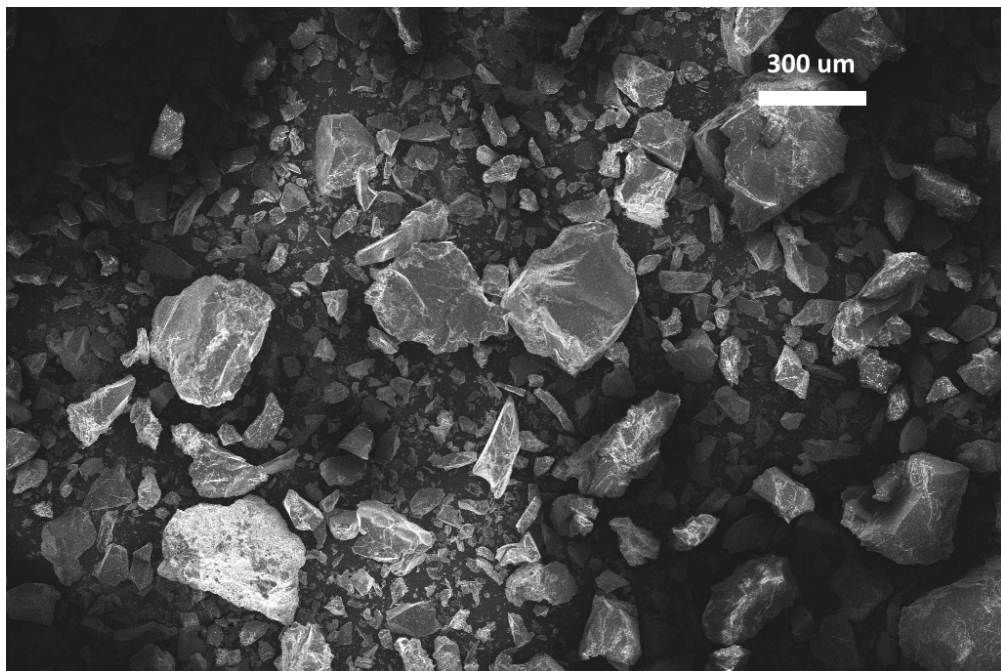


FIGURE C.7: SEM image of the large Al₂O₃ powder with an average particle size of $450 \pm 83 \mu\text{m}$ after the experiment showing the resulting material size and shapes.

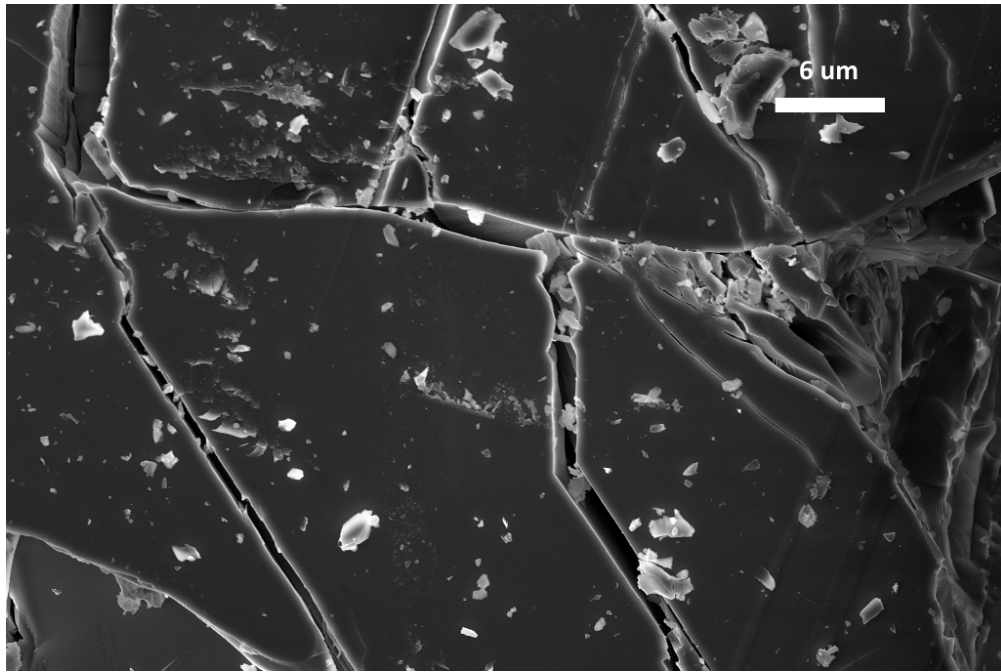


FIGURE C.8: SEM images were taken of the Al₂O₃ powder to observe powder morphology before experiments and failure features post-experiment. The following is Al₂O₃ powder with an average particle size of $450 \pm 83 \mu\text{m}$.

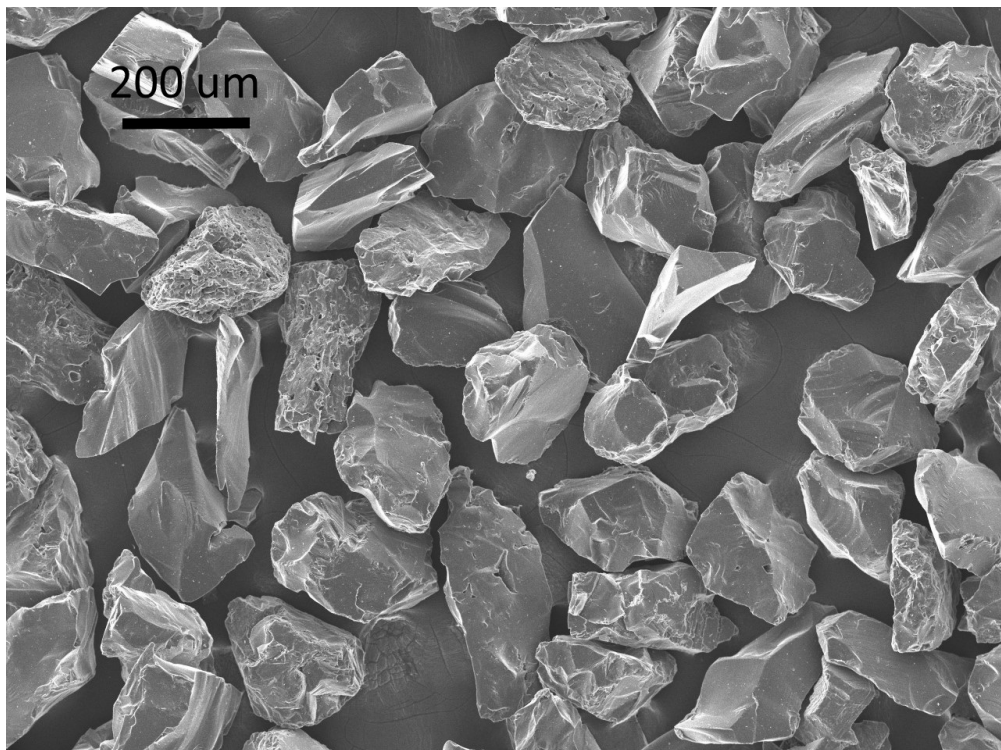


FIGURE C.9: SEM images of B₄C were taken to observe the small and large particles, focusing on powder morphology before and after experiment. The figure depicts $170 \pm 40 \mu\text{m}$ B₄C powder before compression.

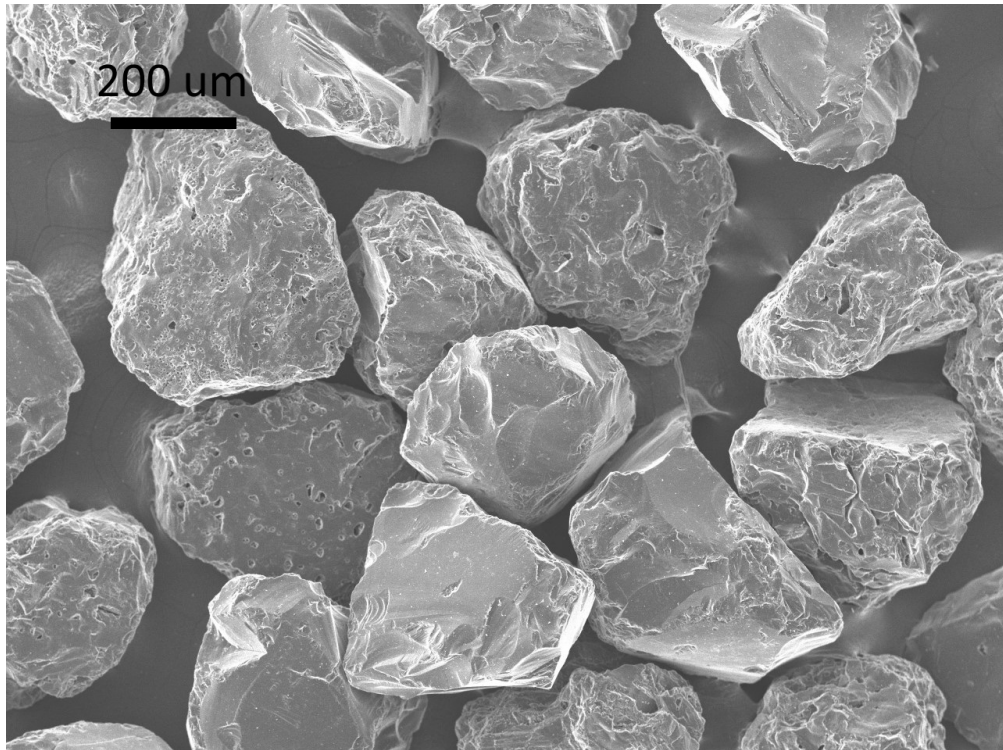


FIGURE C.10: The figure depicts B₄C powder with an average particle size of 320 ± 59 μm showing the overall geometry before compression.

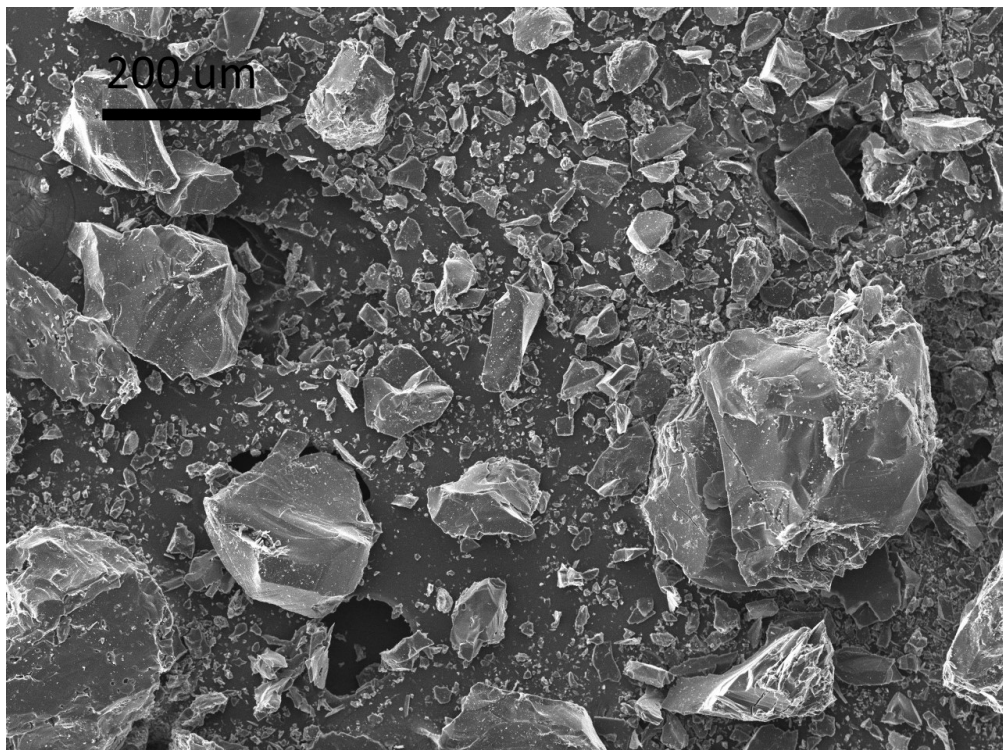


FIGURE C.11: The figure depicts the postmortem B₄C powder with an average particle size of 320 ± 59 μm visualizing the overall fragment distribution.

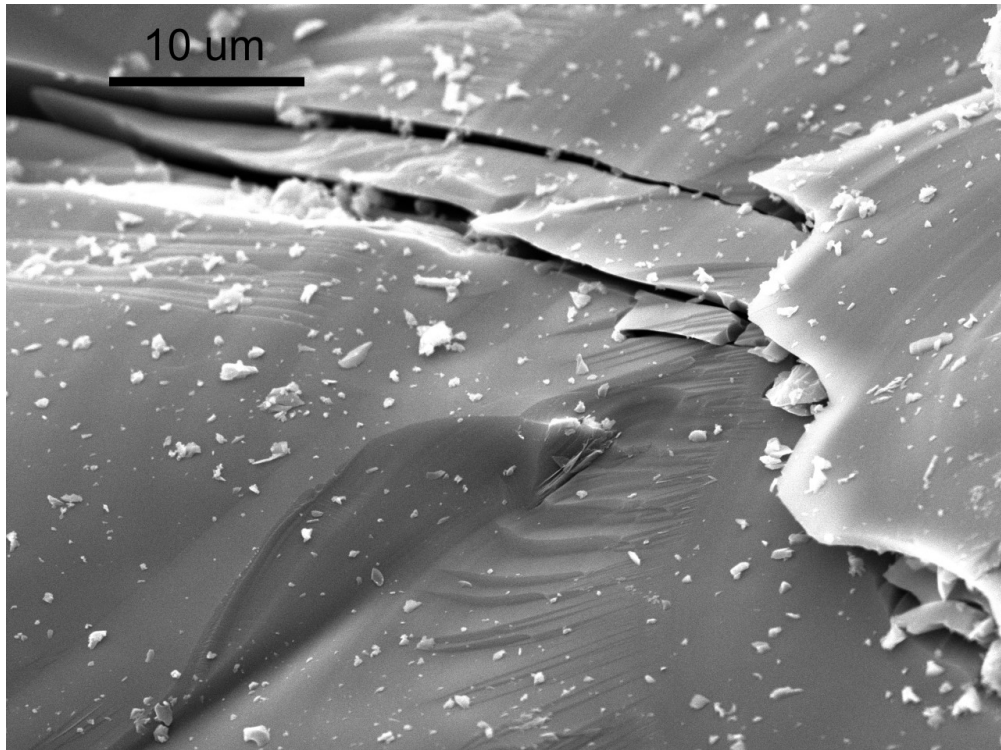


FIGURE C.12: The following figure depicts the surface features post experiment of B₄C powder with an average particle size $320 \pm 59 \mu\text{m}$.

Appendix D

Hooke's Law ^a

D.1 Generalized Hooke's Law

Hooke's law describes that the stress experienced by an object by an external force, is proportional to the gradient of deformation occurring in the material. In Cartesian coordinates, we can write the generalized Hooke's law:

$$\sigma_{ij} = C_{ijkl}\varepsilon_{kl} \quad \text{where } i,j,k,l = 1,2,3 \quad (\text{D.1})$$

where σ_{ij} is the second order stress tensor and ε_{kl} is the second order strain tensor. These equations assume that stress is a linear function of strain and we refer to them as constitutive equations. These equations are applicable to materials experiencing small deformations when subjected to external forces. The 81 independent constants described by C_{ijkl} the stiffness tensor, are the elastic stiffness of the material. Due to the symmetry of σ_{ij} and ε_{ij} , the stiffness tensor must satisfy these relations:

$$C_{ijkl} = C_{jikl} = C_{ijlk} = C_{jilk}$$

which allows us to simplify the stiffness tensor to 36 independent constants.

^aThe following derivations were taken from [132].

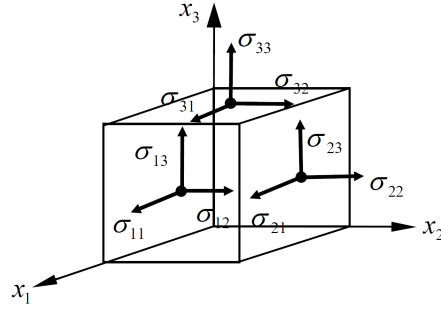


FIGURE D.1: Stress components defined with respect to the Cartesian coordinate system [133].

Using the coordinate system outline in Figure D.1, we define a new set of variables to make the equations easier to analyze:

$$\begin{bmatrix} \sigma_1 & \sigma_4 & \sigma_5 \\ \sigma_4 & \sigma_2 & \sigma_6 \\ \sigma_5 & \sigma_6 & \sigma_3 \end{bmatrix} = \begin{bmatrix} \sigma_{11} & \sigma_{12} & \sigma_{13} \\ \sigma_{21} & \sigma_{22} & \sigma_{23} \\ \sigma_{31} & \sigma_{32} & \sigma_{33} \end{bmatrix}$$

The generalized equations for Hooke's law can be represented as:

$$\sigma_i = C_{ij}\varepsilon_j \quad (\text{D.2})$$

Note that the same relation can be expressed in terms of strain, using the elastic compliance tensor, S_{ij} . These constants satisfy the relation:

$$S_{mi}C_{ij} = \delta_{mj} \quad \text{where } i, m, j = 1, \dots, 6$$

and

$$\sigma_{ij} = \begin{cases} \sigma_i, & i=j=1,2,3 \\ \sigma_{1+i+j}, & i \neq j, \text{ and } i = 1, \text{ or } 2 \end{cases}$$

Further these relations show that C_{ij} is related to C_{pqrs} by the relation

$$\begin{aligned}
C_{m1} &= C_{ij11} & C_{m4} &= 2C_{ij12} \\
C_{m2} &= C_{ij22} & C_{m5} &= 2C_{ij13} \\
C_{m3} &= C_{ij33} & C_{m6} &= 2C_{ij23}
\end{aligned}$$

where

$$m = \begin{cases} i, & \text{when } i = j = 1, 2, \text{ or } 3 \\ 1 + i + j, & \text{when } i \neq j \text{ and } i = 1 \text{ or } 2 \end{cases}$$

The above equations can be verified by expanding (D.1) and (D.2) and comparing like terms.

The generalized form of Hooke's law can now be expanded where all 36 independent constants can be seen:

$$\begin{bmatrix} \sigma_1 \\ \sigma_2 \\ \sigma_3 \\ \sigma_4 \\ \sigma_5 \\ \sigma_6 \end{bmatrix} = \begin{bmatrix} C_{11} & C_{12} & C_{13} & C_{14} & C_{15} & C_{16} \\ C_{21} & C_{22} & C_{23} & C_{24} & C_{25} & C_{26} \\ C_{31} & C_{32} & C_{33} & C_{34} & C_{35} & C_{36} \\ C_{41} & C_{42} & C_{43} & C_{44} & C_{45} & C_{46} \\ C_{51} & C_{52} & C_{53} & C_{54} & C_{55} & C_{56} \\ C_{61} & C_{62} & C_{63} & C_{64} & C_{65} & C_{66} \end{bmatrix} \begin{bmatrix} \varepsilon_1 \\ \varepsilon_2 \\ \varepsilon_3 \\ \varepsilon_4 \\ \varepsilon_5 \\ \varepsilon_6 \end{bmatrix} \quad (\text{D.3})$$

D.2 Material Symmetries

For an isotropic material, it is assumed that the elasticity is the same in all directions. This allows one to simplify (D.3) to the following relation:

$$\begin{bmatrix} \sigma_1 \\ \sigma_2 \\ \sigma_3 \\ \sigma_4 \\ \sigma_5 \\ \sigma_6 \end{bmatrix} = \begin{bmatrix} C_{11} & C_{12} & C_{13} & 0 & 0 & 0 \\ C_{21} & C_{22} & C_{23} & 0 & 0 & 0 \\ C_{31} & C_{32} & C_{33} & 0 & 0 & 0 \\ 0 & 0 & 0 & C_{44} & 0 & 0 \\ 0 & 0 & 0 & 0 & C_{55} & 0 \\ 0 & 0 & 0 & 0 & 0 & C_{66} \end{bmatrix} \begin{bmatrix} \varepsilon_1 \\ \varepsilon_2 \\ \varepsilon_3 \\ \varepsilon_4 \\ \varepsilon_5 \\ \varepsilon_6 \end{bmatrix} \quad (\text{D.4})$$

With the reduced matrix, we define the quantities and note that for isotropic materials these constants are not independent. Finally we can write out for Hooke's law in three dimensional space where E is the Young's modulus of elasticity and ν is the Poisson's ratio.

$$\begin{Bmatrix} \sigma_{11} \\ \sigma_{22} \\ \sigma_{33} \\ \sigma_{23} \\ \sigma_{13} \\ \sigma_{12} \end{Bmatrix} = \frac{E}{(1+\nu)(1-2\nu)} \begin{bmatrix} (1-\nu) & \nu & \nu & 0 & 0 & 0 \\ & (1-\nu) & \nu & 0 & 0 & 0 \\ & & (1-\nu) & 0 & 0 & 0 \\ & & & \frac{(1-2\nu)}{2} & 0 & 0 \\ & & & & \frac{(1-2\nu)}{2} & 0 \\ \text{sym} & & & & & \frac{(1-2\nu)}{2} \end{bmatrix} \begin{Bmatrix} \varepsilon_{11} \\ \varepsilon_{22} \\ \varepsilon_{33} \\ 2\varepsilon_{23} \\ 2\varepsilon_{13} \\ 2\varepsilon_{12} \end{Bmatrix}$$

For simplicity in notation, the above matrix can be written out for isotropic plain stress, where the matrix parameters have been outlined above. The constitutive equations are:

$$\begin{aligned}\sigma_{11} &= \frac{E}{(1+\nu)(1-2\nu)} [(1-\nu)\varepsilon_{11} + \nu(\varepsilon_{22} + \varepsilon_{33})] \\ \sigma_{22} &= \frac{E}{(1+\nu)(1-2\nu)} [(1-\nu)\varepsilon_{22} + \nu(\varepsilon_{33} + \varepsilon_{11})] \\ \sigma_{33} &= \frac{E}{(1+\nu)(1-2\nu)} [(1-\nu)\varepsilon_{33} + \nu(\varepsilon_{22} + \varepsilon_{11})] \\ \sigma_{12} = \sigma_{21} &= \frac{E}{1+\nu}\varepsilon_{12} \\ \sigma_{13} = \sigma_{31} &= \frac{E}{1+\nu}\varepsilon_{13} \\ \sigma_{23} = \sigma_{32} &= \frac{E}{1+\nu}\varepsilon_{23}\end{aligned}$$

D.3 Cylindrical Coordinates

The same theory and material symmetry can be applied using the cylindrical coordinate system as it was outlined above. Refer to Figure D.2 for visualization of the principle directions.

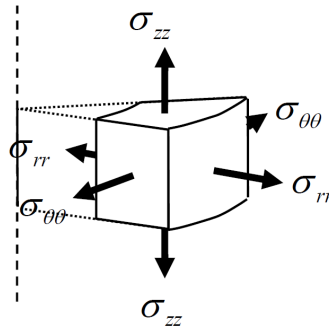


FIGURE D.2: Stress components with respect to the cylindrical coordinates [133].

Due to the cylindrical shape, the stress components are independent of the angular coordinate θ and so the derivatives with respect to θ are equal to zero. The result of the constitutive equations for the stress tensor in cylindrical coordinates can be written as:

$$\begin{Bmatrix} \sigma_r \\ \sigma_z \\ \sigma_\theta \\ \tau_{r\theta} \\ \tau_{rz} \\ \tau_{\theta z} \end{Bmatrix} = \frac{E}{(1+\nu)(1-2\nu)} \begin{bmatrix} (1-\nu) & \nu & \nu & 0 & 0 & 0 \\ & (1-\nu) & \nu & 0 & 0 & 0 \\ & & (1-\nu) & 0 & 0 & 0 \\ & & & \frac{(1-2\nu)}{2} & 0 & 0 \\ & & & & 0 & 0 \\ & & & & & 0 \end{bmatrix} \begin{Bmatrix} \varepsilon_r \\ \varepsilon_z \\ \varepsilon_\theta \\ \gamma_{r\theta} \\ \gamma_{rz} \\ \gamma_{\theta z} \end{Bmatrix}$$

where E is the Young's modulus of elasticity and ν is the Poisson's ratio of the material. For an isotropic material, the plane stress can be expressed with the following constitutive equations:

$$\begin{aligned} \sigma_r &= \frac{E(1-\nu)}{(1+\nu)(1-2\nu)} [(1-\nu)\varepsilon_r + \nu\varepsilon_\theta] & \tau_{r\theta} &= \frac{E}{1+\nu} \varepsilon_{r\theta} = 2G\varepsilon_{r\theta} = G\gamma_{r\theta} \\ \sigma_\theta &= \frac{E(1-\nu)}{(1+\nu)(1-2\nu)} [(1-\nu)\varepsilon_\theta + \nu\varepsilon_r] & \tau_{rz} &= \tau_{\theta z} = 0 \\ \sigma_z &= \frac{E\nu}{(1+\nu)(1-2\nu)} [\varepsilon_r + \varepsilon_\theta] \end{aligned}$$

Appendix E

Supplementary Material

E.1 Curve fitting

Process simulations using finite element modelling is useful when controlling the density distribution of a desired part. For this to be done, numerical models are created which are further composed of constitutive equations. Using these relationships, various empirical yield functions are developed to resemble the densification of the material under certain loading conditions. The benefit of simulating multi-level confined compaction of granular ceramics and metals allows for not having to repeat multiple triaxial compression tests.

To understand the confined compression behaviour of the materials tested, a curve fitting function based on the elasto-plastic deformation of granular media is used. This relationship is further used in developing a cap model that predicts the densification of metal and ceramic powders. This function was generated based on the work by Shima and Oyane [134] and more recent work by Lee and Kim [70]. The curve fitting function form is as follows:

$$f(x) = Ae^{Bx} (1 - x)^C \tag{E.1}$$

where A , B , and C are function constants. From the results obtained during the compression experiments, (E.1) was fitted through the crush curve data points and magnitudes of the function constants were recorded. The target was focused on the advanced ceramic powders, as the hydro-static response was unique with respect to particle size through

out the loading range in comparison to the stainless steel 316. After the expression in (E.1) was fitted through the data A , B , and C was recorded and plotted against average particle size.

Observing the results from the Al_2O_3 powder, distinct trends can be seen in Figure E.1.

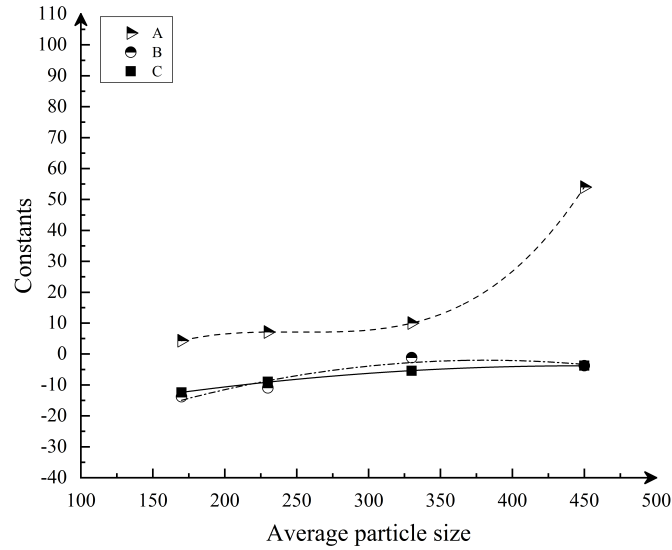


FIGURE E.1: For the Al_2O_3 powder, trends can be observed when plotting the constants (A, B, C) as a function of average particle size for (E.1). Polynomial fitting functions were used for the purpose to explicitly show the overall trends of each constant.

The most volatile parameter is A where it exponentially increases as the average particle size approaches $450\ \mu\text{m}$. The other two parameters B and C , approach an increasing plateau as the particle size increases towards $400\ \mu\text{m}$.

The same approach was applied to the B_4C powder and the trends are depicted in Figure E.2.

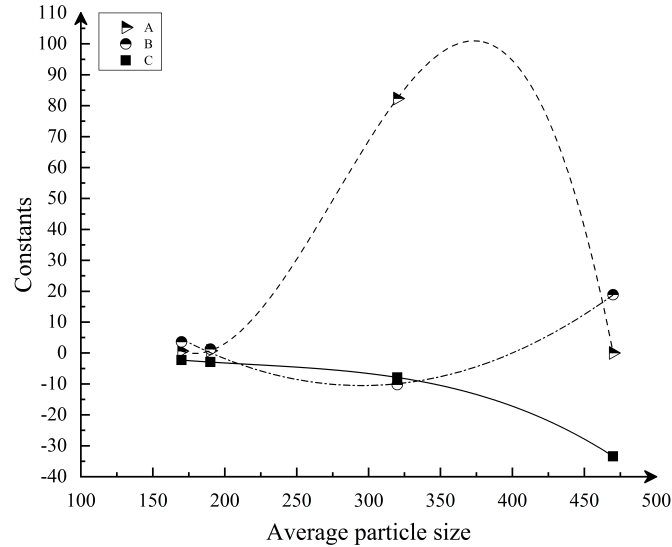


FIGURE E.2: The function constants (A, B, C) for granular B_4C were plotted against increasing particle size. Polynomial fitting functions of order two and three were used for the purpose of depicting overall trends of each constant.

Referring to constant A , the trend observed increases as particle size increase to $390 \mu\text{m}$ where an inflection point exists and the trend begins to decrease as particle size increases. A similar threshold exists when observing constants B and C . As the particle size increases towards $350 \mu\text{m}$, constant B increases with increasing particle size and constant C decreases with increasing particle size.

The behaviour of both ceramics is very complex and difficult to understand. This numerical work can be supplementary in creating failure cap models to incorporate the densification behaviour when predicting material failure. Additional research must be done on empirical modelling of granular advanced ceramics to better understand the observed trends illustrated in Figure E.1 and Figure E.2.

E.2 Particle distribution data

The distribution of the ceramics particles before and after compaction was analyzed and plotted. The empirical cumulative distribution function (ecdf) was plotted against particle size to observe any changes or trends. Illustrated in Figure E.3 the ecdf was plotted against particle size for granular alumina and in Figure E.4 is the ecdf plotted against average particle size for granular boron carbide.

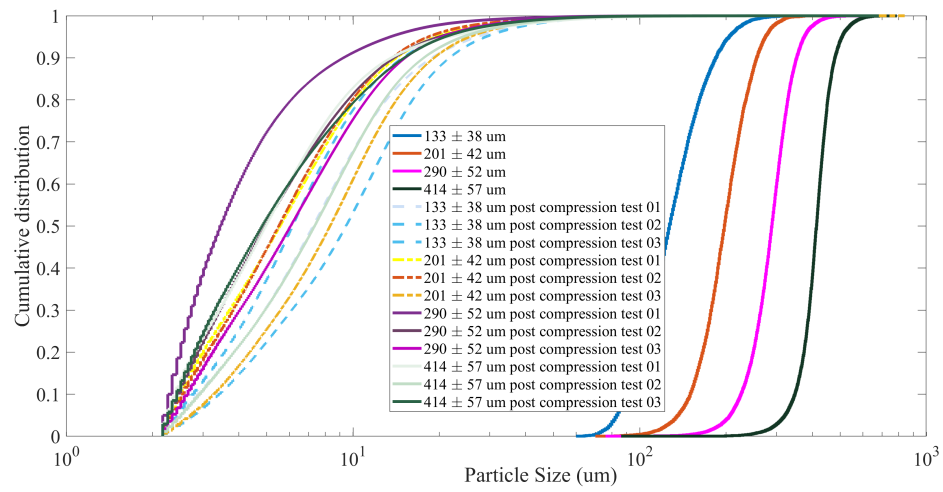


FIGURE E.3: The empirical cumulative distribution function is plotted against average particle size before and after compaction for granular alumina.

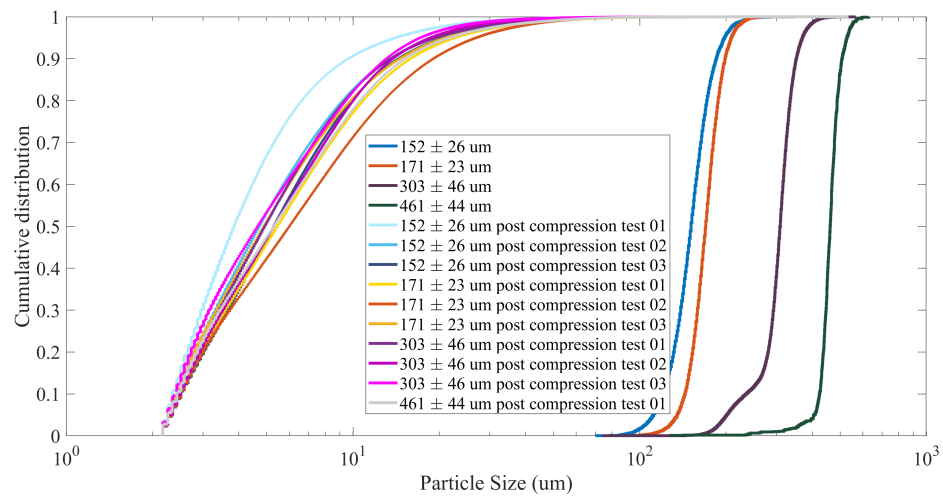


FIGURE E.4: The empirical cumulative distribution function is plotted against average particle size before and after compaction for granular boron carbide.

Appendix F

Curriculum Vitae



Education

2017 - 2019: Masters of Science in Mechanical Engineering | University of Alberta

Thesis topic: mechanics of material in advanced granular ceramics; failure prediction in blast mitigation.

Thesis title: "Confined Uniaxial Compaction Observing Triaxial Response of Granular Media under Quasi-static Loading Conditions"

2014 - 2017: Bachelor in Mechanical Engineering | University of Alberta

Enrolled in traditional program.

2013 - 2014: Bachelor of Science in Engineering Transfer | Macewan University

Enrolled in transfer program.

Academic Experience

2017 - Present: Graduate Student Researcher | *University of Alberta, Edmonton*

Bridging the work between academia and industry, specifically working with U. S. Army Research Laboratory, Defence Research and Development Canada, and Grey Ghost Gear

Canada in investigating the failure of advanced ceramics.

Summarized tasks as a researcher:

- Leading material related experiments being heavily involved in the following steps: outlining the problem at hand in order to create a solution, designing a feasible solution to successfully execute the experiments, interpreting the results to justify the observed trends, and clearly communicating the information to the scientific community.
- Designing and fabricated a experimental apparatus to test for triaxial compaction of granular materials. This included generating and reviewing technical drawings, managing formal documents (funding requests, work contracts, technical design reports, purchase orders, and progress presentations.)
- Based on the outlined work, currently there are two academic papers submitted for publication on the failure effects of granular stainless steel, alumina, and boron carbide under quasi-static triaxial compression loading conditions:

I First publication: P. Nicewicz, T. Sano, J.D. Hogan, "Confined Uniaxial Compression of Granular Stainless Steel 316". Powder Technology. *Accepted*. Manuscript number: POWTEC-D-18-03323R1. Article reference: PTEC14359.

II Second publication: P. Nicewicz, P. Peciar, O. Macho, T. Sano, J.D. Hogan. "Quasi-static Confined Uniaxial Compaction of Granular Alumina and Boron Carbide Observing the Particle Size Effects". Journal of the American Ceramic Society. *Under review*. Manuscript number: JACERS-44392.

III Conference Poster: B. M. L. Koch, P. Nicewicz, C. Lo, J. D. Hogan. *Collaborators*: P. Janotti, T. Sano, B. E. Schuster, T. Walter. "Failure of Advanced Ceramics: From Intact Materials to Granular Powders". MACH 2018. *Accepted*.

As an academic, the responsibilities were focused on course material and undergraduate students.

Summarized tasks as a Teaching Assistant:

- Understanding and developing the course content for *MecE 360: Mechanical Design II*. The goal was to incorporate a direct experience for the students where they

use various manufacturing techniques such as 3D printing, when designing in the course.

- Assisting undergraduate students in clarifying course material to help them in learning and motivating their creative direction.

May - Sep 2018: Process Engineer Intern | *Slovak University of Technology, Bratislava*

- Working in between academia and industry in solving problems with processing granular material. The major focus was optimizing the fertilizer manufacturing operation. The following tasks were completed: granular milling and dry granulation, particle characterization using microscopes and software, and summary report writing was generated for the client.
- Additional work for academic purposed included analyzing and testing various granular samples at different stages of manufacturing, investigating the mechanical properties of the material. Other tasks such as particle characterization of various granular media (pharmaceuticals, potash) were completed, using state of the art imaging microscopes and software.

Languages

- English: Native proficiency at reading, writing, and speaking.
- Polish: Exceptional at reading, writing, and speaking.

Computer skills

Design: SolidWorks, Catia

Administration: Microsoft Office, L^AT_EX, Adobe Acrobat

Computation: MATLAB, MathCad

Interests

- i **Mechanics** - Rebuilt a four cylinder engine, replacing all the engine internals to handle high power output.
- ii **Skiing** - Skied at various resorts in western Canada and United States.
- iii **Dance** - Member of Board of Directors for Lowicz Polish Folklore Ensemble; currently operating the administration of the organization.
- iv **CAD Design** - Continuously growing portfolio with personal projects, available upon request.